

THESIS

SPATIAL FREQUENCY MODULATED SINGLE DETECTOR IMAGING

Submitted by

Gregory L. Futia

Department of Electrical and Computer Engineering

In partial fulfillment of the requirements

For the Degree of Master of Science

Colorado State University

Fort Collins, Colorado

Spring 2011

Master's Committee:

Advisor: Randy Bartels

Ali Pezeshki

David Krueger

Peter Young

Copyright by Gregory L. Futia 2011

All Rights Reserved

ABSTRACT
SPATIAL FREQUENCY MODULATED SINGLE DETECTOR IMAGING

This thesis presents images of absorbing and fluorescent objects captured by modulating a time varying spatial frequency to an illumination beam. The modulator produces a field intensity with a linear increase in temporal modulation frequency across its spatial extent. The linear temporal modulation is preserved after square law integration over the area of the detector and present in its electronic signal. Recording the temporal signal out of the detector with analog to digital converter and then Fourier transforming recovers the profile of the spatial field intensity distribution on the detector. This imaging modality offers the possibility of relatively simple and high speed imaging of objects with an single element detector. The modulator can be produced at low cost by printing a mask onto a clear CD-ROM substrate. The theory developed explains how the parameters of the modulator and optical system relate to the resolution and number of points in the electrical image. Numerical simulations are used to explore the optical limits of the electrical image in the presence of optical aberrations. Experimental results verify theoretical relations and images are captured of a Air Force test pattern and prepared fluorescent patterns.

TABLE OF CONTENTS

ABSTRACT OF THESIS	ii
ACKNOWLEDGEMENTS	v
I INTRODUCTION	1
1.1 Contributions	5
II THEORY OF SPIFI	6
2.1 The Modulated Field at the Detector	6
2.1.1 SPIFI modulated illumination	6
2.1.2 Field Modulated SPIFI	8
2.1.3 SPIFI Pumped Fluorescence	9
2.2 SPIFI Derivation Using Parseval's Theorem	10
2.3 Effect of optical diffraction on the SPIFI image	11
2.3.1 Optical diffraction in coherent SPIFI modulated illumination	11
2.3.2 Optical diffraction for incoherent field modulated SPIFI	14
2.4 Resolution and Number of Points	15
2.5 Dynamic Range	16
2.5.1 Dynamic Range of Analog to Digital Converter	17
2.6 Symmetrical vs. Asymmetrical Modulation	18
2.7 Analysis of the time window	20
III THE DISC MODULATOR	22
3.1 Number of Points and Resolution	23
3.2 Wobble	24
3.3 Wobble Correction	25
IV EXPERIMENTAL	29
4.1 Wobble Correction	31
4.2 Fluorescent Imaging	35
V CONCLUSION	37
5.1 Future work	38
5.1.1 Improvements to the disk modulator	38
5.1.2 Removal of aberrations from the optical system	39
5.1.3 More efficient use of time-bandwidth product detector bandwidth & 2D	39
5.1.4 Additional Modulation Methods	40

5.1.5	SPIFI onto a 1D array	40
APPENDIX A — ADDITIONAL MATHEMATICAL DERIVATIONS AND CALCULATIONS		42
A.1	Direct transform frequency domain distribution	42
A.2	Map from space to frequency with magnifications between planes	43
A.2.1	Number of Points	45
A.3	Parameters for Disc Modulator	45
APPENDIX B — GENERAL OPTICAL CONSIDERATIONS		47
B.1	Spatial Frequency, NA, and Abbe Resolution	49
B.2	Conjugate Plane Resolution and NA	53
B.3	NA Analysis of Common Optical Systems	55
B.3.1	Single Lens Imaging System	55
B.3.2	Telecentric and Infinity Corrected Microscopes	58
B.3.3	Comparison between NA of Single Lens and Telescope	60
B.4	Simulations	61
B.4.1	The Spatial Simulation Parameters	63
B.4.1.1	Choice of Δx	65
B.4.2	Single Lens	67
B.4.2.1	Single Lens Ideal Phase Function	70
B.4.3	Telescope	71
B.4.4	2D Simulations	73
B.5	Spatial Invariance and Vignetting	74
APPENDIX C — NUMERICAL SIMULATIONS		79
C.1	Simulated Optical Limits to SPIFI Number of Points	79
C.2	Effects of Binary Printing	83
APPENDIX D — EXTENDED BACKGROUND INFORMATION		85
D.1	High speed imaging	85
D.1.1	Applications Requiring High speed Imaging	86
D.2	CMOS and CCD Imagers	87
D.3	Reticle Imaging	88
D.4	High Speed Scanning Microscopy	88
D.5	Structured Illumination Microscopy	88
REFERENCES		90

ACKNOWLEDGEMENTS

An undertaking such as this is rarely the work of one person alone. This is the reason why “we” is used in the text of this and most manuscripts. It is the purpose of this section the credit people who contributed to this work and to my graduate education.

First, I would like to thank my advisor Randy Bartels for the time he put into mentoring me. I came to Colorado State University with little knowledge of the fields such as optics, lasers, and imaging. Most of the knowledge I have gained in these areas have come from him and the courses he taught. Hopefully this document demonstrates great extent to which I have gained understanding in this topics. I would like to acknowledge Randy as the one who originally purposed and engaged me in the topic of SPIFI presented in this document.

I would like to thank Philip Schlup, a research scientist who worked in Randy’s group, for his motorship. Additionally Philip has contributed to this work by the generation of illustrative graphics. I found Philip to be a practical researcher with some of strongest technical and computer skills in which I have encountered. I hopefully will work more people like Philip in the course of my professional career but my current experience suggests people like him are rare.

Additionally, I would like to acknowledge all of my peers in the Bartels’ Ultra Fast Group. Specifically, David Winters in which we collaborated with to take the SPIFI fluorescent data and co-authored the associated publication. Besides David’s contributions to SPIFI , I would also like to acknowledge him for all he taught me about fiber optics.

CHAPTER I

INTRODUCTION

Optical imaging is widely used though out science to reproduce a representation of a object. The ability of lenses to perform optical imaging was known to the ancient Romans and Greeks. Yet, the philosophy of the ancients didn't conceive of anything worth seeing smaller than what is visible [1].

Shortly after the start of the modern age(16th century), the first printed works in science were being produced. One of the first widely disseminated printed works in optical imaging was [2] published by Robert Hooke in 1665. In the introduction of [2], Hooke lays out the philosophical thoughts of his time on Microscopes and Telescopes. He also describes a microscope apparatus that he used to image numerous specimens though out [2]. Hooke's diagram of his apparatus is shown in Fig. 1.1. The detection backed used by Hooke to record his images was Hooke himself. He viewed the microscopic objects using his eye and then recorded them with his hand.

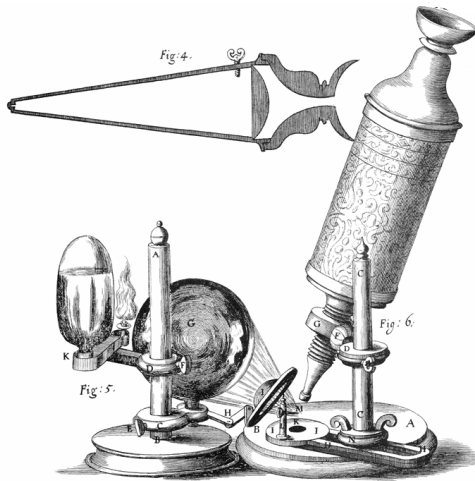


Figure 1.1: Hooke's Microscope(Fig. 6) with lens diagram(Fig. 4). The illumination source was light focused using a water globe illumination source(Fig. 5). Schematic from Micrographica [2].

Up to the 19th century, imaging system designers had no choice but to use the eye as the detector. The detection side changed in the 19th century with the discovery of the photosensitivity of silver salt and the chemical methods to fix it. Fixing or the stoping of the photosensitivity of the salt was essential for generating a lasting image. The first known fixed photograph was made by Joseph Niépce [3] titled, "View from the Window at Le Gras". Niépce process was imperfect

and he used a varnish to fix the image. His partner and collaborator Louis Daguerre would later develop a different process called the Daguerreotype that would become one of the two mainstream photographic processes of the 19th century [3]. The French government realized the importance of the Daguerreotype process and decided to purchase the patent from Daguerre and Niépce's surviving son in return for an annual pension of 6,000 and 4,000 Francs respectively and made the Daguerreotype, "Free to the World" [3].

The other mainstream photographic process of the 19th century is the Calotype invented by Henry Fox Talbot [4]. Talbot developed the Calotype photographic process in England independent of the work of Daguerre. The Calotype process differed from the Daguerreotype process in that it employed a negative in the reproduction step. One would be remiss if the work of John Herschel was not mentioned [5], as Herschel developed the soda that would become common in the fixing of photographs [6].

Currently, photographic film has been displaced by electronic detection. The interest in electronic detection was peaked by the demonstration of the photoelectric effect in 1887 by Henry Hertz [7]. The photoelectric effect coupled with the discovery of secondary electron emission [8], allowed for the invention of the photomultiplier tube(PMT) by 1935 [9].

The PMT is a single element detector and doesn't provide two dimensional(2D) image information, also referred to as wide-field, without additional optical multiplexing. Some of the early interest in electronic detection was lead by the desire to broadcast video signals. Different electronic tube designs were used to record 2D images electronically with the one of the first employed called the Iconoscope patented by Vladimir Zworykin of RCA in 1935 [10]. In a Iconoscope the optical image is captured on a photosensitive surface inside of a cathode ray tube consisting of multiple discrete elements which take on a positive charge corresponding to the optical intensity of the image. The 2D image is then read out by scanning the electron beam of the cathode ray through the photosensitive surface discharging it.

The photosensitivity of semiconductors is another physical property now commonly employed to perform electronic photo detection. It also has 19th century roots. In 1833, Michael Faraday was one of the first to examine the photoconductivity of silver sulphide reporting that its (photo)conduction increased rapidly when light from a lamp was applied to it [11]. Initial interest in semiconductors was more for their rectifying electrical characteristics than for their photosensitivity. The development of semi-conductors eventually lead to the p-n junction diode which can be used as photodetector in both photovoltaic and photoconductive modes [12].

Today, semiconductor array detectors are common in wide field image acquisition. The first

widely used 2D semiconductor imaging array was the charge coupled device(CCD) invented by Boyle, and Amelio in 1970 [13,14]. The CCD and their MOS counterparts have now replaced the tube detectors deriving from Iconoscopes as the dominant wide-field detection method.

The use of 2D array detectors avoids the need to optically multiplex the image onto a single element detector. In wavelength regimes, such as the mid-infrared, the bandgap of developed semiconductor materials such as Si, Ge, and GaAs do not match the photon energies. These wavelength regimes require the use of more exotic semiconductor materials such HgCdTe making them more difficult to construct and increasing their cost. In the mid-infrared($\lambda = 3 - 20$ (μm)) these arrayed optical detectors are called focal plane arrays(FPA) and are the subject of current research [15,16]. At the Terahertz($f = .3 - 3$ (THz)), 2D detectors are even more rare and a 2D array detector with 15 pixels is the state of the art [17]. Even in the millimeter wavelengths, 2D image arrays are more developed but do not produce excellent quantity images [18]. In these wavelength regimes methods of optical multiplexing allowing for the collection images on a single detector have become important [19].

Optical multiplexing can lower the systems cost by reducing the dimensionally the detector. In some cases this also improves system performance by allowing for the use of a more sensitive detector or by improving optical performance. The most common form of optical multiplexing is raster scanning. In a raster scan, one point of the image is relayed to the detector at a given time and the signal intensity is recorded. In this sense, the raster scan can be viewed as a time domain(TD) spatial multiplex. Raster scanning is commonly employed in laser scanning confocal microscopy [20]. In confocal microscopy, a laser beam is focused onto the sample and either the Rayleigh scattered or in the case of fluorescence frequency shifted light from the sample is descanned though a spatial filter [21] onto a sensitive single element detector such as a PMT or avalanche photodiode(APD). Descaning the signal though a spatial filter the depth localization in the image. The increased localization is also known as optical sectioning and is the reason why confocal microscopy has wide spread use in the life sciences [22]. Passing the beam though a single spatial filter allows only one part of the specimen to be measured at a time leading to the natural use of raster scanning.

In this thesis, another optical multiplex for recovering one dimensional(1D) wide-field spatial information on a single element detector is presented. The method scans spatial frequencies across the sample and records their intensity on a single element detector. In by doing this, the spatial information of the sample is present in the electronic frequency domain(FD) signal of the detector simply recorded with an analog to digital(ATD) converter and recovered through Fourier transform. In this sense the technique is the FD conjugate to raster scanning and can be considered frequency

domain(FD) spatial frequency multiplex. We call this method, SPIFI, for SPAtIal Frequency modulated Imaging. We acknowledge the acronym is a bit of a reach but it's just a name, and we desire a name that is easily pronounced.

An asymmetrical version of the mask pattern implemented in this work(Sec. 3) to perform SPIFI is referred to as the Lovell reticle [23]. The initial interest FM reticles such as the Lovell reticle was to generate an electrical signal containing optical target position tracking [24]. In 1991, Sanders, Driggers, Halford, and Griffin realized that the FM reticle would also provide wide-field 1D spatial information and demonstrated this ability experimentally [25].

We encountered the Lovell reticle in looking for a method to produce the modulation described in Eq. 2.2. In Ch. 2 the optical theory on how modulating the field with Eq. 2.2 encodes spatial information into the electrical signal of a single element detector is developed. The theory includes what parameters of the modulator and optical system set the object resolution and field of view which leads to the number of points SPIFI can resolve and includes how this relates to the image refresh rate.

The Lovell reticle has been modified to be symmetrical and we have produced a version of it on a CD-ROM substrate(Ch. 3). The object resolution of SPIFI images is ultimately limited by the highest periodicity that could be produced on the CD-ROM substrate and the largest demagnification that the optical system could perform. A detailed analysis of the general optical system characteristics is performed in Appendix B with additional numerical simulations in terms SPIFI in Appendix C.

Using the disk modulator of Ch. 3 mounted to an electrical motor, electronic images were captured with a line update rate of 80 Hz. In the disc implementation of SPIFI presented here, the line update rate of the 1D image is exactly the same as the motor rotations speed in rotations per second(RPS). A motor's spin rate is typically measured in rotations per minute(RPM), and 80 RPS corresponds to 4,800 RPM. The disk modulator mounted on the motor is similar to a CD-ROM in a CD-ROM drive. Spindle speed of a CD-ROM drive increases with the drives x factor, and a 52x CD-ROM speeds corresponds to a maximum spindle speed of 200 (RPM) x 52 or 10,400 (RPM) [26,27]. 10,400 RPM is already past the critical speed of the optical disk [28] and it is difficult to construct drives with even higher angular velocities due to increasing disk vibrations [29], which can cause disks to shatter at around 23,000 RPM [30]. Our motor was unable to exceed 6,000 RPM due to its small size, but from the observations of CD-ROM spin speeds it seems reasonable that the update rate could be increased by a factor of 2.1 to 174 Hz(10,400 RPM) with a motor upgrade.

Using the disc modulator implementation of SPIFI for one dimension and a translation stage for the second(Ch. 4) images of absorption(Fig. 4.4) and fluorescent objects(Fig. 4.10) have been

captured. The absorption objects showed a image resolution down to 150 (μm). The resolution of the absorption objects was ultimately limited by the demagnification of the optical system and could be brought to a diffraction limited performance(Sec. 2.3.1, Appendix B). The recording of fluorescent objects by using SPIFI to modulate the illumination(Sec. 2.1.3) was new and Fig. 4.10 contains first reported images recorded.

SPIFI 's impact is focused on in the conclusion(Ch. 5). Emphasis is placed on applying SPIFI in regions of the electromagnetic spectrum where 2D array detectors are less developed such in the terahertz. Improvement to SPIFI , in the 1D sense using the disc modulator presented in this work, are discussed in the future work and are applicable regardless of the spectral region of interest. In addition the longer term research goals taking SPIFI 2D are also discussed and the high speed 2D version of SPIFI using an 1D array detector for the second dimension is purposed.

1.1 Contributions

This imaging method was first demonstrated by [25]. We have developed the imaging theory of this method which we are calling SPIFI . Our theory explains the mapping from space to electrical frequency, resolution limits, the effects of time windows, the number of points, and dynamic range(Ch. 2). Additionally, we developed a model of disc non concentricity(Sec. 3.2), and a method to correct for it(Sec. 3.3).

We have implemented opto-mechanical modulator to produce the required modulation of SPIFI . The modulator is similar to the pattern first created by [23]. The modulator consists of an absorption pattern printed onto a clear CD-ROM disc and is presented in Ch. 3 and Ch. 4.

Using this modulator we have captured images of a 1954 Air Force test pattern in a absorption configuration(Fig. 4.4). These images appear of higher quality than that in [25]. We are the first to use a reticle modulator to perform imaging of florescence(Fig. 4.10) and we have compared the SPIFI modulated florescence to SPIFI absorption images(Ch. 4).

CHAPTER II

THEORY OF SPIFI

2.1 *The Modulated Field at the Detector*

The underlying principle of SPIFI is that by varying the modulation frequency across the spatial extend of the field spatial information of the field is encoded into its temporal content. Having a field with temporally encoded spatial information allows for recovery of its spatial information on a single element detector.

For the sake of simplicity, the magnifications between modulator, object, and image planes have been dropped, and the field is assumed to be completely captured on the detector's area. For an analysis that includes the magnifications see Appendix A.2.

2.1.1 SPIFI modulated illumination

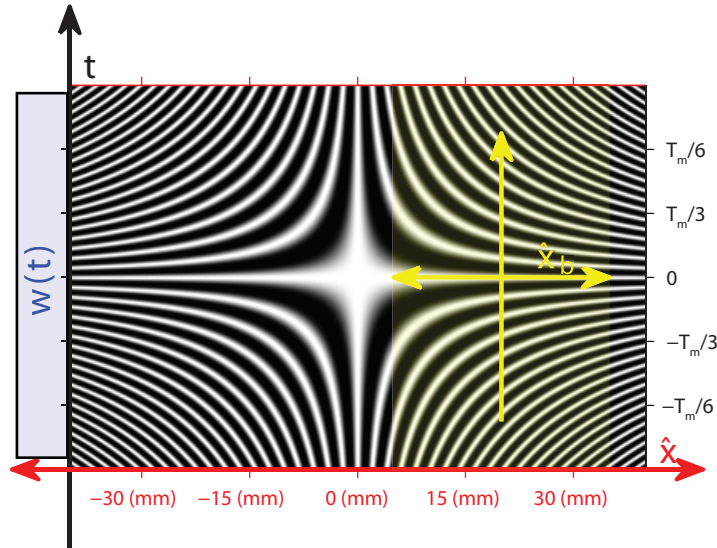


Figure 2.1: Diagram of the unwrapped modulator, $m(x, t)$ of Eq. 2.2, white indicates transmission and black absorpoin/reflectance. The region the illumination beam occupies is shown in yellow, it's centroid position, x_c is indicated by the yellow vertical line.

When SPIFI is setup in a modulated illumination configuration, an illumination field, $E_0 u(x) e^{j\omega_0 t}$, shown in yellow Fig. 2.1 is first modulated with the SPIFI modulator, $m(x, t)$, the black and white

pattern in Fig. 2.1 such that immediately behind the modulator the field is a product of the illumination field and modulator, $u(x)m(x, t)$. This field is imaged to the object plane, containing an absorptive object with transmission function, $g(x)$, producing a field distribution behind the transmission object of $E_0u(x)g(x)m(x, t)e^{j\omega_0 t}$. This transmitted field through the object is then relayed with a second imaging system onto the single element area of a electronic photo-detector.

Assuming the detector to be square law in nature, such as is the case for a photo-diode, the detector produces a output signal $s(t) = \gamma \int I(x, t)$, where the multiplied constant γ is the detector efficiency, and $I(x, t)$ is the square law intensity of the field on the detector

$$I(x, t) = I_0|u(x)g(x)m(x, t)|^2 \quad (2.1)$$

where $I_0 = \frac{1}{2}\eta\epsilon_0 E_0^2$.

For the electronic square law signal to contain spatial information, a modulator that maps local space to temporal frequency is required. A amplitude modulator, $m(x, t)$

$$m(x, t) = \frac{w(t)}{2} [1 + \cos(2\pi\kappa x t)] \quad (2.2)$$

has a local temporal frequency chirp of, κx , and a local spatial frequency chirp of κt . Since neither of these things can increase indefinitely, the chirped cosine is windowed by a rectangular window, $w(t) = \text{rect}\left(\frac{t}{T_m}\right)$, where T_m is the duration of the modulation.

This modulator is shown unwrapped in time in Fig. 2.1. It is origin, $x = 0$, point is displaced from the center of the illumination field by distance x_c such that the illumination field does not extend beyond the DC frequency of the modulator. If the illumination field crosses the DC frequency of the modulator each electronic frequency will correspond two to spatial locations.

The shifted modulator, $m(x - x_c, t)$, will generate the square-law signal out of the detector

$$s(t) = \gamma \frac{I_0}{4} \int |u(x)g(x)|^2 |w(t)|^2 \left[\frac{3}{2} + 2 \cos(2\pi\kappa t x - 2\pi\kappa t x_c) + \frac{1}{2} \cos(4\pi\kappa t x - 4\pi\kappa t x_c) \right] dx \quad (2.3)$$

which can be separated in terms of harmonics and scaled by γ and I_0 , to be written as $s(t) = \frac{1}{4} I_0 \gamma [s_0(t) + s_1(t) + s_2(t)]$. $s_0(t) = |w(t)|^2 \int \frac{3}{4} |u(x)g(x)|^2 dx$ is a constant power term stationary in time. The time dependent signals s_1 and s_2 are the first and second harmonic bands of the modulation frequency,

$$s_1(t) = |w(t)|^2 e^{j2\pi\kappa t x_c} \int |u(x)g(x)|^2 e^{j2\pi\kappa t x} dx + \text{c.c.} \quad (2.4)$$

$$s_2(t) = \frac{1}{4} |w(t)|^2 e^{j4\pi\kappa t x_c} \int |u(x)g(x)|^2 e^{j4\pi\kappa t x} dx + \text{c.c.} \quad (2.5)$$

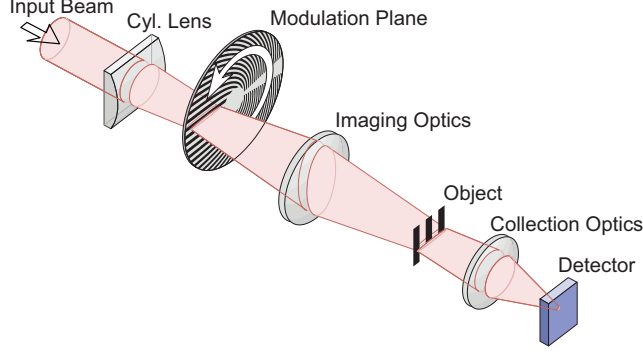


Figure 2.2: Experimental Setup

centered at temporal frequencies $f_c = \kappa x_c$, $2f_c = 2\kappa x_c$.

Eq. 2.4 is of the form of a spatial Fourier transform, where the spatial frequency $f_x \rightarrow \kappa t$. With this identification and defining the spatial Fourier transform as

$$\mathcal{G}'(f_x) = \int |u(x)g(x)|^2 e^{j2\pi f_x x} dx \equiv \mathfrak{F} \{ |u(x)g(x)|^2 \}, \quad (2.6)$$

we obtain an expression for the time-varying photodiode signal of

$$s_1(t) = 2|w(t)|^2 |\mathcal{G}'(\kappa t)| \cos(2\pi f_c t + \angle \mathcal{G}'(\kappa t)) \quad (2.7)$$

where $\angle \mathcal{G}'$ is the phase of the spatial frequency distribution, \mathcal{G}' , and the center frequency is $f_c = \kappa x_c$. The Fourier transform of the temporal signal, $\hat{S}_1(f) = \mathfrak{F} \{ s_1(t) \}$, shows a spectrum with conjugate symmetric sidebands decomposed as $\hat{S}_1(f) = \kappa^{-1} \hat{S}_{1+}(-f) + \kappa^{-1} \hat{S}_{1-}(f)$. The sidebands are the spatial extent of the illuminated intensity limited in resolution by convolution with the temporal window. The upper side band can be written as

$$\hat{S}_{1+}(x' = f\kappa^{-1}) = \mathcal{W}(\kappa x') \otimes |u(x')g(x')|^2 \quad (2.8)$$

where f is the frequency of the electronic signal, and \otimes is the convolution operator. The Fourier transform of the finite time window of the modulator defines the equivalent point spread function (PSF) of the system given by $\mathcal{W}(x') = \mathfrak{F} \{ |w(t)|^2 \}_{f=x'\kappa^{-1}}$.

2.1.2 Field Modulated SPIFI

The order of the two imaging systems can be reversed. If the input beam contains just a line of the field of interest, $u_1(x)$, this can be imaged onto the modulator can be inserted at this place. The modulated field $u_1(x, t)m(x, t)$ can be relayed onto the square-law single element detector producing a signal out of a square law detector of

$$s(t) = \gamma \frac{I_0}{4} \int |u_1(x)|^2 |w(t)|^2 \left[\frac{3}{2} + 2 \cos(2\pi \kappa t x) + \frac{1}{2} \cos(4\pi \kappa t x) \right] dx \quad (2.9)$$

This is the configuration used in [25].

This signal is of the form as Eq. 2.3, setting $u(x)g(x) = u_1(x)$ one sees in the spectral domain of the electrical signal contains a waveform of the incident field $|u_1(x)|$ convolved with a point spread function of $W(\kappa x')$.

$$\hat{S}_{1+}(x' = f\kappa^{-1}) = \mathcal{W}(\kappa x') \otimes |u_1(x')|^2 \quad (2.10)$$

2.1.3 SPIFI Pumped Fluorescence

Sec. 2.1.1 considered recovery of the transmission object, $g(x)$, illuminated with the modulated monochromatic illuminating field $E_0 u(x)m(x,t)e^{jw_0 t}$. The loss of transmission could be to reflections or absorptions of the field at the object plane. If the object is purely absorptive, then the spatial extent of the intensity absorption of the object can be written as

$$|a(x,t)|^2 = |a(x)|^2 |m(x,t)|^2 \quad (2.11)$$

where $|a(x)|^2 = (1 - |g(x)|^2) I_0 |u(x)|^2$ the spatial extent of the absorbed intensity

If the object fluorescence a percentage, β , of the field power will be readmitted at new optical frequency, w_0 , the readmission will can be modeled as a impulse response of

$$h(t) = \begin{cases} \beta e^{-\frac{t}{\tau_f}} e^{-jw_1 t}; & t > 0 \\ 0; & otherwise \end{cases} \quad (2.12)$$

where τ_f is the florescent life time producing a emitted field at a new wavelength

$$v(x,t) = h(t) \otimes |a(x)| |m(x,t)| \quad (2.13)$$

The fluorescent field can be separated from the pump field with optical filters and be imaged onto the area of a square law detector. The square law detector will produce a output signal of

$$s(t) = \gamma \frac{I_0}{4} |h(t)|^2 \otimes \int |a(x)|^2 |w(t)|^2 \left[\frac{3}{2} + 2 \cos(2\pi\kappa t x) + \frac{1}{2} \cos(4\pi\kappa t x) \right] dx \quad (2.14)$$

This is the same integral as Eq. 2.3, setting $|u(x)g(x)|^2 = |a(x)|^2$ the integral can be separated into the three harmonic terms, $s_0(t)$, $s_1(t)$, and $s_2(t)$ the same as in Sec. 2.1.1. The recovered signal can be written as

$$s(t) = \gamma \frac{I_0}{4} h(t) \otimes [s_0(t) + s_1(t) + s_2(t)] \quad (2.15)$$

Transferring the impulse response Eq. 2.12 to the frequency domain, $\hat{H}(f) = \mathfrak{F}\{|h(t)|^2\}$ the first upper side band of the electrical signal,

$$\hat{S}_{1+}(x' = f\kappa^{-1}) = H(\kappa x') \mathcal{W}(\kappa x') \otimes |a(x')|^2 \quad (2.16)$$

contains the information about the distribution of the absorption $|a(x')|^2$. Absorption time constants are typically in the high nano to pico second regimes. Therefore the bandwidth of the frequency response $H(f)$ is just equal to the florescent efficiency $H(f) = |\beta|^2$ and the frequency response is assumed to be flat over this regime leaving

$$\hat{S}_{1+}(x' = f\kappa^{-1}) = \mathcal{W}(\kappa x') \circledast |\beta a(x')|^2 \quad (2.17)$$

where $|\beta a(x')|^2$ is the intensity distribution of the florescence emission.

2.2 SPIFI Derivation Using Parseval's Theorem

The signal out of the square law detector can also be derived in the spatial frequency domain using Parseval's relation. This derivation gives more physical insight as to the terms that are mixing in the generation of the three harmonic signals, $s_0(t)$, $s_1(t)$, and $s_2(t)$.

For SPIFI the field distribution on the detector can be written as

$$e(x) = w(t)v(x) \left(\frac{1}{2} + \frac{1}{2} \cos 2\pi(f_c + \kappa x)t \right) \quad (2.18)$$

where $v(x) = u(x)g(x)$. As usual the interest is in the square law signal coming out of the spatial integrating detector, which is equivalent in space and spatial frequency from Parseval's Theorem,

$$s(t) = \int_{-\infty}^{\infty} |e(x)|^2 dx = \int_{-\infty}^{\infty} |\hat{E}(f_x)|^2 df_x \quad (2.19)$$

where $\mathfrak{F}\{e(x)\} = \hat{E}(f_x)$ is the spatial fourier transform of $e(x)$. $\hat{E}(f_x)$ can be written as

$$\hat{E}(f_x) = \frac{1}{2}\hat{V}(f_x) + \frac{1}{4}\hat{V}(f_x - \kappa t)e^{-j2\pi f_c t} + \frac{1}{4}\hat{V}(f_x + \kappa t)e^{+j2\pi \alpha t} \quad (2.20)$$

we are interested in $|\hat{E}(f_x)|^2$. This is

$$\begin{aligned} |\hat{E}(f_x)|^2 = |w(t)|^2 & \left(\frac{1}{2}\hat{V}(f_x) + \frac{1}{4}\hat{V}(f_x - \kappa t)e^{-j2\pi f_c t} + \frac{1}{4}\hat{V}(f_x + \kappa t)e^{+j2\pi f_c t} \right) \left(\right. \\ & \left. \frac{1}{2}\hat{V}^*(f_x) + \frac{1}{4}\hat{V}^*(f_x - \kappa t)e^{+j2\pi f_c t} + \frac{1}{4}\hat{V}^*(f_x + \kappa t)e^{-j2\pi f_c t} \right) \end{aligned} \quad (2.21)$$

Performing the multiplication leads to a equation for $|\hat{E}(f_x)|^2$ with nine terms

$$\begin{aligned} |\hat{E}(f_x)|^2 = |w(t)|^2 & \left[\frac{1}{4}\hat{V}(f_x)\hat{V}^*(f_x) + \frac{1}{8}\hat{V}(f_x)\hat{V}^*(f_x - \kappa t)e^{+j2\pi f_c t} + \frac{1}{8}\hat{V}(f_x)\hat{V}^*(f_x + \kappa t)e^{-j2\pi f_c t} \right. \\ & + \frac{1}{8}\hat{V}(f_x - \kappa t)\hat{V}^*(f_x)e^{-j2\pi f_c t} + \frac{1}{16}\hat{V}(f_x - \kappa t)\hat{V}^*(f_x - \kappa t) + \frac{1}{16}\hat{V}(f_x - \kappa t)\hat{V}^*(f_x + \kappa t)e^{-j4\pi f_c t} \\ & \left. + \frac{1}{8}\hat{V}(f_x + \kappa t)\hat{V}^*(f_x)e^{+j2\pi f_c t} + \frac{1}{16}\hat{V}(f_x + \kappa t)\hat{V}^*(f_x - \kappa t)e^{+j4\pi f_c t} + \frac{1}{16}\hat{V}(f_x + \kappa t)\hat{V}^*(f_x + \kappa t) \right] \end{aligned} \quad (2.22)$$

This looks like a Hermitian matrix with conjugate symmetry about the diagonal. This makes sense since the signal is real. The DC terms are across the diagonal and consist of the DC, and the two

modulated spatial frequencies mixing with themselves. The off diagonal terms are they only ones that carry a temporal modulation. The first harmonic terms are the ones multiplied by $e^{j2\pi f_c t}$ and $e^{-j2\pi f_c t}$ and are associated with the mixing of the sweeping spatial frequency distribution $\hat{V}(f_x \pm \kappa t)$, mixing with DC spatial frequency distribution, $\hat{V}(f_x)$. The second harmonic terms are caused by the mixing of $\hat{V}(f_x + \kappa t)$ with $\hat{V}(f_x - \kappa t)$.

The first harmonic signal can be separated out as

$$s_1(t) = |w(t)|^2 \int_{-\infty}^{\infty} \frac{1}{8} \hat{V}(f_x) \hat{V}^*(f_x - \kappa t) e^{+j2\pi f_c t} + \frac{1}{8} \hat{V}(f_x) \hat{V}^*(f_x + \kappa t) e^{-j2\pi f_c t} + \frac{1}{8} \hat{V}(f_x - \kappa t) \hat{V}^*(f_x) e^{-j2\pi f_c t} + \frac{1}{8} \hat{V}(f_x + \kappa t) \hat{V}^*(f_x) e^{+j2\pi f_c t} df_x \quad (2.23)$$

We are interested in recovering the spatial intensity of the field, $|v(x)|^2 = |u(x)g(x)|^2$. We previously defined the Fourier transform of $|v(x)|^2$ as $\mathcal{G}'(f_x)$, this is also the autocorrelation of the fields spatial frequency distribution

$$\mathcal{F}\{|v(x)|^2\} = \mathcal{G}'(f_x) = \int_{-\infty}^{\infty} \hat{V}(f'_x) \hat{V}^*(f'_x - f_x) df'_x \quad (2.24)$$

The terms in Eq. 2.23 are just this autocorrelation function $\mathcal{G}'(f_x)$, evaluated for $f_x = \pm \kappa t$. Making the substations

$$s_1(t) = \frac{1}{4} |w(t)|^2 [\mathcal{G}'(\kappa t) e^{j2\pi f_c t} + \mathcal{G}'(-\kappa t) e^{-j2\pi f_c t}] \quad (2.25)$$

Since $|v(x)|$ must be real $\mathcal{G}'(-\kappa t) = \mathcal{G}'^*(\kappa t)$. This allows $s_1(t)$ to be written as

$$s_1(t) = \frac{1}{2} |w(t)|^2 |\mathcal{G}'(\kappa t)| \cos(2\pi f_c t + \angle \mathcal{G}'(\kappa t)) \quad (2.26)$$

which is Eq. 2.7 times a multiplicative constant.

2.3 Effect of optical diffraction on the SPIFI image

So far the distribution of the field on the square law detector hasn't considered the effect of diffraction. Diffraction has the effect of windowing the spatial frequencies that can be transferred onto the area of the detector. Here we will look how diffraction effects the SPIFI image for SPIFI modulated illumination in the coherent case, and for field modulated SPIFI in the incoherent case.

2.3.1 Optical diffraction in coherent SPIFI modulated illumination

For SPIFI modulated coherent illumination of a transmission object, such as performed in Ch. 4, there are two optical relay systems that modify the field distribution of the SPIFI square law signal. The effect of these systems can be modeled with a complex point spread function(PSF), $p(x)$, and complex amplitude transfer function(ATF), $\hat{P}(f_x)$. These two functions are related by fourier transform $\mathfrak{F}\{p(x)\} = \hat{P}(f_x)$.

Since there are two optical systems, two PSFs/ATFs will be used to separate their diffraction effects. The first $\mathfrak{F}\{p_1(x)\} = \hat{P}_1(f_x)$, is associated with the optical system that transfers the modulated illumination field, $u(x)m(x, t)$ to the object plane. Considering the diffraction effect of this optical system, the field at the object plane can be written as

$$e_{\text{obj}}(x) = w(t)u(x) \left(\frac{1}{2} + \frac{1}{2} \cos 2\pi(f_c + \kappa x)t \right) \otimes p_1(x) \quad (2.27)$$

or in the spatial frequency domain as

$$\hat{E}_{\text{obj}}(f_x) = \frac{1}{2}w(t) \left[\hat{U}(f_x) + \frac{1}{4}\hat{U}(f_x - \kappa t)e^{-j2\pi f_c t} + \frac{1}{4}\hat{U}(f_x + \kappa t)e^{+j2\pi f_c t} \right] \hat{P}_1(f_x) \quad (2.28)$$

The spatial extent of the field at the object plane is multiplied against the transmission object, $g(x)$, and imaged with a second imaging system described by $\mathfrak{F}\{p_2(x)\} = \hat{P}_2(f_x)$ onto the square-law detector. With the diffraction effect of the second system also considered, the field on the square law detector can be written as

$$e_{\text{det}}(x) = w(t) \left[u(x) \left(\frac{1}{2} + \frac{1}{2} \cos 2\pi(f_c + \kappa x)t \right) \otimes p_1(x) \right] g(x) \otimes p_2(x) \quad (2.29)$$

or in the spatial frequency domain as

$$\hat{E}_{\text{det}}(f_x) = \frac{1}{2}w(t)\hat{P}_2(f_x) \left\{ \left[\hat{U}(f_x) + \frac{1}{4}\hat{U}(f_x - \kappa t)e^{-j2\pi f_c t} + \frac{1}{4}\hat{U}(f_x + \kappa t)e^{+j2\pi f_c t} \right] \hat{P}_1(f_x) \otimes G(f_x) \right\} \quad (2.30)$$

As discussed in Sec. 2.2, the signal out of the square law detector can be written as

$$s(t) = \int_{-\infty}^{\infty} |\hat{E}_{\text{det}}(f_x)|^2 df_x \quad (2.31)$$

$|\hat{E}_{\text{det}}(f_x)|^2$ contains nine terms similar to Eq. 2.22. It can be written out as

$$\begin{aligned} |\hat{E}(f_x)|^2 &= |w(t)|^2 |\hat{P}_2(f_x)|^2 \left\{ \frac{1}{4} \left[\hat{U}(f_x)\hat{P}_1(f_x) \otimes \hat{G}(f_x) \right] \left[\hat{U}^*(f_x)\hat{P}_1^*(f_x) \otimes \hat{G}^*(f_x) \right] \right. \\ &\quad + \frac{1}{8} \left[\hat{U}(f_x)\hat{P}_1(f_x) \otimes \hat{G}(f_x) \right] \left[\hat{U}^*(f_x - \kappa t)\hat{P}_1^*(f_x) \otimes \hat{G}^*(f_x) \right] e^{+j2\pi f_c t} \\ &\quad + \frac{1}{8} \left[\hat{U}(f_x)\hat{P}_1(f_x) \otimes \hat{G}(f_x) \right] \left[\hat{U}^*(f_x + \kappa t)\hat{P}_1^*(f_x) \otimes \hat{G}^*(f_x) \right] e^{-j2\pi f_c t} \\ &\quad + \frac{1}{8} \left[\hat{U}(f_x - \kappa t)\hat{P}_1(f_x) \otimes \hat{G}(f_x) \right] \left[\hat{U}^*(f_x)\hat{P}_1^*(f_x) \otimes \hat{G}^*(f_x) \right] e^{-j2\pi f_c t} \\ &\quad + \frac{1}{16} \left[\hat{U}(f_x - \kappa t)\hat{P}_1(f_x) \otimes \hat{G}(f_x) \right] \left[\hat{U}^*(f_x - \kappa t)\hat{P}_1^*(f_x) \otimes \hat{G}^*(f_x) \right] \\ &\quad + \frac{1}{16} \left[\hat{U}(f_x - \kappa t)\hat{P}_1(f_x) \otimes \hat{G}(f_x) \right] \left[\hat{U}^*(f_x + \kappa t)\hat{P}_1^*(f_x) \otimes \hat{G}^*(f_x) \right] e^{-j4\pi f_c t} \\ &\quad + \frac{1}{8} \left[\hat{U}(f_x + \kappa t)\hat{P}_1(f_x) \otimes \hat{G}(f_x) \right] \left[\hat{U}^*(f_x)\hat{P}_1^*(f_x) \otimes \hat{G}^*(f_x) \right] e^{+j2\pi f_c t} \\ &\quad + \frac{1}{16} \left[\hat{U}(f_x + \kappa t)\hat{P}_1(f_x) \otimes \hat{G}(f_x) \right] \left[\hat{U}^*(f_x - \kappa t)\hat{P}_1^*(f_x) \otimes \hat{G}^*(f_x) \right] e^{+j4\pi f_c t} \\ &\quad \left. + \frac{1}{16} \left[\hat{U}(f_x + \kappa t)\hat{P}_1(f_x) \otimes \hat{G}(f_x) \right] \left[\hat{U}^*(f_x + \kappa t)\hat{P}_1^*(f_x) \otimes \hat{G}^*(f_x) \right] \right\} \end{aligned} \quad (2.32)$$

In Sec. 2.2, the term $\hat{V}(f_x \pm kt) = \hat{U}(f_x \pm kt) \otimes \hat{G}(f_x)$ was of interest, consideration of the diffraction effect of the first relay system modifies this to be

$$\hat{U}(f_x \pm kt) \hat{P}_1(f_x) \otimes \hat{G}(f_x) = \int_{-\infty}^{\infty} \hat{U}(f'_x \pm kt) \hat{P}_1(f'_x) \hat{G}(f_x - f'_x) df'_x \quad (2.33)$$

which is still a cross correlation integral but windowed by the amplitude transfer function of the system $\hat{P}_1(f_x)$. For a aberration free hard aperture system, the ATF take the form

$$\hat{P}_1(f_x) = \text{rect} \left(\frac{\lambda f_x}{2NA_1} \right) \quad (2.34)$$

A broad illumination beam, as one would use to illuminate wide field of view, has a narrow spatial frequency distribution, $\hat{U}(f_x)$. For the time dependent spatial frequency terms, the center spatial frequency of this distribution sweeps as a function of time. As long as this narrow spatial frequency distribution is under the aperture window,

$$\hat{U}(f_x \pm kt) \hat{P}_1(f_x) \otimes \hat{G}(f_x) = \hat{U}(f_x \pm kt) \otimes \hat{G}(f_x) \quad (2.35)$$

otherwise, Eq. 2.33 is equal to zero. This allows the $\text{rect}()$ to be pulled out front,

$$\hat{U}(f_x \pm kt) \hat{P}_1(f_x) \otimes \hat{G}(f_x) = \text{rect} \left(\frac{\lambda \kappa t}{2NA_1} \right) \left(\hat{U}(f_x \pm kt) \otimes \hat{G}(f_x) \right) \quad (2.36)$$

or $\hat{P}_1(f_x) \hat{U}(f_x \pm kt) \otimes \hat{G}(f_x) = \text{rect} \left(\frac{\lambda \kappa t}{2NA_1} \right) \hat{V}(f_x \pm kt)$. $\hat{P}_1(f_x)$ also limits the convolution of the DC term. Assuming that $\hat{G}(f_x)$ is already band limited shorter than the rectangular ATF, the effect is minimal and

$$\hat{U}(f_x) \hat{P}_1(f_x) \otimes \hat{G}(f_x) = \hat{V}(f_x). \quad (2.37)$$

Taking assumption of broad illumination beam, Eq. 2.35, and assuming the effect of $\hat{P}_1(f_x)$ to the DC part of input beam to be negligible, Eq. 2.37, the mess of Eq. 2.32 can be rewritten as

$$\begin{aligned} |\hat{E}(f_x)|^2 = \frac{1}{4} |w(t)|^2 |\hat{P}_2(f_x)|^2 \hat{V}(f_x) \hat{V}^*(f_x) + |w(t)|^2 |\hat{P}_2(f_x)|^2 \text{rect} \left(\frac{\lambda \kappa t}{2NA_1} \right) \left[\right. \\ \left. \begin{aligned} & 0 + \frac{1}{8} \hat{V}(f_x) \hat{V}^*(f_x - \kappa t) e^{+j2\pi f_c t} + \frac{1}{8} \hat{V}(f_x) \hat{V}^*(f_x + \kappa t) e^{-j2\pi \alpha t} \\ & + \frac{1}{8} \hat{V}(f_x - \kappa t) \hat{V}^*(f_x) e^{-j2\pi f_c t} + \frac{1}{16} \hat{V}(f_x - \kappa t) \hat{V}^*(f_x - \kappa t) + \frac{1}{16} \hat{V}(f_x - \kappa t) \hat{V}^*(f_x + \kappa t) e^{-j4\pi f_c t} \\ & + \frac{1}{8} \hat{V}(f_x + \kappa t) \hat{V}^*(f_x) e^{+j2\pi f_c t} + \frac{1}{16} \hat{V}(f_x + \kappa t) \hat{V}^*(f_x - \kappa t) e^{+j4\pi f_c t} + \frac{1}{16} \hat{V}(f_x + \kappa t) \hat{V}^*(f_x + \kappa t) \end{aligned} \right] \end{aligned} \quad (2.38)$$

The second optical system simply acts to set the limits of integration of the autocorrelation integral, Eq. 2.24. This integral is thus changed to

$$\mathcal{Q}'(f_x) = \int_{-\infty}^{\infty} |\hat{P}_2(f_x)|^2 \hat{V}(f'_x) \hat{V}^*(f'_x - f_x) df'_x \quad (2.39)$$

and the time domain signal is

$$s_1(t) = \frac{1}{2}|w(t)|^2 \text{rect}\left(\frac{\lambda\kappa t}{2NA_1}\right) |\mathcal{Q}'(kt)| \cos(2\pi f_c t + \angle\mathcal{Q}'(kt)) \quad (2.40)$$

$|\hat{P}_2(f_x)|^2$ sets the limits of integration on the autocorrelation integral. Since this is the magnitude square of the ATF of the second optical system, the phase on the ATF doesn't effect the SPIFI image. The phase on the ATF can be associated with either the object or detector being displaced from their conjugate planes. Since is $|\hat{P}_2(f_x)|^2$ this displacement doesn't matter, all that is important is that the modulated spatial frequency bandwidth of the object is captured.

If second optical system is assumed to be associated with a hard aperture then $|\hat{P}_2(f_x)|^2 = \text{rect}\left(\frac{\lambda f_x}{2NA_2}\right)$ and

$$\mathcal{Q}'(f_x) = \text{rect}\left(\frac{\lambda\kappa t}{2NA_1}\right) \int_{-\infty}^{\infty} \text{rect}\left(\frac{\lambda f'_x}{2NA_2}\right) \hat{V}(f'_x) \hat{V}^*(f'_x - f_x) df'_x \quad (2.41)$$

When the autocorrelation sweeps outside of the aperture, $\mathcal{Q}'(f_x)$ is not approximately equal to $\mathcal{G}'(f_x)$, thus the modified first harmonic signal windowed by the two apertures can be written as

$$s_1(t) = \frac{1}{2}|w(t)|^2 \text{rect}\left(\frac{\lambda\kappa t}{2NA_1}\right) \text{rect}\left(\frac{\lambda\kappa t}{2NA_2}\right) |\mathcal{G}'(kt)| \cos(2\pi f_c t + \angle\mathcal{G}'(kt)) \quad (2.42)$$

Assuming a rectangular modulator window, $w(t) = \text{rect}\left(\frac{t}{T_m}\right)$, the effective time window should can be written as the minimum of the time window of the modulator and that of the NA ,

$$T_{\text{eff}} = \min\left\{T_m, \frac{2NA_1}{\lambda\kappa}, \frac{2NA_2}{\lambda\kappa}\right\} \quad (2.43)$$

which produces the result

$$s_1(t) = \frac{1}{2} \text{rect}\left(\frac{t}{T_{\text{eff}}}\right) |\mathcal{G}'(kt)| \cos(2\pi\alpha t + \angle\mathcal{G}'(kt)) \quad (2.44)$$

2.3.2 Optical diffraction for incoherent field modulated SPIFI

For the case of incoherent field modulated SPIFI we assume the line field of interest, now simply denoted as $v(x)$ is modulated by the SPIFI modulator $m(x, t)$. Then imaged onto the area of the square law detector, by the imaging system characterized by the complex function $p(x)$. The square law field at the detector plane can be written as

$$|e(x, t)|^2 = |v(x)m(x, t)|^2 \otimes |p(x)|^2 \quad (2.45)$$

This changes Eq. 2.3 to

$$s(t) = \gamma \frac{I_0}{4} |w(t)|^2 \int |u(x)g(x)|^2 \otimes |p(x)|^2 \left[\frac{3}{2} + 2 \cos(2\pi\kappa t x - 2\pi\kappa t x_c) + \frac{1}{2} \cos(4\pi\kappa t x - 4\pi\kappa t x_c) \right] dx \quad (2.46)$$

and leads to a first harmonic signal of

$$s_1(t) = 2|w(t)|^2 \hat{O}(\kappa t) |\mathcal{G}'(\kappa t)| \cos(2\pi f_c t + \angle \mathcal{G}'(\kappa t)) \quad (2.47)$$

where $\hat{O}(f_x) = \{|p(x)|^2\}$. $\hat{O}(f_x)$ is called the optical transfer function(OTF) of the optical system and is equal to $\hat{O}(f_x) = \hat{P}(f_x) \otimes \hat{P}(-f_x)$ where $\hat{P}(f_x) = \{p(x)\}$

For the case of a diffraction limited system, $\hat{P}(f_x) = \text{rect}\left(\frac{\lambda f_x}{2NA}\right)$ and

$$\hat{O}(f_x) = \text{tri}\left(\frac{\lambda f_x}{2NA}\right) \quad (2.48)$$

where $\text{tri}(x) = \text{rect}\left(\frac{x}{2}\right)(1 - |x|)$, also defined as $\mathfrak{F}\{\text{tri}(x)\} = \mathfrak{F}\{\text{rect}(x)\}^2$. Eq. 2.47 can be written as

$$s_1(t) = 2|w(t)|^2 \text{rect}\left(\frac{\lambda \kappa t}{4NA}\right) \text{tri}\left(\frac{\lambda \kappa t}{2NA}\right) |\mathcal{G}'(\kappa t)| \cos(2\pi f_c t + \angle \mathcal{G}'(\kappa t)) \quad (2.49)$$

The recovered spatial information is now convolved with the point spread function, $|p(x)|^2$ in addition to the time window

$$\hat{S}_{1+}(x' = f\kappa^{-1}) = \mathcal{W}(\kappa x') \otimes |p(x)|^2 \otimes |u(x')g(x')|^2 \quad (2.50)$$

2.4 Resolution and Number of Points

For any imaging system, two of the most relevant system characteristics are the spatial resolution and the number of points resolved. The ability to resolve two closely spaced points in an image is characterized by the numerical aperture, NA, of the imaging system [31]. The numerical aperture is defined through $NA = n \sin \theta_{\max}$, where n is the local index of refraction, and θ_{\max} is the largest angle collected by the imaging system [32]. The definition of spatial frequencies, f_x , of an object $f_x \lambda = \sin \theta$ [33] means that the numerical aperture can also be given by $NA = n \lambda f_{x_{\max}}$, where $f_{x_{\max}}$ is the maximum spatial frequency collected. This is discussed in detail in Appendix B.

In SPIFI, time in the electronic signal is linearly related to the spatial frequency through the chirp parameter, $f_x = \kappa t$. As a result, the equivalent numerical aperture is given by $NA = \frac{1}{2} \lambda \kappa T_m$, where T_m is the duration of the modulator time-window, $w(t)$. The Rayleigh spatial resolution is then (in 1D) $\delta x = \lambda(2NA)^{-1}$, equivalent to $\delta x = (2f_{x_{\max}})^{-1}$ which for SPIFI gives a resolution $\delta x = (\kappa T_m)^{-1}$, the highest spatial frequency sampled on the mask.

The number of spatially resolved points, N , is given by the beam width, W divided by the spatial resolution, δx . Making the substitutions for SPIFI, the number of spatial points is $N = W/\delta x = \kappa W T_m$, which is the same as the space-spatial frequency bandwidth product, $N = 2W f_{x_{\max}}$. For the temporal signal, the number of points is the modulated bandwidth, Δf_m , divided by the resolution bandwidth, δf . The resolution bandwidth δf is the inverse of the acquisition duration, T_m , leading

to the time-bandwidth product, $N = \Delta f_m T_m$. For SPIFI the signal bandwidth is $\Delta f_m = \kappa W$, and the resolution bandwidth of the trace is T_m^{-1} , giving a temporal number of points $\kappa W T_m$, identical to the spatial-spatial frequency bandwidth product. One limit on both the number of points and the resolution is seen to be based on the modulator design and is independent of the wavelength of the illumination.

2.5 *Dynamic Range*

SPIFI captures the modulated spatial information on a single element photodiode. Photodiodes generate an electron hole pair for each absorbed photon leading to a current out of the device. The current out can thus be written as

$$s(t) = \int_{-\infty}^{\infty} \gamma I(x, t) dx \quad (2.51)$$

Sec. 2.1 showed that the transform of this contains the spatial information of the beam.

We will now explore the signal to noise ratio of the SPIFI image. The SNR will be defined in the electrical sense as the ratio between the electrical power spectral density(PSD) of the signal, $P_s(f)$ divided by the electrical PSD of $P_n(f)$ the noise.

$$SNR(f) = \frac{P_s(f)}{P_n(f)} \quad (2.52)$$

The electrical PSD of the signal can be written in terms of its current PSD $|S(f)|^2$ or its voltage PSD $|V_s(f)|^2$ as both are related by ohms law through the sensing resistance R_s . For noise, the same relation holds, and the current, $\sigma_N^2(f)$ or voltage PSD can be used. In terms of SNR, changes between, the use of electrical power, electrical current, or electrical voltage doesn't matter as the resistances cancel and all three ratios are equal. Since the signal in the experiment is the photoconductive current from a diode, the electrical current SNR is

$$SNR(f) = \frac{|S(f)|^2}{\sigma_N^2(f)} \quad (2.53)$$

where, $S(f) = \mathfrak{F}\{s(t)\}$.

$\sigma_N^2(f)$ can have multiple contributors. The common ones are shot noise, $\sigma_s^2(f)$ and thermal noise $\sigma_T^2(f)$, both are white. Systems may also have instrumentation noise, $\sigma_I(f)$. Since these noise mechanisms are uncorrelated, they add in PSD and sum in $\sigma_N^2(f)$

$$\sigma_N^2(f) = \sigma_s^2(f) + \sigma_T^2(f) + \sigma_I^2(f) \quad (2.54)$$

The current power spectral density of shot noise is given by the simple relation

$$\sigma_s^2(f) = q S_{avg} \quad (2.55)$$

where q is the charge of the electron.

The current power spectral density of thermal noise is

$$\sigma_T^2(f) = \frac{2k_B T}{R_s} \quad (2.56)$$

where k_B is Boltzmann's constant, T is the absolute temperature, and R_s is the sensing resistance.

Johnson and Shot noise are the two most common sources of noise. Both processes are white, meaning they have a uniform power spectral density. The noticeable difference between them is that shot noise is signal dependent while Johnson noise is not.

In SPIFI the signal of interest is the first harmonic upper side band of the $S(f)$. From Eq. 2.10, and the scaling constants the upper sideband current is

$$\hat{S}_{i1+}(x' = f\kappa^{-1}) = \frac{1}{2} I_0 \gamma \kappa^{-1} \mathcal{W}(\kappa x') \otimes |u_1(x')|^2 \quad (2.57)$$

Leading to a current power spectral density of

$$\hat{P}_s(x' = f\kappa^{-1}) = \frac{1}{4} I_0^2 \gamma^2 \kappa^{-2} \left[\mathcal{W}(\kappa x') \otimes |u_1(x')|^2 \right]^2 \quad (2.58)$$

This scales quadratically with optical signal power. To calculate the amount of shot noise we need to find the average current coming out of the detector, which is proportional to the DC term, s_0 .

$$S_{avg} = \frac{1}{2} \gamma I_0 s_0 \quad (2.59)$$

The total signal to noise ratio can be written as

$$SNF(x' = f\kappa^{-1}) = \frac{\frac{1}{4} I_0^2 \gamma^2 \kappa^{-2} \left[\mathcal{W}(\kappa x') \otimes |u_1(x')|^2 \right]^2}{\frac{1}{2} \gamma I_0 s_0 + 2 \frac{k_B T}{R_s} + \sigma_I^2(\kappa x')} \quad (2.60)$$

Since the signal varies in frequency over the spatial extent of the beam, it is not a constant value as it would be for a time domain signal, but changes with spatial position. If the SNR is dominated by shot noise, it will increase linearly with the optical power, if it is dominated by thermal noise it will increase quadratically with the optical power. We also note, that by using a real optical modulator the average optical power on the detector is $\frac{3}{8}$ of what it would otherwise be lowering the shot noise floor by over $\frac{5}{8}$.

2.5.1 Dynamic Range of Analog to Digital Converter

The typical rule of thumb to find the dynamic range of an analog to digital converter (ATD) is the 6 dB per bit rule, which will now be derived.

As usual the signal to noise ratio (SNR) will be defined as the ratio of powers,

$$SNR = \frac{P_{sig}}{P_{noise}} = \frac{A_{sig}^2}{A_{noise}^2} \quad (2.61)$$

The signal to noise ratio in dB is

$$SNR_{\text{dB}} = 10 \log_{10} (SNR) \quad (2.62)$$

Let us suppose that we are interested in the peak SNR of a n bit signal, where only the last bit is corrupted.

$$SNR_{\text{dB}} = 10 \log_{10} \left(\frac{2^n - 1}{1} \right)^2 \quad (2.63)$$

$2^n - 1$ is the maximum value of a n bit integer, and the squaring is to convert into power. One finds

$$SNR_{\text{dB}} = 10 \log_{10} (2^n (1 - 2^{-n}))^2 \quad (2.64)$$

$$SNR_{\text{dB}} = n 20 \log_{10}(2) + 20 \log_{10}(1 - 2^{-n}) \quad (2.65)$$

the second term $20 \log_{10}(2^{-n} - 1)$ goes to zero rapidly and for $n = 5$ is $-.27$ (dB). This term can be dropped, and the SNR can be approximated by the first term

$$SNR_{\text{dB}} \approx n 6.0205 \quad (2.66)$$

or about 6 (dB) per bit. The frequency domain the SNR ratio is actually slightly better than the 6 (dB) per bit rule due to overcalling. Maximum gives the FD SNR as

$$SNR_{\text{dB}} = n 6.0205 + 1.76 + 10 \log_{10} \left(\frac{f_s}{2f_{\text{max}}} \right), \quad (2.67)$$

where f_s is the sampling rate, and f_{max} is the maximum bandwidth of the input tone [34]. The last term $10 \log_{10} \left(\frac{f_s}{2f_{\text{max}}} \right)$ is called the processing gain.

To consider if the number of bits for good SPIFI dynamic range, the 6 dB rule provides an adequate estimation, which is actually better when the processing gain is considered. For the 16 bit DAQ used to perform the experiment Ch. 4, the 6 dB rule gives a dynamic range of 96 dB.

2.6 Symmetrical vs. Asymmetrical Modulation

The SPIFI pattern as proposed in Sec. 3 sweeps the spatial frequencies over the range $\pm \frac{\Delta k}{2}$ during each rotation of the modulator, with each spatial frequency modulated twice. The information appears redundant, if a time delay of $\frac{.5}{T_m}$ is introduced to the modulator, then over its acquisition period the time domain signal of Eq. 2.4 would capture the 0 to Δk spatial frequencies of intensity spatial frequency distribution $\mathcal{G}'(f_x)$. Since $|u(x')g(x')|^2$ must be real, $\mathcal{G}'(f_x)$, must be conjugate symmetric, meaning $\mathcal{G}'(-f_x) = \mathcal{G}'(f_x)^*$.

The half time domain $s_{\text{half}}(t)$ trace with spatial frequencies ranging from 0 to Δk can be collected, and added to a flip time domain conjugate of it's self to produce a double sided time domain signal that can be transformed by the computer to yield Eq. 2.50.

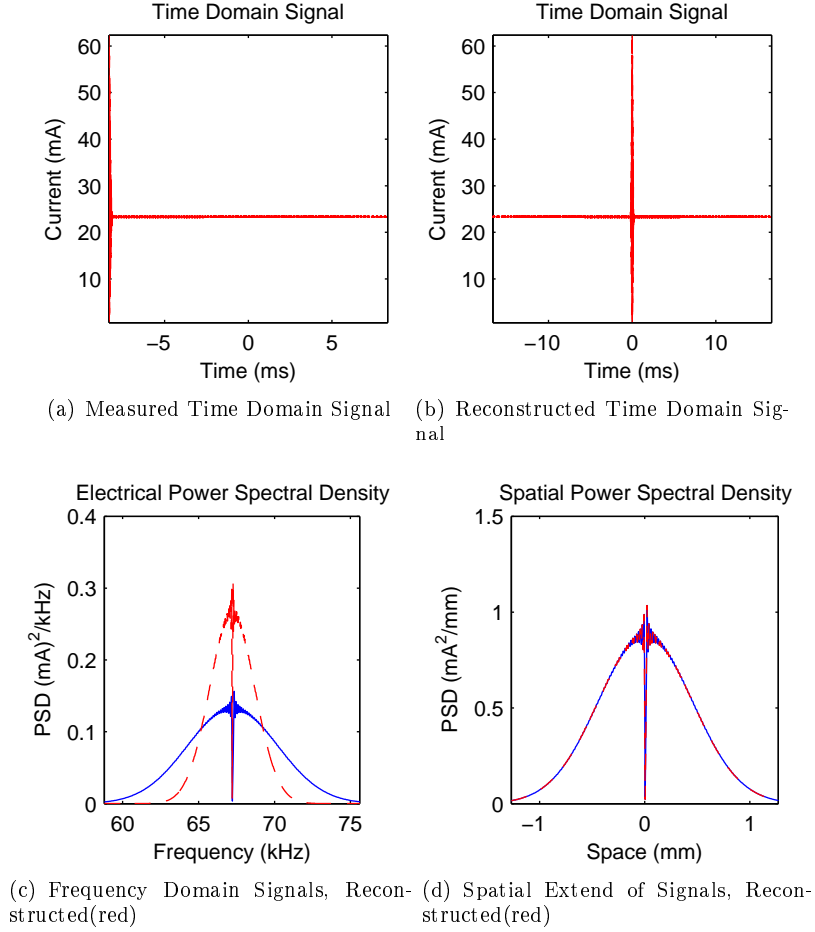


Figure 2.3: Measured Time Domain Signal (a) and Reconstructed Time Domain Signal (b) compared against non reconstructed signal (blue) in measured electrical power spectral density (c) and in spatial electrical power spectral density (d)

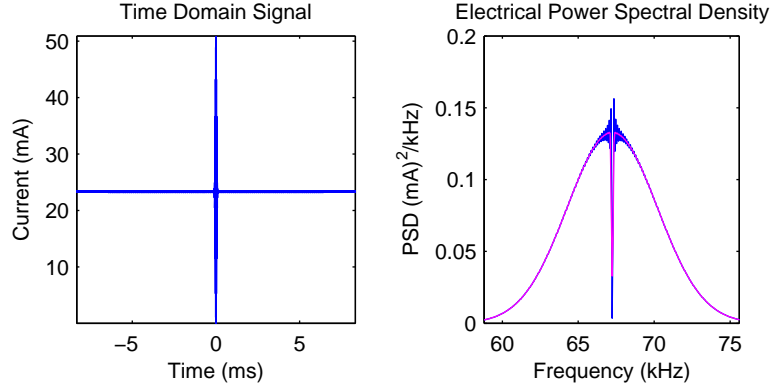
The new trace will have a time duration of $2T_m$ and thus a resolution bandwidth of half that and thus spatial resolution of twice that of the original trace. The other difference is that using the time offset has a maximum spatial frequency in the trace of Δk vs $\frac{\Delta k}{2}$ in the first instance. The value of Δk should thus be lowered by a factor of 2 to have the same maximum spatial frequency for comparison thus resulting in a equal resolution trace.

Verification that there is no difference between the methods was done numerically. Working with the parameters of Table 3, and setting $M_1 = -0.25$, $M_2 = -1$ the single sided trace for the same field spatial distribution was generated, as shown in Fig. 2.3 (a) without propagation. This trace was added to a flipped and rotated version of itself generating and the trace of Fig. 2.3 (b). The trace was then transformed to the frequency domain, shown in Fig. 2.3 (c) and plotted with the that generated by the typical symmetric TD trace.

It appears that both frequency domain traces occupy the same area, under inspection of Parseval's Relation, it was found that the time domain traces generated with both methods have the same average power. When the traces are mapped to the spatial domain shown in Fig. 2.3 (d), one sees that they overlap nearly perfectly, thus verifying that the method of flipping, has no substantial effect on the spatial content of the traces.

The only difference between the two traces when plotted in spatial coordinates, is that the flipped method occupies twice the space and the unfilled method. This is due to the points being at the same spacing, but the flipped trace having twice the points. We decided not to use the method of flipping, as it would complicate the processing during real time acquisition.

2.7 Analysis of the time window



(a) Time domain Signal From Detector
(b) Comparison of Hamming Window (magenta) with square window (blue)

Figure 2.4: Electronic time domain signal (a), and electronic frequency domain signal (b)

All recorded traces have an implicit rectangular time window, $w(t) = \text{rect}\left(\frac{t}{T_m}\right)$. The implicit rectangular time window, $|w(t)|^2$ causes the object to be convolved with a *sinc* in the FD, causing edge ripple as shown in blue in Fig. 2.4 (b). Here we demonstrate that the ripple can be eliminated by applying alternate window functions, in this case a hamming window, to the time domain trace.

A TD and FD traces of the simulation without diffraction is shown in Fig. 2.4. These simulations had resolution limited notch object of the type shown in Fig. C.1. In the purple trace in Fig. 4(b) (b), a Hamming window was applied to the TD trace before transforming, this is shown compared against the implicit rectangular window with FD trace shown in blue. Using the Hamming window suppressed the edge ripple previously present with rectangularly windowed TD trace. The cost of using the Hamming window is a slightly broader FD function is convolved with the image. This seems to be a reasonable trade off since the ripple caused by the rectangular window can make the

image very difficult to interpret.

CHAPTER III

THE DISC MODULATOR

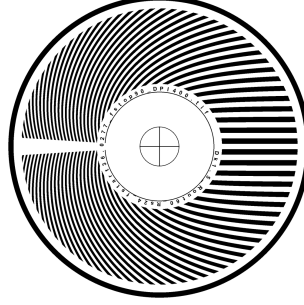


Figure 3.1: Example Mask with $\Delta k = 1.5 \text{ (mm)}^{-1}$, $k_0 = 0$, and $\Delta\theta = .98(2\pi) \text{ (rad)}$

The modulation function $m(x, t)$ of Eq. (2.2) can be realized by printing a pattern of absorbing features onto a transparent disc. Slicing the incident beam with the disc then spinning it will create a beam with the desired modulation. The beam to be modulated is focused to a radial line focus, so that the amplitude modulation frequency depends linearly on radial position R . We have created masks with the family of patterns defined by

$$m(R, \theta) = \frac{1}{2} + \frac{1}{2} \cos [(k_0 + \Delta k R)\theta] \quad (3.1)$$

where θ is the angular coordinate relative to the center of the disc. An example print of this pattern is shown in Fig. 3.1. The prints of the mask had $m(R, \theta)$ rounded to either 0 or 1 to avoid dithering of the print, making the printed mask

$$m(R, \theta) = \frac{1}{2} + \frac{1}{2} \text{sgn}(\cos [(k_0 + \Delta k R)\theta]) \quad (3.2)$$

, where *

$$\text{sgn}(x) = \begin{cases} 1 & \text{if } x \geq 0 \\ -1 & \text{if } x < 0 \end{cases} \quad (3.3)$$

The simulated effect of the rounding is treated in Sec. C.2, it has the effect of dampening the second harmonic signal. In this section we will approximate the modulator as Eq. 3.1.

The radial line is sampled at an angle $\theta_0 = 0$. To get time modulation, the mask is spun around its origin at a constant angular velocity, $2\pi f_0$, causing a constant angular displacement of

$m(R, -2\pi f_m t)$. This leads to a radially, time dependent equation at $\theta_0 = 0$.

$$m(R, t) = \frac{1}{2} + \frac{1}{2} \cos [2\pi f_m (k_0 + \Delta k R)t] \quad (3.4)$$

Substituting R with x, Eq. (2.2) and Eq. (3.4) are of the same form. Comparing the terms, the center frequency, f_c is $f_m k_0$, the chirp parameter $\kappa = f_m \Delta k$. In the lab, the beam and the modulator will not be centered on the same coordinate axis. The coordinate systems are displaced spatially by x_0 . This changes the center frequency to

$$f_c = f_m k_0 + f_m \Delta k x_0 \quad (3.5)$$

3.1 Number of Points and Resolution

In Sec. 2.4 the performance quality of the SPIFI image was evaluated in terms of their key parameters of resolution and field of view leading to the total number of points resolvable in a SPIFI trace. It was found that the SPIFI resolution was inversely proportional to the highest spatial frequency produced by the modulator, $\frac{\delta x}{2} = f_{x_{\max}} = \frac{1}{2} \kappa T_m$. Though, the famous relation, $\delta x = \lambda(2NA)^{-1}$ this the modulator can be associated with a NA .

For the disc modulator, $\kappa = f_m \Delta k$, and $T_m = (f_m)^{-1}$. The maximum spatial frequency produced by the modulator, $f_{x_{\max}} = \frac{\Delta k \Delta \theta}{2}$ is just a function of the mask print parameters Δk , $\Delta \theta$. The NA is then just a product of the highest spatial frequency of the disc modulator with the wavelength,

$$NA = \frac{\lambda \Delta k \Delta \theta}{2} \quad (3.6)$$

where n is the index of refraction of the medium, taken to be air $n = 1$.

The number of resolved points, N , is given by the illumination field width, W , divided by the spatial resolution, δx . Making the substitution,

$$N = W(\delta x)^{-1} = W \Delta k \Delta \theta \quad (3.7)$$

which is just a function of the spatial extent of the beam and the print parameters of the mask, and is the same as $N = \frac{W n k_{x_{\max}}}{\pi}$.

For the temporal signal, the number of points is the modulation bandwidth, Δf_m , divided by the resolution bandwidth, δf . The resolution bandwidth is the inverse of the acquisition duration, T_m , leading to the time bandwidth product, $N = \Delta f_m T_m$. For the SPIFI disc modulator, the signal bandwidth is $\Delta f_m = f_m \Delta k W$, and the resolution bandwidth is $f_m (\Delta \theta)^{-1}$ leading giving a temporal number of points, $W \Delta k \Delta \theta$, identical to the spatial number of points.

3.2 Wobble

A high number of points in SPIFI requires a high value of Δk leading to dense features on the disc. For a $\Delta k = 100(\frac{1}{mm})$, the structure of the disc would have feature size of 10 (mu). It is reasonable to expect that if the disc wobbles an amount greater than the feature size 10 (mu) per revolution then the spatial resolution of the points will blur together in the FD.

A simple deterministic model for the frequency blurring attributes it solely due to nonconcentric mounting between the modulating disc and the motor. The nonconcentric mounting can be viewed as a coordinate shift to the modulator, Eq. 3.1 as shown in Fig. 3.2. The offset is represented by \vec{x} in Fig. 3.2.

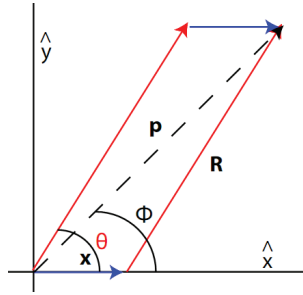


Figure 3.2: Coordinate Shift Diagram

\vec{x} is added to \vec{R} and the new vector \vec{p} represents the shifted coordinate system. The disc now rotates around the new origin. Points in this system can be written in polar coordinates as (ρ, ϕ) . The new values for R and Θ are

$$R^2 = x^2 + y^2 + \rho^2 - 2\rho(x\cos(\phi) + y\sin(\phi)) \quad (3.8)$$

$$\Theta = \tan^{-1}\left(\frac{\rho\sin\phi - y}{\rho\cos\phi - x}\right) \quad (3.9)$$

Substituting this into the modulator equation, 3.1, one finds the mask function in the new coordinate system to be

$$t_{mod}(\rho, \phi) = .5 + .5\cos\left((k_1 + \Delta k\sqrt{x^2 + y^2 + \rho^2 - 2x\rho\cos(\phi) - 2y\rho\sin(\phi)}\right)\tan^{-1}\left(\frac{\rho\sin\phi - y}{\rho\cos\phi - x}\right)\right) \quad (3.10)$$

To get the time modulation function ϕ should be substituted for $2\pi f_0 t$, leading to the messy expression

$$t_{mod}(\rho, \phi) = .5 + .5\cos\left((k_1 + \Delta k\sqrt{x^2 + y^2 + \rho^2 - 2x\rho\cos(2\pi f_0 t) - 2y\rho\sin(2\pi f_0 t)}\right)\tan^{-1}\left(\frac{\rho\sin(2\pi f_0 t) - y}{\rho\cos(2\pi f_0 t) - x}\right)\right) \dots \quad (3.11)$$

Since the distance from the origin is ρ typically larger than the offset of the disc placement, the square root term inside the first cosine is dominant in the expression. The x^2 and y^2 terms are off

little concern because they remain constant in time. The cross terms between $2x\rho$ and $2y\rho$ are not constant in time and modulate the argument of the first cosine.

The effect of the wobble will further analyzed numerically in Sec. 3.3. It will also be measured in Sec. 4.1.

3.3 Wobble Correction

A model of FD trace distortion to non-concentric disc mounting leading that we refer to as wobble was presented in Sec. 3.2. In this section we simulate the disc wobble and present a method that to remove it.

Two traces, one concentricity mounted and one with a non-concentric mounting of $100(\mu m)$ are shown in Fig. (b). The spital extent of the illumination beam with the object for both traces, back propagated to the object plane is shown on in Fig. 3.3 (a).

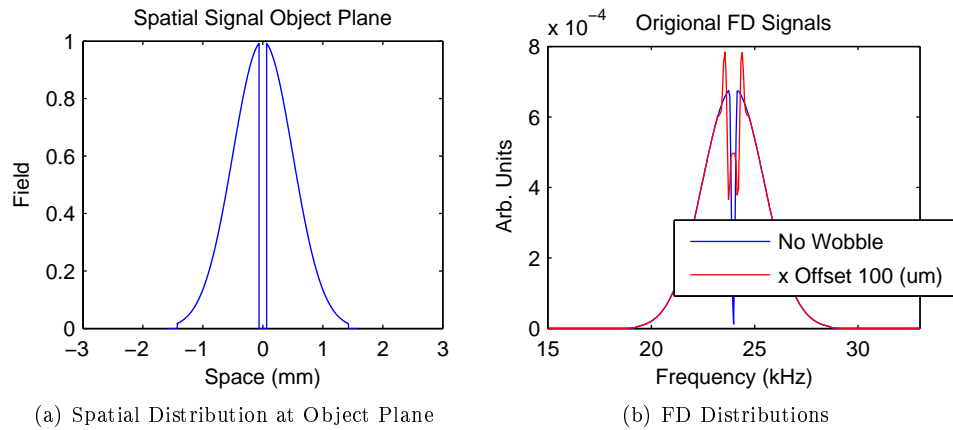


Figure 3.3: Spatial Distribution (a) and FD Distribution (b)

The from the simulation parameters, resolution of this trace is $\frac{1}{\Delta k} = 20(\mu m)$. For just twice the resolution limit in disc offset the trace becomes distorted, and with increasing offset like 5 times the resolution used in Fig. 3.3 (b) the distortions become worse. Ripple appears on the sharp edges in the trace.

Another way to understand the frequency distortion due to the wobble is to look at the wobbles' effect on a point object at the or past the SPIFI resolution limit. Ideally such a point would appear as a single point in the FD. Under wobble, the single function will blur out. This effect is shown in Fig. 3.4.

At least for deterministic distortions, such as those of Sec. 3.2, the wobble may be thought as time varying change of the center frequency of a focused signal. This focused signal, like that shown

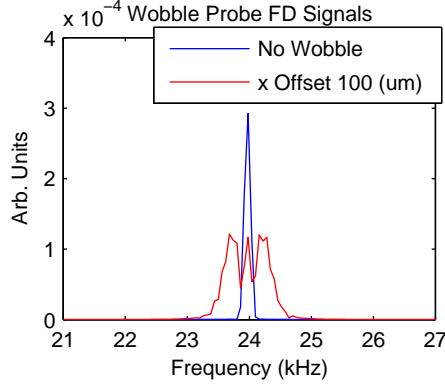


Figure 3.4: Wobble Probe Traces without offset and with x offset of 100(μm)

in Fig. 3.4 will be referred to as the wobble probe. To assess if this is the case, the Gabor transform of the time domain trace with the wobble signal was taken.

$$G_x(t, f) = \int_{-\infty}^{\infty} x(\tau) e^{\left(\frac{t\alpha u - t}{w_g}\right)^2} e^{-j2\pi f\tau} d\tau \quad (3.12)$$

The Gabor transform is one of many transforms that can produce a 2D phase space distribution between time and space. The width of the gaussian, w_g in Eq. 3.12, effects the localization between frequency and time in the distribution. The Gabor transform for the signal corresponding to the wobble trace of Fig. 3.12 is shown in Fig. 3.5. The width of the Gabor time domain gaussian was taken to be $w_g = 1.7$ (ms).

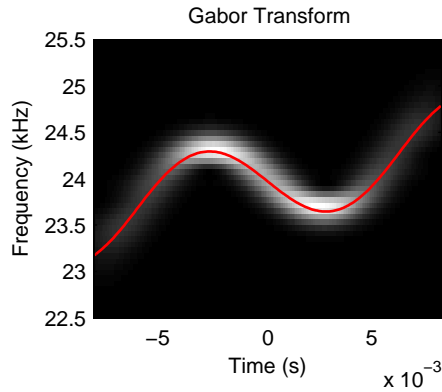


Figure 3.5: Gabor Transform of Probe Wobble Trace

An approach to compensate for the wobble is to rescale the time axis such that the wobble probe stays at a constant frequency becoming a singular point again. We wish to rescale the time axis such that as the Gabor transform centroid drifts towards higher frequencies have time domain points that are stretched to be farther apart, and when the centroid drifts towards lower frequencies the time

domain points are changed to be closer together. The time separation between the points dt will be linearly scaled.

The amount to scale dt depends on the ratio between centroid as shown in red in Fig. 3.5, and the centroid's center frequency, taken to be the time average of the centroid frequency. Thus dt will be multiplied by the compensation factor such that

$$dt'[t] = dt * \frac{f_{centroid}[t]}{f_{center}} \quad (3.13)$$

The new time points spacings are then cumulatively summed to make a new time axis.

$$t_{new}[t] = \sum dt'[t] \quad (3.14)$$

This axis still has the same number of points as the original trace but the time points are no longer evenly spaced. Since the time points need to be evenly spaced to do the FFT, the new points are interpolated from the original data set.

Performing this on the wobble trace of Fig. 3.4 produces a new wobble trace shown for comparison with the original in Fig. 3.6. The focused trace looks narrower than the original measurement.

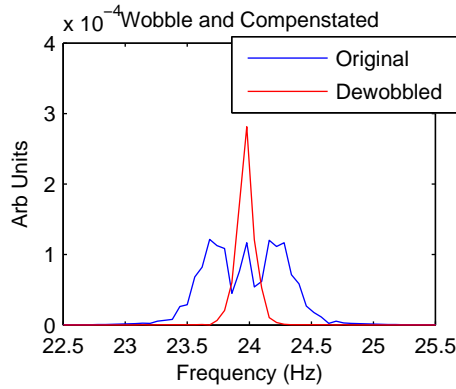


Figure 3.6: Comparison of Original and Correct Probe Traces in the FD

The new time axis is then applied to the signal trace and interpolated to generate a compensated signal. The original trace and the new trace are compared in Fig. 3.7.

The compensated signal trace looks close to the original shown in Fig. 3.3 (a).

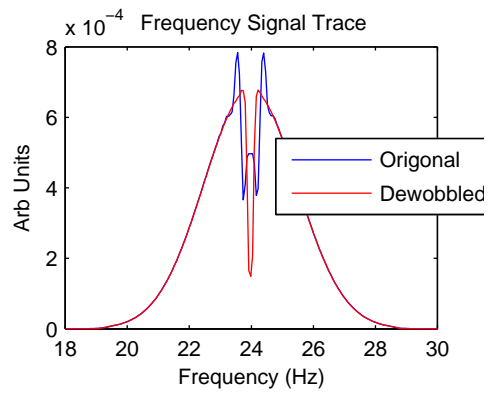


Figure 3.7: Comparison of Original and Correct Signal Traces in the FD

CHAPTER IV

EXPERIMENTAL

A diagram of the constructed system used to perform the SPIFI imaging is shown in shown in Fig. 4.1. The system was based on a fiber-coupled continuous wave(CW) laser with center wavelength 1550 nm that was set at 20 % power to produce output 20 (mW) at the output of a fiber collimator. A 25 mm lens was used to make the beam converge to tight waist, which was measured with a gaussian fitting beam profiler(Bullet) to have a waist of $w_y = 11.23$ (μm) in the plane perpendicular to the table and a waist of $w_x = 10.91$ in the plane of the table. The fit profiler produced M squared(M^2) measurements for these waists of $M_x^2 = 1.04$ and $M_y^2 = 1.03$.

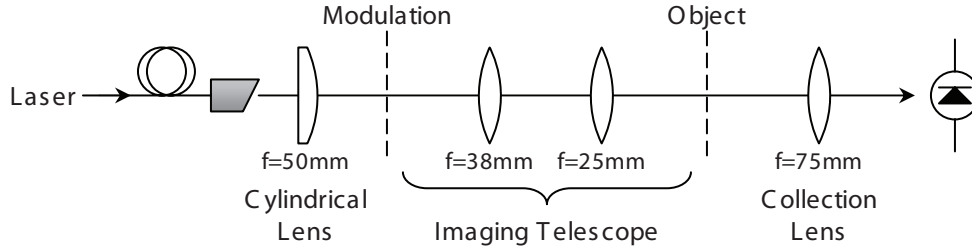


Figure 4.1: Optical System

Since the M^2 values for the waists are very close to one, the illumination beam path can be designed using the complex beam propagator, q . LaserCanvas 5, developed by P. Schlup, is a program that allows for the design of optical beam paths by allowing the 2D movement optical elements. LaserCanvas uses the q propagator to show the spatial extent of the beam.

The optical beam path first transforms the circular beam into a line focus, which illuminates the modulator, which is then followed by two imaging systems. The imaging systems were used to relay the field between modulation, object, and detector planes.

The first line was created by collimating the beam with a $f = 62$ (mm) lens and then focusing the collimated beam in the y -axis with a $f = 50$ (mm) cylindrical lens. The line focus was used to illuminate the modulator at the modulation plane. At the modulation plane the line focus had a measured waist in the y -axis of $w_{y \text{ mod}} = 12.65$ (μm), and M_y^2 parameter of 1.42. The beam size in the x direction was measured to be $w_{x \text{ mod}} = 2.92$ (mm) and not convergent enough to measure its specific location nor the M_x^2 value.

The modulation plane was then imaged with a demagnifying $M = -.80$, $f_1 = 62$ (mm), $f_2 = 50$ (mm) telescope to the object plane. The object under examination was placed in the modulated illumination beam at the object plane. At the object plane the illuminating line focus was measured to have a focus of $wy \text{ mod} = 12.65$ (um) and $M_y^2 = 2.51$ and a beam width of $w_x = 1.92$ (mm).

The field of the illuminating line focus perturbed by the object was collected with a $f = 75$ (mm) lens configured to demagnify by -1.36 times onto the area of a 10 (mm) area of a Ge photodiode(ThorLabs DET50B).

TIFF files of the mask pattern were generated with a Matlab code. The mask file used in the experiment is shown in Fig. 4.2. The transparent stripe at the $\pm\pi$ boundary was used for timing. The files were printed by courtesy of MAM-A with a 400DPI thermal printer onto a clear polycarbonate CD-ROM substrate stamped out by U-TECH Dallas. The mask file was generated with parameters, $k_1 = 0$ and $\Delta k = \frac{7}{mm}$. The value of Δk was limited by the DPI of the thermal printer. A chuck was made to mount the mask to a 1628 brushless DC Faulhaber motor with a maximum angular speed of 477 rotations per second. The motor was spun at the slower rate of $f_0 = 40(Hz)$ to lower the burden on the data acquisition computer. The companioning Faulhaber SC1801 speed controller provided a timing signal corresponding to the motor period used to synchronize the data acquisition.

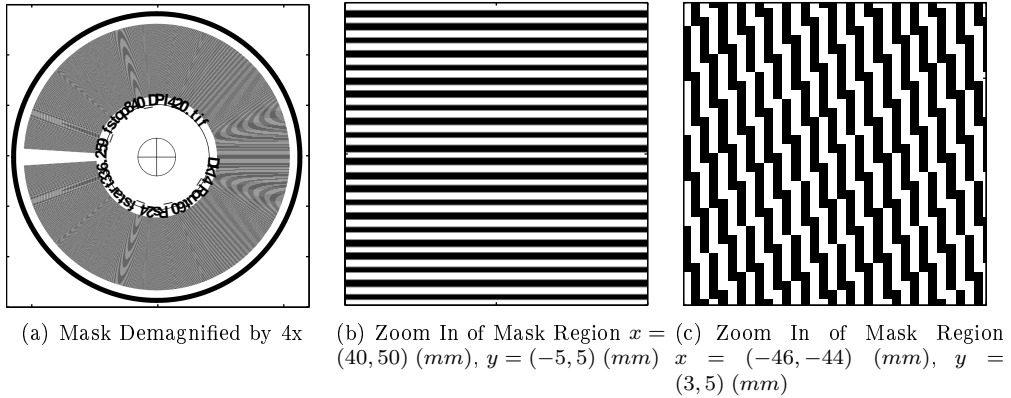


Figure 4.2: The mask file used for the data with parameters $\Delta k = 14$ ($\frac{1}{mm}$) and $k_0 = 0$, demagnified (a) and zoomed to the area of low frequencies (b) and zoomed to an area of high frequencies (c).

The output current from the Ge detector was transimpedance amplified at $1 \frac{mA}{V}$ and was sampled at 80 (kHz) with a NI-6251 DAQ using in-house software(Squid). The in house software transformed the time domain traces and displaced their frequency domain power spectral density in real time for use in the lab. The software provided ease in synchronizing line(frame) window and outputted the data to a MATLAB .mat file for postprocessing. A time domain trace for the unperturbed beam

is shown in Fig. 4.3 (a). The time domain trace is a Gaussian modulated by the carrier frequency. The in the FD the beam the Gaussian is shown in units of PSD in Fig. 4.3 (b) blue, and the fitted trace for the beam profiled waist is in the red dashed line. The theoretical profile is similar to what is measured.

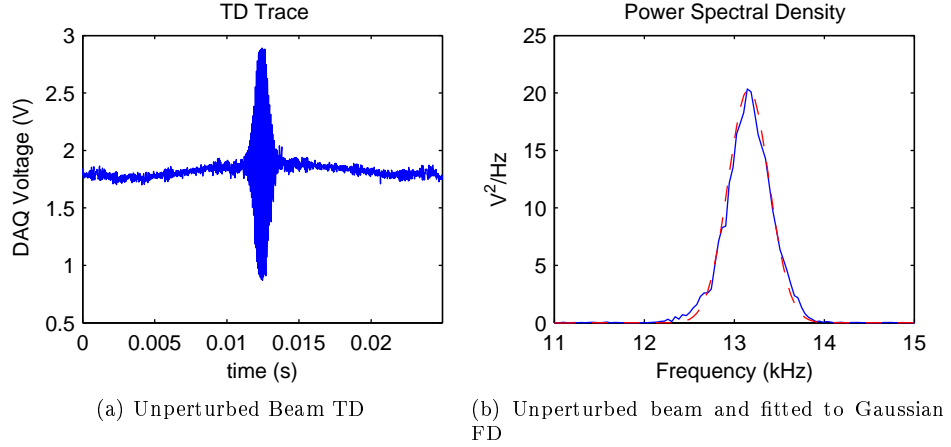


Figure 4.3: The unperturbed gaussian beam in time (a) and frequency (b) (blue) fitted to measured gaussian (red)

The center frequency of the trace is at 13.2 (kHz). From theory of Sec. 2.1, and for the mask parameters and system magnifications, the beam is determined to be centered 47 (mm) from the center of the disc. The profiled Gaussian had waist parameter $w_{0y} = 2.92(mm)$, maps to 1.29 kHz of bandwidth in the SPIFI FD, this gaussian profile is shown overlaid on the data in Fig. 4.3. Since the PSD is the 2nd power of the measured intensity, the plot is the 4th power of the field. (b). The expected resolution at the object plane is, 5.32 points/mm.

To further demonstrate the SPIFI theory, an spatial image was taken. A 1954 air force test pattern was placed in the object plane, and translated in the y-axis to resolve the other necessary axis. The 2D image is shown in Fig. 4.4, to demonstrate ability of SPIFI. It is noted that there is little ripple from the sharp edges in the mask, and that the numbers are also resolvable. Other higher speed methods to resolve the y dimension such a galvos or AOBD could also be used. Row 6 in the test pattern appears at the pixel limit. The period of lines in row 6 is 280 μm apart. The vertical lines appear to span 2 pixels.

4.1 Wobble Correction

A HeNe laser, $\lambda = 632.8 (nm)$, was added to the system as a probe beam. Its beam was focused to a measured waist of $w_0 = 10(\mu m)$ in the modulator plane. This waist is smaller than the resolution

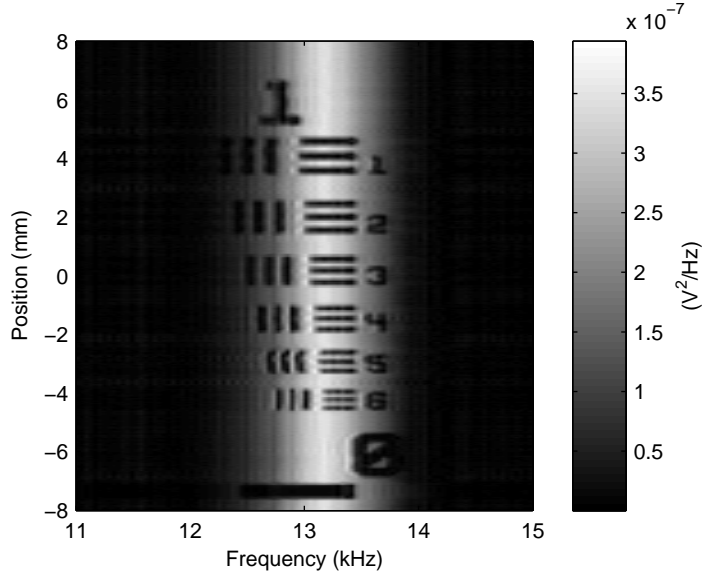


Figure 4.4: Image of 1954 Air Force Test Pattern

of the system, and this point should be the width of the Fourier Transform of the time window centered at the frequency determined by the centroid of the point on the wheel. The FD signal as the probe trace as shown in Fig. 3.6.

The probe beam was collected after the measurement focus with a $f = 25(mm)$ lens onto a single element diode(ThorLabs DET10A). This trace was acquired simultaneously with each FD SPIFI trace, sampled at the same sampling frequency $f_s = 80 (kHz)$.

The 400 SPIFI traces used to generate the Air Force test pattern of Fig. 4.4 were acquired simultaneously with the wobble probe beam. Producing 2 400 sets of traces. To look at the statistics of the wobble probe measurement. First a representative trace, the first trace taken in the probe Fig. 4.5 (a), and it's Gabor transform, Fig. 4.5 (b), with Gabor gaussian $w_g = 5 (ms)$ is shown to the reader for reference.

The Fourier transform of 400 Wobble traces are shown super imposed in and the centroid of the Gabor transform for each trace is shown in Fig. 4.6. This is to give the reader an appreciation of the high frequency noise.

To understand the repeatability of the wobble traces between shots, the average frequency and the standard deviation of the gabor transform as a function of frequency were taken. The standard deviation is plotted around the mean values in Fig. 4.7

At the beginning and end of the traces the standard deviation increases due to the centroid not being well localized.

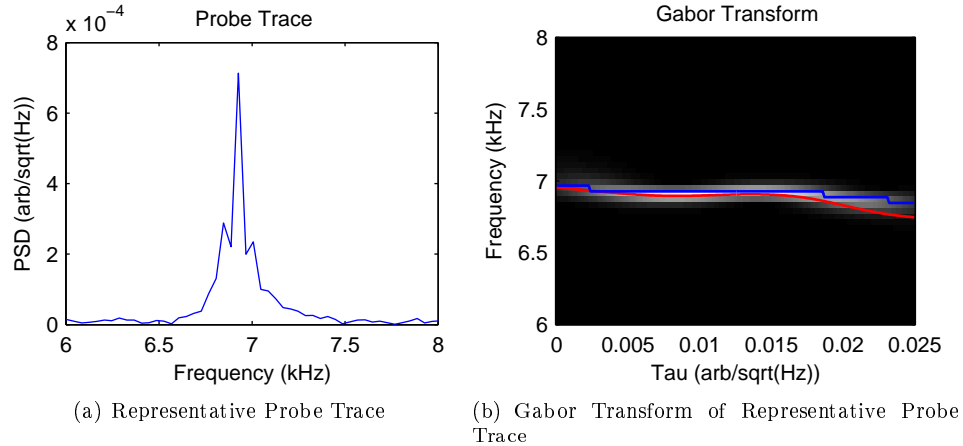


Figure 4.5: A representative probe trace (a) and in phase space (b)

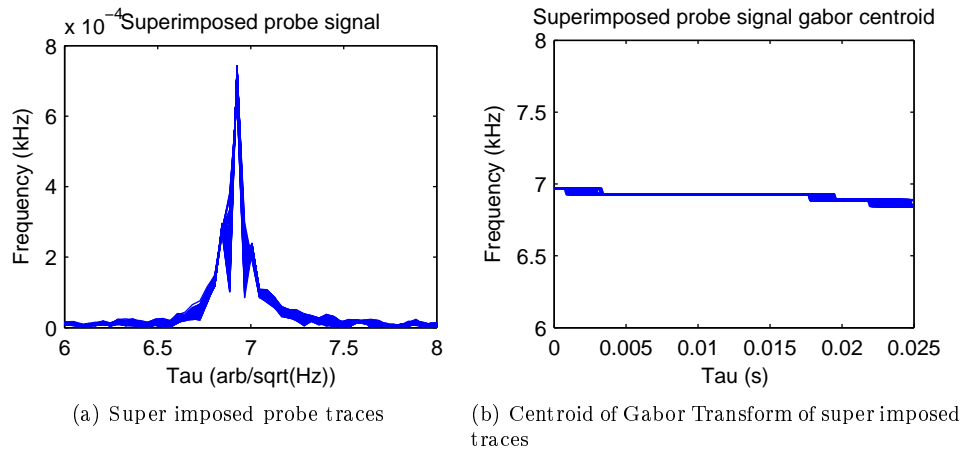


Figure 4.6: Probe traces superimposed (a) and in phase space ??

The simplest method is to generate the correction from just one of the probe signals and apply this to all of the image traces. Since the probe trace is being acquired simultaneously with the image traces, the probe trace corresponding to a given image trace can be used to generate the correction factors for each of the signal traces. Finally, the centroids of the gabor transform are shown in Fig. 4.7 (b). This can also be used to generate the correction factor and can then be applied to all of the traces, similar to the first case.

If the correction is working well it should narrow the probe trace. Applying these corrections to all of the probe traces, an additional mean and standard deviation can be found. The mean and standard deviation for the three methods in correction to the probe traces are shown in Fig. 4.8.

From the correction to the probe traces, Fig. 4.8, one sees that correcting using just one measured correction value produces a sufficient result, and it is probably unnecessary to correct in real time

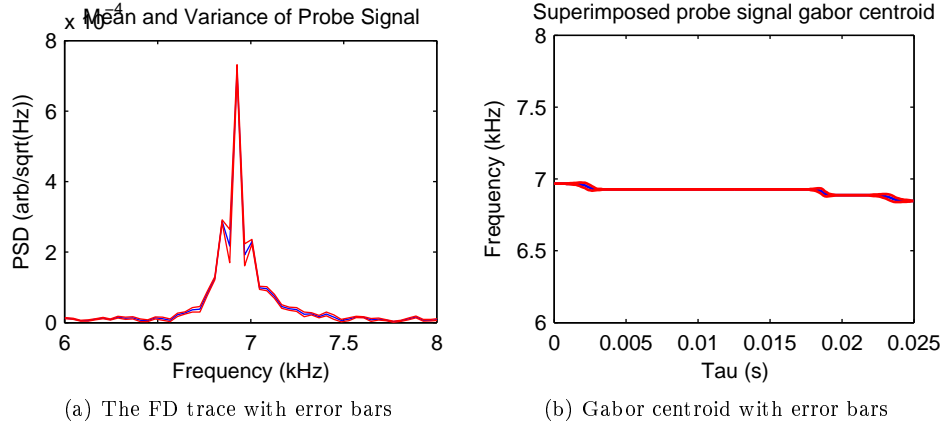


Figure 4.7: Probe traces with error bars (a) and in phase space (b)

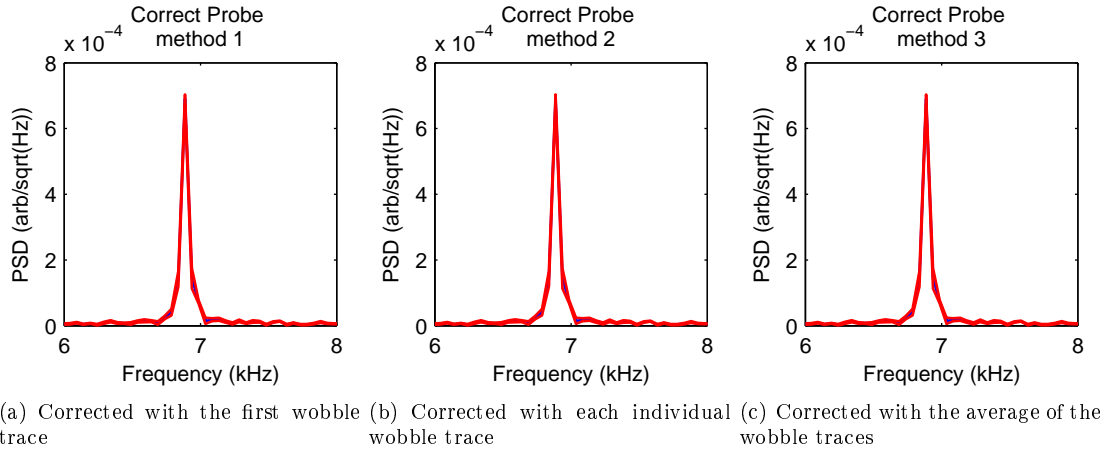


Figure 4.8: Comparison of corrected probe traces using different methods, using the first probe trace (a), using the corresponding probe trace (b), and using the centroid of the probe traces (c). The uncorrected trace

to each of the probe traces simplifying the acquisition.

The correction to the Air Force test pattern using all three methods discussed is shown in Fig. 4.9, in comparison with when no correction is applied.

The wobble correction algorithm appears to have little effect on the airforce test pattern image. This is probably due to the mount concentricity after much improvements in centering through interaction being near 142 (μm) the point at which the concentricity becomes a problem for the $\Delta k = 7$ (mm) wheel. The power axis between the traces shows that the wobble corrected trace has slightly less dynamic range than the original. The loss of dynamic range may be an effect from the interpolation where the cosine becomes rounded off.

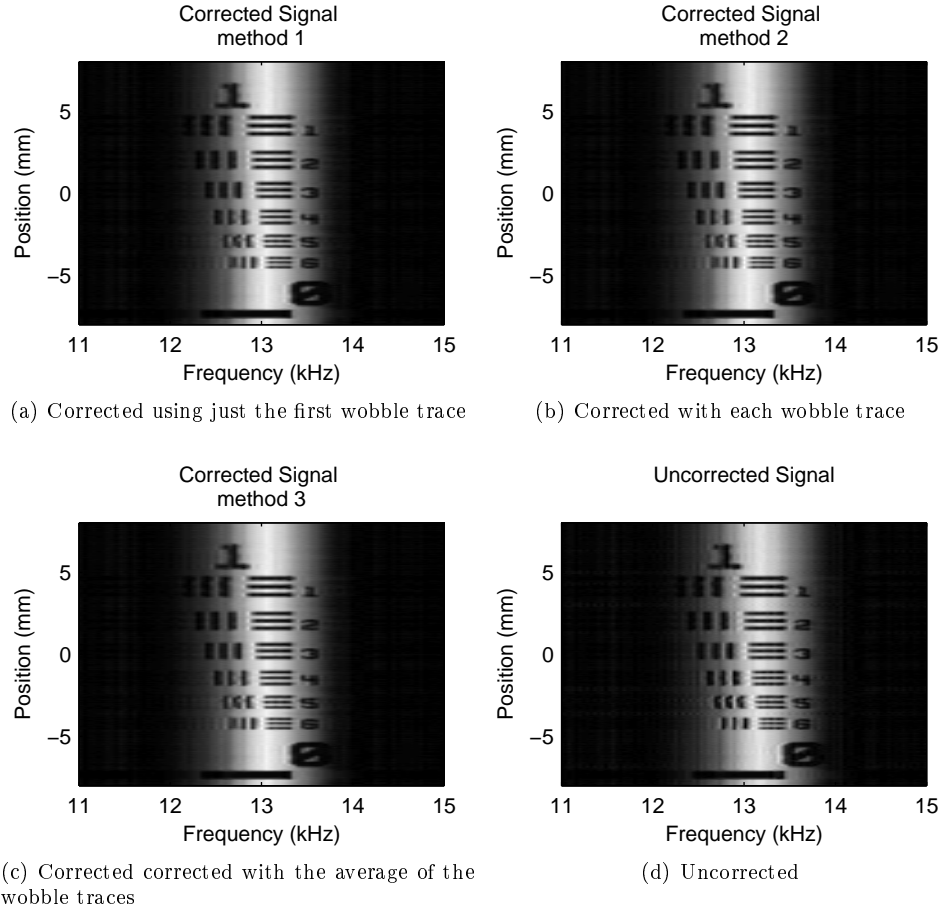


Figure 4.9: Comparison of corrected Air Force test patterns traces using the three methods, using the first probe trace (a), using the corresponding probe trace (b), and using the centroid of the probe traces (c). The uncorrected trace for comparison Fig. (d).

4.2 *Fluorescent Imaging*

The illumination source was changed $\lambda = 532(nm)$ laser(Coherent DPSS 532) to demonstrate SPIFI modulation transfer to florescent emission.

The SPIFI modulator illumination and optical imaging system transferring it to the object has remained the same. For the fluorescent images the SPIFI modulated florescence was then imaged though two optical filters and a grating to reject the pump beam, leaving just the field of florescent spectrum. The filters were removed and the grating was rotated to pass the fundamental to capture the absorption images.

A fluorescent object was created consisting of a glass slide with a image imprinted on it with florescent ink. The slide was prepared by dry coating hairspray onto its surface. The felt tip of a orange highlighter(Sharpie) was rubbed onto the surface of a rubber stamp, coating its surface with

ink. The stamp was then pressed onto the surface of the slides transferring the pattern to the slide.

Images of the fluorescent dye pattern, taken in both absorption (a) and emission (b) configuration is shown in Fig. 4.10. The images have been normalized relative to the leak through excitation or illumination intensity measured in the absence of a sample. Inhomogeneity of the dyes application to the slide caused blotchiness of the tips the edges of the star. Each image is the composite of 3 2D SPIFI image segments, with a manual translation stage used to offset the image relative to the line focus for each scan.

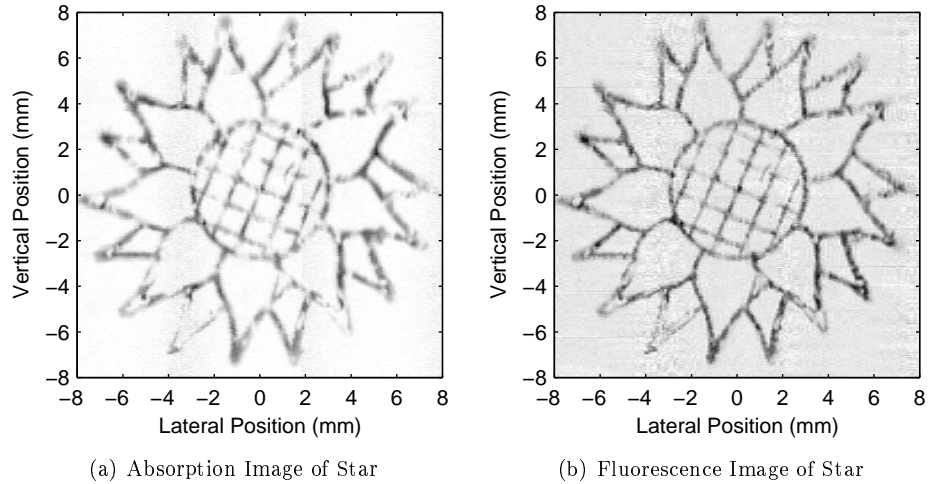


Figure 4.10: Absorption image of star stamp Fig. (a), Fluorescence Image of Star Fig. (b)

The images captured by the large area diode(ThorLabs DET10A) were amplified using a transimpedance amplifier with a gain of $1 \frac{mA}{V}$ for the fluorescence images and $1 \frac{V}{mA}$ for the absorption images. A bandpass filter on the amplifier was engaged with -6 (dB) corner frequencies of 3 kHz and 100 kHz. The voltage signal was collected with a DAQ using custom in-house software(Squid).

Although the motor was not able to spin at acquisition speed of SPIFI could be raised to 500 lines per second, potentially enabling acquisition of a 500x500 point image 1 second. Ways to push SPIFI to higher speeds will be proposed in this section. These methods can be generally grouped into two categories. Methods to multiplex more information into the bandwidth of the detector and methods increase the number of detectors elements.

CHAPTER V

CONCLUSION

Theory and experimental results for a 1D single detector image acquisition method called SPIFI have been presented. Many modulator formats are possible. In this work a opto-mechanical modulator was implemented. With this modulator the update rate of the SPIFI 1D line images is the rotation speed of the modulating disc(Ch. 3). Using this technique, an absorption image of a Air Force test pattern was collected with resolution of 120 (μm). The modulation is slow enough to be transferred from a illumination beam to florescent emission, and images of a florescent pattern were acquired.

SPIFI offers the ability to do high resolution wide field imaging leading to a high number of points. For example consider visible wavelength radiation, with a $\lambda = 700$ (nm), assuming a optical system $\text{NA} = .5$, and the pattern covers the full angular distribution of the disk, $\Delta\theta = 1$ the maximum value of Δk that can be reproduced on the detector is $\Delta k = \frac{2\text{NA}}{\lambda\Delta\theta} = 1,428$ ($\frac{1}{\text{mm}}$)(Eq. 3.6). If a modulator was filled with 10(mm) of a field of interest then imaged under unity magnification none of the field of view would be lost on the area of a 10 (mm) x 10 (mm) such as a ThorLabs DET100A [35]. The detector would then collect 14,285 points per line scan, at a resolution of $\delta x = 700$ (nm). Currently available digital cameras use array detectors that support up to 10 megapixels. In one dimension, this is 3,464 points so SPIFI images with 14,285 points per frame is a interesting proposition due to the large field of view. Critics may still point to array detectors as being able to produce 2D wide-field images quicker, and arguing against the additional complication to the imaging system to do SPIFI when a sensitive or fast 2D array detector could be purchased.

In the even redder wavelengths bands such as the mid-infrared, far-infrared, terahertz(THz), and millimeter wave regimes array detectors are costly, with limited commercially availability(mid-infrared, far-infrared), if any at all(terahertz, millimeter). In particular the THz region remains one of the least tapped of the electromagnetic spectrum even though there is perhaps nowhere else in the spectrum with so much information about chemical species [36]. It is in these spectral regions that wide-field optical multiplexing methods such as SPIFI may have a big impact.

Currently, optical multiplexing in the terahertz region mostly consists of raster scanning. If a laser beam can be employed to scan across the target, raster scanning can be a viable option as was done in [37]. If passive wide-field imaging is desired, the $\frac{1}{N}$, where N is the number of points

collected, loss in signal makes raster scanning unattractive. Compressed sensing may offer an answer, but even these methods used in the terahertz have yet to produce impressive results [38].

In the THz constructing a line camera with SPIFI mask such as [25] may be a good answer. SPIFI is ultimately limited in resolution by the maximum periodicity that can be reproduced between the mask and detector planes(B). If 3 THz, is the optical frequency of interest. This would correspond to a wavelength of 100 (μm). Again assuming the optical NA = .5, the maximum value of $\Delta k = 10$. An a image resolution of $\delta x = 100$ (μm). The experiment is made interesting by generating a high number of points in the electronic signal. This requires a large field of view and 1D detector with large area. If the field of view was made $W = 50$ (mm) and imaged onto a rectangular detector, this would correspond to $N = 500$ points per 1D line scan allowing for discernable images. Many detectors exist in the THz [36], one rectangular detector that would suit the needs of area and response time is a large area bolometer [39].

Regardless of the wavelength band of interest, there two issues should be addressed in order to capture SPIFI images with a high number of points as proposed. These are the increasing the periodicity of the optical mask Δk , and removing aberrations from the optical systems such that Δk is reproduced on the detector's area. These two issues are addressed in the future work section(Sec. 5.1.1, 5.1.2). Then in Sec. 5.1.3 non-optimal use of the detectors's electrical bandwidth and spatial area is considered and is used to lead into the question of 2D modulation methods. Finally, the Sec. 5.1.5 considers the possibility of SPIFI imaging with high frame rate and high number of points used a 1D array detector.

5.1 *Future work*

5.1.1 Improvements to the disk modulator

In this work, the experimental disc modulator used had a $\Delta k = 7 \frac{1}{(mm)}$. This modulator was produced by printing the mask with a thermal printer onto a clear polycarbonate CD-ROM substrate care of MAM-A in Colorado Springs, Co. Other methods, such as ink-jet printing laser printing onto acetate were also explored but produced results that suffered in either resolution(ink-jet, laser-printing), pixelation(ink-jet) or mounting difficulties(laser, ink-jet). Additionally, MAM-A explored the used of UV printer but even it didn't produce the desired resolution, Δk .

Patterns of arbitrary features can be produced on glass substrates, but they are expensive \$ 2000, and will require mounting to a suitable motor, and could shatter if the disks are spun at high speeds.

Additional work on the production of masks with high Δk values is warranted. It would be even

more desirable for these masks be reflective rather than absorptive. Such as could be done with metal patterning on the CD-ROM substrates. Such a mask may be usable infrared and well as in the visible and if based off of existing CD-ROM & DVD technology could be produced at a relatively low cost.

5.1.2 Removal of aberrations from the optical system

In Sec. C.1 showed through simulation that aberrations in the optical system lead to distortions to the envelope of the recoded temporal spatial frequency profile, leading to hard ripples on the edges of the object. Sec. B.4.2 & Sec. B.3.2 showed that optical systems composed of spherical lenses do suffer from aberrations which are related to phase on the systems OTF. The best way to design a optical system free of aberrations is to use computer ray tracing [40]. A common computer ray tracing program is ZeMax [41]. An analysis of the optical systems in SPIFI should be undertaken using program like ZeMax would lead to a diffraction limited system regardless of wavelength.

5.1.3 More efficient use of time-bandwidth product detector bandwidth & 2D

For illustration, a reversed biased ThorLabs DET100A, is a 10(mm)x10(mm) detector with 23Mhz, -3dB corner frequency. If the full 23 (MHz) bandwidth of detector could be used in SPIFI , at a line refresh speed of 100 Hz, it would allow for of 230,000 points per frame. In 1D SPIFI multiplex this is not possible, since in a 10 (mm) detector distance, with 550 (nm) radiation, the optical limit to the maximum number of points is $18000 = \frac{10 (mm)}{550 (nm)}$. This gap between the number of points the bandwidth of the detector can support and the number of points SPIFI could produce on its area, suggests the DET100A detector that is not being fully utilized in SPIFI .

This detector could be better utilized if the SPIFI modulator spun at a higher angular velocity, say around 1.2 (kHz) which would lead to 18,00 points per frame. This is not currently possible with the existing SPIFI modulator which has a motor that tops out at around 100 RPS. Instead, the other method to improve the use of the bandwidth of the detector is to further increase it's area. Increases in detector area will lower the bandwidth of the detector [12] detector while increasing the SPIFI bandwidth collected on its area.

An additional method to further put to use the electronic bandwidth of the detector is to devise a SPIFI modulator that encodes 2D information into the FD of the detector. Assuming the 2D information could be encoded across the detectors entire 2D area, then the 10(mm)x10(mm) detector could support $330,000,000 = \frac{100 (mm^2)}{550 (nm^2)}$ up to points. To collect this amount of points the frame rate of the detector would need to be lowered. If this is undesirable, simple reduction in the detectors

area corresponding to a decrease in the number of points may be acceptable.

5.1.4 Additional Modulation Methods

When we considered modulation formats, two additional formats seemed promising to produce frequency domain images. These are acousto-optic modulators(AOMs) and spatial light modulators(SLMs). SLMs have been developed for the projection TVs, and development kits are available. AOMs were of particular interest due to their high bandwidths, and reasonable cost.

Acousto-optic modulators(AOMs) and their larger aperture cousins acousto-optic beam deflectors work on the principle of photon-phonon interaction. The phonons are generated with a piezo transducer adhered to the side of the crystal, and driven by a RF waveform. When momentum and energy conservation conditions are met, the two particles mix and a photon shifted in frequency can be generated. The frequency shift is equal to the RF drive frequency, and the deflection angle is also proportional to the RF drive frequency. This is the mapping that is desired.

By varying the drive frequency, beam steering is possible and AOBs are often used for this purpose. AOBs are sold in 1D and 2D versions and the number of points depends on the size of the active device area and the RF bandwidth of the crystal. Since phonon energy and momentum are linearly related(dispersion), the position may be recoverable from the frequency of a RF heterodyne signal. The line update rate of a AO device is the time it takes for a photon to travel through the crystal. A typical device may have update rate of 10 (μ s), or 200,000 kHz. This would offer extremely high speed imaging.

Modulation with a SLM has been the least considered modulation method of current investigation. The cost of development goes up due to the computer interfacing requirements of the SLM. There the developer must spend time to learn the device and how to program it. The response time of SLMs is in the mili to 100 micro second range.

5.1.5 SPIFI onto a 1D array

The modulator presented in this work performs a 1D mapping between space and electronic frequency. The 1D spatial information was captured on a single element photodiode and the second dimension for the 2D images was acquired by scanning the sample through the beams focus. It is the second dimension of multiplexing the one currently done by SPIFI that is currently limiting the 2D SPIFI update rate.

If instead the beam was prepared to be square at the object and imaged onto a 1D photodiode array, each photo diode would have 1D spatial information encoded into its electronic signal while the

second dimension of this signal would vary as a function of the 1D array element. This would allow the line refresh speed to be brought up the rotation speed in the opto-mechanical modulator, 400Hz or potentially to 200,000 kHz in the acousto-optical format. Such a method would be extremely high speed imaging.

APPENDIX A

ADDITIONAL MATHEMATICAL DERIVATIONS AND CALCULATIONS

A.1 Direct transform frequency domain distribution

Starting with Eq. 2.4,

$$s_1(t) = |w(t)|^2 \int_{-\infty}^{\infty} |u(x)g(x)|^2 \cos [2\pi\kappa tx] dx \quad (\text{A.1})$$

Taking Eq. A.1 immediately to the frequency domain though Fourier transformation

$$S_1(f) = \int_{-\infty}^{\infty} \int_{-\infty}^{\infty} |w(t)|^2 |u(x)g(x)|^2 \cos [2\pi\kappa tx] dx e^{j2\pi ft} dt \quad (\text{A.2})$$

The spatial term, $|u(x)g(x)|^2$ has no time dependence so the orders of integration between time and space can be reversed, allowing the integral to be written as

$$S_1(f) = \int_{-\infty}^{\infty} |u(x)g(x)|^2 \int_{-\infty}^{\infty} |w(t)|^2 \cos [2\pi\kappa tx] dt dx \quad (\text{A.3})$$

The time domain integral

$$g(f, x) = \int_{-\infty}^{\infty} |w(t)|^2 \cos [2\pi\kappa tx] dt \quad (\text{A.4})$$

is the shifted fourier transform of the window function $\mathcal{W}(f) = \mathfrak{F} \{ |w(t)|^2 \}$.

$$g(f, x) = \frac{1}{2} \mathcal{W}(f + \kappa x) + \frac{1}{2} \mathcal{W}(f - \kappa x) \quad (\text{A.5})$$

Leading to a frequency domain waveform

$$S_1(f) = \frac{1}{2} \int_{-\infty}^{\infty} |u(x)g(x)|^2 \mathcal{W}(f + \kappa x) + |u(x)g(x)|^2 \mathcal{W}(f - \kappa x) dx \quad (\text{A.6})$$

Making the substitution, $x = \frac{f}{\kappa}$ shows this is just a two convolution integrals

$$\hat{S}_1(x' = f\kappa^{-1}) = \frac{1}{2} |u(x')g(x')|^2 \circledast \mathcal{W}(-\kappa f) + \frac{1}{2} |u(x')g(x')|^2 \circledast \mathcal{W}(\kappa f) \quad (\text{A.7})$$

with an upper side band identical to Eq. 2.50.

A.2 Map from space to frequency with magnifications between planes

The optical imaging systems to relay the field between, object, modulator, and image planes can easily be constructed to have non unity magnification. Incorporating the magnifications into theory adds magnification constants to the theory of Sec. 2.1.

This appendix presents the same derivation as but with the magnifications. The resulting math is very similar except number of arguments to the equations is increased due to the magnifications.

This section will assume a magnification, M_1 between the modulator and object planes, and a second magnification M_2 between the object and detector planes. The square law intensity signal of Eq. 2.1 now becomes

$$I(x, t) = I_0 \left| u \left(\frac{x}{M_1 M_2} \right) g \left(\frac{x}{M_2} \right) m \left(\frac{x}{M_1 M_2}, t \right) \right|^2 \quad (\text{A.8})$$

Using the same modulator, Eq. 2.2, this intensity distribution generates the square-law signal out of the detector

$$s(t) = \gamma \frac{I_0}{4} \int \left| u \left(\frac{x}{M_1 M_2} \right) g \left(\frac{x}{M_2} \right) \right|^2 |w(t)|^2 \left[\frac{3}{2} + 2 \cos \left(\frac{2\pi\kappa t}{M_1 M_2} \right) + \frac{1}{2} \cos \left(\frac{4\pi\kappa t}{M_1 M_2} \right) \right] dx \quad (\text{A.9})$$

that can be separated in terms of harmonics and scaled by γ and I_0 to be written as $s(t) = \frac{1}{2} [s_0(t) + s_1(t) + s_2(t)]$. $s_0(t) = |w(t)|^2 \int \frac{3}{4} \left| u \left(\frac{x}{M_1 M_2} \right) g \left(\frac{x}{M_2} \right) \right|^2 dx$ is a constant power term stationary in time. The time dependent signals s_1 and s_2 are the first and second harmonic bands of the modulation frequency with

$$s_1(t) = |w(t)|^2 \int |u(M_1^{-1} M_2^{-1} x) g(M_2^{-1} x)|^2 e^{\frac{j2\pi\kappa t x}{M_1 M_2}} dx + \text{c.c.} \quad (\text{A.10})$$

$$s_2(t) = \frac{1}{4} |w(t)|^2 \int |u(M_1^{-1} M_2^{-1} x) g(M_2^{-1} x)|^2 e^{\frac{j4\pi\kappa t x}{M_1 M_2}} dx + \text{c.c.} \quad (\text{A.11})$$

The first and second harmonic sidebands contain replicate information about the field distribution. We will concern ourselves with the first harmonic sideband, $s_1(t)$. The center frequency for the side band is determined by the centroid of the illumination field on the disc, $x_c = \int x |u(x)|^2 dx$. Shifting to the coordinate system of the field of interest the first harmonic side band term is

$$s_1(t) = |w(t)|^2 e^{j2\pi\kappa x_c t} \int |u(M_1^{-1} M_2^{-1} x) g(M_2^{-1} x)|^2 e^{j2\pi\kappa M_1^{-1} M_2^{-1} t x'} dx' + \text{c.c.} \quad (\text{A.12})$$

This integral takes the form of a spatial Fourier transform, where the spatial frequency, $fx \rightarrow \kappa M_1^{-1} M_2^{-1} t$

$$\mathcal{G}'(f_x) = \int |u(M_1^{-1}M_2^{-1}x)g(M_2^{-1}x)|^2 e^{j2\pi f_x x} dx \equiv \mathfrak{F} \{ |u(M_1^{-1}M_2^{-1}x)g(M_2^{-1}x)|^2 \}, \quad (\text{A.13})$$

we obtain an expression for the time-varying photodiode signal of

$$s_1(t) = 2|w(t)|^2 |\mathcal{G}'(M_1^{-1}M_2^{-1}\kappa t)| \cos(2\pi f_c t + \angle \mathcal{G}'(M_1^{-1}M_2^{-1}\kappa t)) \quad (\text{A.14})$$

where $\angle \mathcal{G}'$ is the phase of the spatial frequency distribution, \mathcal{G}' , and the center frequency is $f_c = \kappa x_c$. The Fourier transform of the temporal signal, $\hat{S}_1(f) = \mathfrak{F} \{s_1(t)\}$, shows a spectrum with sidebands decomposed as $\hat{S}_1(f) = M_1 M_2 \kappa^{-1} \hat{S}_{1+}(-f) + M_1 M_2 \kappa^{-1} \hat{S}_{1-}(f)$. The sidebands are the spatial extent of the illuminated intensity limited in resolution by convolution with the temporal window. The upper side band can be written as

$$\hat{S}_{1+}(f) = \mathcal{W}(f) \otimes |u(\kappa^{-1}f)g(M_1 \kappa^{-1}f)|^2 \quad (\text{A.15})$$

By inspection, the relationship between the spatial and frequency extent of the beam at the detector is $x' = M_1 M_2 \kappa^{-1} f$, and the positive frequency side band can be written as

$$\hat{S}_{1+}(x' = M_1 M_2 \kappa^{-1} f) = \mathcal{W}(M_1^{-1} M_2^{-1} \kappa x') \otimes |u(M_1^{-1} M_2^{-1} x')g(M_2^{-1} x')|^2 \quad (\text{A.16})$$

The mapping between space and frequency at the object plane is $x'' = M_1 \kappa^{-1} f$. Using this relation the upper side band can be written as

$$\hat{S}_{1+}(x'' = M_1 \kappa^{-1} f) = \mathcal{W}(M_1^{-1} \kappa x'') \otimes |u(M_1^{-1} x'')g(x'')|^2 \quad (\text{A.17})$$

From Eq. A.15 the magnification from the object to the detector plane, M_2 has no effect on the frequency content of the signal. M_2 should be set to maximize the area of the field that is collected onto the detector, and should be set to demagnify. There is an optical limit on M_2 , and the field cannot be demagnified through the diffraction limit. Also from Eq. A.15 the bandwidth collected on the detector is determined only by the size of the distribution of illumination field on the modulator, $u_1(x)$.

On the other hand, the magnification between the modulator and illumination planes, M_1 does have an effect on the spatial resolution of the object. From Eq. A.17 The spatial width of the window function \mathcal{W} to be convolved with the spatial extent of the object $|g(x)|$ is $M_1 \kappa^{-1}$. If this system is demagnifying then $|M_1|$ is less than one, and increasing the demagnification increases the resolution of the object.

A.2.1 Number of Points

If the time window of the traces is T , this corresponds to a resolution bandwidth of

$$BW_{res} = \frac{1}{T} \quad (\text{A.18})$$

From Eq. A.15, this determines the minimum amount of space that can be resolved by the system to be

$$dx = \frac{M_1 M_2}{\kappa T} \quad (\text{A.19})$$

The taking the size of the beam at the modulator plane to be ΔW , due to the magnifications at the detector plane it is of size

$$\Delta W' = M_1 M_2 \Delta W \quad (\text{A.20})$$

The number of points at the detector is the size of the illumination beam at the detector divided by the spatial resolution Eq. A.19. The magnifications cancel and the number of points is

$$N = \Delta W \kappa T \quad (\text{A.21})$$

The number of points is dependent only on the time window, the parameters of the beam at the modulator, and the modulator sweep parameter α , and does not change with magnification between planes.

A.3 Parameters for Disc Modulator

The implemented SPIFI imaging system utilized both the modulating disc of Sec. 3 and used imaging systems with magnifications between the planes. A presentation of the space to electronic temporal frequency mapping with magnifications was derived in Appendix A.2. In this section we map the disc and motor parameters, to the final equation of Appendix A.2, Eq. A.15.

As was written in Sec. 3 for the disc modulator the parameter

$$\kappa = f_m \Delta k \quad (\text{A.22})$$

and the center frequency is at

$$f_c = f_m k_0 + f_m \Delta k x_0 \quad (\text{A.23})$$

, where f_m is the rotation speed of the disc in rotations per second. The upper side band with the disc modulator can be written as

$$\hat{S}_{1+}(f) = \mathcal{W}(f) \otimes |u((f_m \Delta k)^{-1} f') g(M_1 (f_m \Delta k)^{-1} f)|^2 \quad (\text{A.24})$$

or realizing the mapping to space in the object plane $x' = M_1 f_m^{-1} \Delta k^{-1} f$

$$\hat{S}_{1+}(x' = M_1 f_m^{-1} \Delta k^{-1} f) = \mathcal{W}(M_1^{-1} f_m \Delta k x') \otimes |u(M_1^{-1} x') g(x')|^2 \quad (\text{A.25})$$

APPENDIX B

GENERAL OPTICAL CONSIDERATIONS

In Ch. 2 we have written the field distribution on the detector as a scaled(Appendix A.2) multiplicative function of the field distributions in the planes of the modulator and object. Experimentally, to reproduce the field distribution between the two planes two optical imaging systems will be employed.

The first method for dealing with the effect of the optical systems is to describe them using their PSF and ATF(Sec. B.1). This was done in Sec. 2.3.1. This appendix chapter deals with what the PSF and ATF for the optical system should be modeled as for general optical systems.

The ATF is a complex quantity which for hard apertures has a bandwidth determined by the NA of the optical system(Sec. B.1). Many optical systems suffer from aberrations and have a OTF with phase(Sec. B.4.2, B.4.3). A optical system with flat phased OTF is considered diffraction limited and corresponds to a transform limited PSF (Sec. B.4.2).

For the diffraction limited optical system the maximum periodicity that can be reproduced is dependent on the NA of the system [31]. Thus the NA sets the maximum time window of the SPIFI trace. For the case of the system with aberrations the PSF broadens(Sec. B.4.2) due to phase on the OTF and makes the system unable to reproduce the finer periodic structures of the mask leading to an expected shortening of the effective SPIFI time window $w(t)$ (Sec. 2.3.1) and a loss in electronic image resolution.

It is most common to construct imagers in the lab either in a single lens or telecentric configuration. The signal lens imager is just a lens placed with conjugate planes satisfying imaging conditions(Sec. B.3.1). Telecentric imagers, such as a telescope or modern infinity corrected microscope, consist of two lenses separated by their combined focal length with conjugate planes in the front and back focal planes of the input and output lenses(Sec. B.3.2).

The construction of these systems is typically done with spherical lenses and suffer from spherical aberrations(Sec. B.4.2, B.3.2). The first order method to correct for this is to use a parabolic lens as the parabolic lens produces a diffraction limited spot when propagated with paraxially (Sec. B.4.2) [33]. Unfortunately with the exact propagator for the $\frac{F}{1}$ lens simulated the parabolic lens does not produce a significantly smaller PSF than the spherical lens(Sec. B.4.2, B.4.3). The way

to produce a on-axis diffraction limited system is to ensure the on-axis point satisfies the Abbe sine condition [32]. A single lens imager designed in this method is undertaken using Fourier optics methods in Sec. B.4.2.1.

As the resolution on the SPIFI mask, Δk , becomes smaller the mask becomes more difficult to manufacture and get concentrically mounted, thus if one is interested in performing diffraction limited microscopy with SPIFI this interest will guide them to push the demagnification between the modulator and object planes to produce a spatial pattern in the object plane with the highest possible spatial frequency. It is for this reason that in Sec. B.3 the NA of two common optical systems is considered in detail as a function of the lens $\frac{F}{\#}$ and system magnification. Magnification also adds the complication as relative to what plane one discusses the PSF and OTF(Sec. B.2). The effect of magnification was also considered in the vignetting simulations of Sec. B.5.

Optical systems are not shift invariant, and their PSFs and OTFs should be considered as the point object moves transversely way from the origin of the system. This is called vignetting and is simulated in Sec. B.5 for the same two common optical systems as Sec. B.3 under 3 system magnifications. To characterize the vignetting the simulated width of the systems PSF in terms of FWHM was measured as a function of the objects offset from the optic axis. The inverse of the width function is a point density(Fig. B.22).

The point density in the vignetting plots falls off as the object point moves away from the optical axis(Fig. B.22). Thus these plots quantify both optical resolution and field of view, with the integral of the point density leading to the total number of points one would expect the optical system to support. The field of view of the optical system ultimately limits the maximum width of the illumination distribution and sets the electronic bandwidth of the SPIFI trace.

In choosing the optical systems, lenses, and magnifications to use between the SPIFI planes, one would expect that when and where the point density(Sec. B.5) is smaller than Δk there will be a loss of spatial frequencies leading to an effective shortening of the local SPIFI time window. From the vignetting plots(Sec. B.5), one should be able to choose a system, even a degraded one composed of spherical lenses out of a lens kit, that pushes the SPIFI resolution and field of view to the optical limits.

Bringing the numerical discussion to conclusion, the next chapter(Ch. C) simulates the SPIFI traces for optical systems that support the Δk point density and systems that do not. Demonstrating what actually happens to the object resolution.

B.1 Spatial Frequency, NA, and Abbe Resolution

An optical imaging system primarily consists of lenses and mirrors separated by distances satisfying imaging conditions. Perhaps the two most common imaging systems are the single lens and telescope. The propose of both systems is to reproduce the distribution of the optical field between input and output planes referred to as conjugate planes.

These systems can easily be configured to magnify or demagnify the field distribution. Under ideal conditions the field distribution at the image and object planes are related by

$$u_{\text{img}}(x) = u_{\text{obj}}\left(\frac{x}{M}\right) \quad (\text{B.1})$$

where M is the magnification.

The conjugate variable to space is spatial frequency. Spatial frequency has units of $(\frac{1}{\text{m}})$ and its angular counter part, angular spatial frequency has units of $(\frac{\text{rad}}{\text{m}})$. The field's angular spatial frequency distribution is related to the field's spatial distribution by Fourier transform.

$$\hat{U}(k_x) = \int_{-\infty}^{\infty} u(x)e^{-jk_x x} dx \quad (\text{B.2})$$

From the relation between the spatial distribution of the field at the two planes, Eq. B.1, and Fourier transform relations Eq. B.2, the angular spatial frequency distribution of the object and image fields are related by

$$\hat{U}_{\text{img}}(k_x) = \hat{U}_{\text{obj}}(Mk_x) \quad (\text{B.3})$$

equivalent to the spatial relation of Eq. B.1.

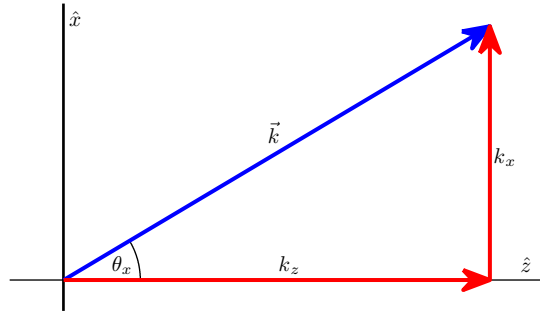


Figure B.1: 1D k-vector diagram

In addition to mathematical utility spatial frequency also has physical meaning. Fourier optics explains that the spatial frequency distribution of the field tells the distribution of angles in which the field propagates. The vector relationship is shown in Fig. B.1, where k is the wave number,

$k = \frac{2\pi}{\lambda}$. $k\hbar$ is proportional to the momentum of the photon, with controversy existing about where to put the index of refraction, n when in a medium [42]. The vector component, k_x is the physical interpretation of k_x from Eq. B.2. From the vector relation shown in Fig. B.1, k_x can be rewritten as the angle θ_x the field is propagating in relative to the optic axis, \hat{z} , through the simple relation

$$\sin \theta_x = \frac{k_x}{k} \quad (\text{B.4})$$

Fourier optics, see Goodman [33], explains that the phase $e^{-jk_z z}$, should be added to the k-space distribution to propagate the field a distance z in the \hat{z} direction. Additionally, quantum mechanics says that momentum is the generator of translation, and that $e^{-jk_z z}$ is the translation operator in the \hat{z} direction. Assuming the spatial field distribution at a plane, $u(x)$, with corresponding angular spatial frequency distribution, $U(\hat{k}_x)$ from Eq. B.2. To propagate the field in \hat{z} , the phase $e^{-jk_z z}$ should be added to the field but the field is not in a eigenbasis k_z it is in the basis k_x . Fortunately, if the wavenumber is known, the k_z can easily be related to k_x through the vector relationship

$$k^2 = k_x^2 + k_z^2 \quad (\text{B.5})$$

allowing the k-space propagator to be written in the k_x to be

$$H_{\text{prop}}(k_x; z) = e^{-j\sqrt{k^2 - k_x^2}z} \quad (\text{B.6})$$

Eq. B.6 can also be derived from the Helmholtz equation [33].

To propagate the field this angular spatial frequency phase term is simply multiplied against to the angular spatial frequency distribution

$$\hat{U}'(k_x; z) = e^{-j\sqrt{k^2 - k_x^2}z} \hat{U}(k_x; 0) \quad (\text{B.7})$$

This geometry shows angular spatial frequencies k_x of the spatial frequency distribution that exceeds the wave number, k , the square root becomes imaginary and the propagator becomes evanescent. These components of the distribution decay in a few wavelengths and are not appreciable between the systems' conjugate planes, referred to as the far-field. The propagator thus windows the spatial frequency distribution and does not pass angular spatial frequency components when $|k_x| > k$.

The geometry of the input to an optical system is shown in Fig. B.2. From the geometry, the aperture at the input to the optical system and the distance from the object plane to the aperture limits the spatial frequency bandwidth of the system. The maximum spatial frequency angle $\theta_{x \text{ max}}$ is related to the maximum angular spatial frequency by

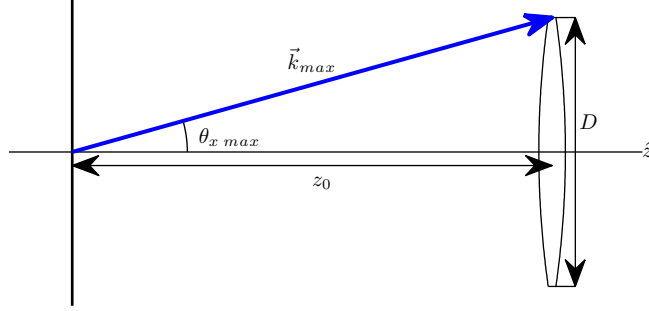


Figure B.2: Input aperture diagram

$$k_{x \max} = k \sin \theta_{x \max} \quad (\text{B.8})$$

In optical terminology, $\sin \theta_{x \max}$ is called the numerical aperture (NA) [32]. It is determined by geometry

$$\text{NA} = n \sin \theta_{x \max} = n \frac{R}{z_0^2 + R^2} \quad (\text{B.9})$$

where $R = \frac{D}{2}$ is the radius of the aperture, and n is the index of the medium between the object and lens had been added. In this discussion we have assumed this medium is air and $n = 1$. From Eq. B.8, the maximum spatial frequency can be written simply in terms of the NA and wave number by

$$k_{x \max} = k \text{NA} \quad (\text{B.10})$$

The spatial frequencies collected by the system are thus bandlimited by the aperture, and the object field spatial frequency distribution transmitted through the system can at best be written as

$$\hat{U}'_{\text{obj}}(k_x) = \text{rect}\left(\frac{k_x}{W_k}\right) \hat{U}_{\text{obj}}(k_x) \quad (\text{B.11})$$

where W_k sets the width of the window, and is twice $k_{x \max}$ or in terms of Eq. B.10,

$$W_k = 2 k \text{NA} \quad (\text{B.12})$$

The multiplying $\text{rect}()$ function is the input optical transfer function (OTF) of the system, and will be denoted as $\hat{P}_{\text{obj}}(k_x)$.

$$\hat{P}_{\text{obj}}(k_x) = \text{rect}\left(\frac{k_x}{W_k}\right) \quad (\text{B.13})$$

This means that to take account of the finite input aperture of the system, the spatial frequency distribution in the image plane should be written as

$$\hat{U}_{\text{img}}(k_x) = \hat{P}_{\text{obj}}(Mk_x) \hat{U}_{\text{obj}}(Mk_x) \quad (\text{B.14})$$

An diagram of the spatial frequency windowing by the aperture is shown in Fig. B.3.

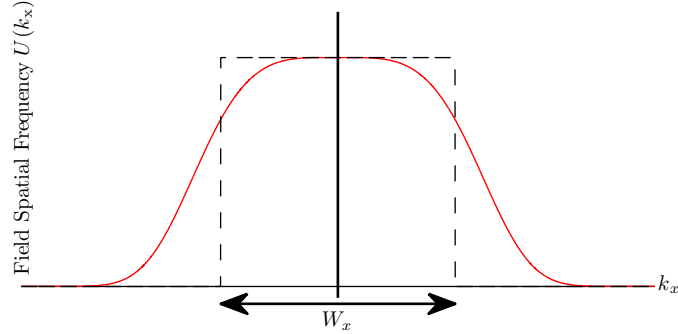


Figure B.3: Aperture spatial frequency windowing

The inverse Fourier transform of the OTF is the coherent point spread function (PSF) of the system. For the OTF of Eq. B.13 the PSF is

$$p(x) = \frac{1}{\sqrt{2\pi}} \text{sinc}\left(\frac{W_k x}{2\pi}\right) \quad (\text{B.15})$$

where $\text{sinc}(x)$ is the normalized sinc function defined as

$$\text{sinc}(x) = \frac{\sin \pi x}{\pi x}, \quad (\text{B.16})$$

that has zeros at $x = \pm 1, \pm 2, \pm 3, \dots$.

From Fourier transform relationships, and assuming spatial invariance, the PSF is convolved with the object field distribution causing image plane field reproduction of the object plane to be blurred

$$u'_{\text{obj}}(x) = \frac{1}{\sqrt{2\pi}} \text{sinc}\left(\frac{W_k x}{2\pi}\right) \otimes u_{\text{obj}}(x) \quad (\text{B.17})$$

The effect of spatial variance leads to vignetting which will be dealt with in Sec. B.5.

The blurring of convolution causes features smaller than the sinc function width, $\frac{2\pi}{W_k}$ not to be resolvable. There are many definitions the minimum distance between spots in which the spots are distinguishable. One of the most common is the Rayleigh criteria. The Rayleigh criteria of the resolvable separation of sinc functions, d_r , is the separation in which the main lobe of the next nearest point is on the first null of it's nearest neighbor as shown in Fig. B.4. Then this occurs when the argument of the sinc is equal to 1 thus

$$d_r = \frac{2\pi}{W_k} \quad (\text{B.18})$$

from Eq. B.12, and the definition of the wave number, the resolution is found to be

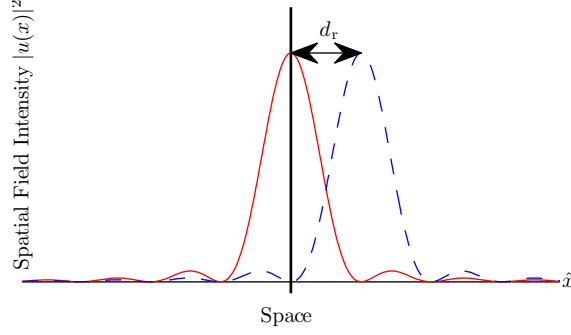


Figure B.4: Rayleigh sinc spatial resolution

$$d_r = \frac{\lambda}{2n \sin \theta_{x\max}} = \frac{\lambda}{2NA} \quad (\text{B.19})$$

Eq. B.19, is referred to as the diffraction limit and is considered to be co-discovered by Helmholtz [43] and Abbe [31]. [43] was the first to present its theoretical derivation although he claimed that the relation had been previous derived by J. Lagrange. Abbe also knew of Eq. B.19 and produced microscope objects that reached the Eq. B.19 limit, demonstrating it experimentally [31].

In [31] Abbe wrote,

“Though this expression applies in strictness only to the visibility of periodic structures composed of regularly arranged elements, it may be taken as a approximate measure of delineating power in general, i.e. in regard to structures of every composition. My theoretical investigations and experiments show that with objects of every shape and arrangement, the microscopical image will not present any indications of structures, the dimensions of which are perceptibly below the value of d_{obj} , given (for any aperture) by the above formula.”

B.2 Conjugate Plane Resolution and NA

It has just been shown that the object’s spatial resolution is limited by the spatial frequency bandwidth of the object OTF set by the input geometry to the system. On the output side of the system, Fig. B.5, the geometry limits the bandwidth of spatial frequencies focusable in the image plane. This can be once again quantified by the geometrical parameter NA , in this case labeled with subscript img denoting focusing into the image plane.

$$NA_{\text{img}} = \sin \theta_{x\max} = \frac{R}{z_1^2 + R^2} \quad (\text{B.20})$$

NA_{img} corresponds to the width of the image optical transfer function,

$$\hat{P}_{\text{img}}(k_x) = \text{rect} \left(\frac{k_x}{2kNA_{\text{img}}} \right) \quad (\text{B.21})$$

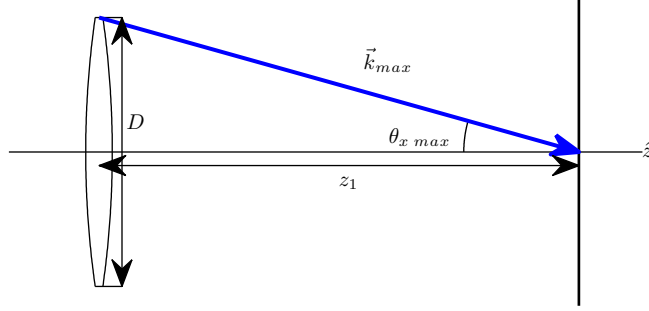


Figure B.5: Output aperture diagram

which defines the bandwidth of spatial frequencies that reach the image plane.

Including the effect of the input aperture, $\hat{P}_{\text{obj}}(k_x)$, output aperture, $\hat{P}_{\text{img}}(k_x)$, and magnification, M , the object plane spatial frequency distribution is modified from Eq. B.14 to be

$$\hat{U}_{\text{img}}(k_x) = \hat{P}_{\text{img}}(k_x) \hat{P}_{\text{obj}}(Mk_x) \hat{U}_{\text{obj}}(Mk_x) \quad (\text{B.22})$$

In the case of hard apertures, $\hat{P}_{\text{img}}(k_x)$ & $\hat{P}_{\text{obj}}(Mk_x)$ are described by the $\text{rect}()$ and Eq. B.22 is

$$\hat{U}_{\text{img}}(k_x) = \text{rect}\left(\frac{k_x}{2k\text{NA}_{\text{img}}}\right) \text{rect}\left(\frac{Mk_x}{2k\text{NA}_{\text{obj}}}\right) \hat{U}_{\text{obj}}(Mk_x) \quad (\text{B.23})$$

This is equivalent to

$$\hat{U}_{\text{img}}(k_x) = \text{rect}\left(\frac{Mk_x}{2k\text{NA}'_{\text{obj}}}\right) \hat{U}_{\text{obj}}(Mk_x) \quad (\text{B.24})$$

where

$$\text{NA}'_{\text{obj}} = \min(\text{NA}_{\text{obj}}, |M| \text{NA}_{\text{img}}) . \quad (\text{B.25})$$

This brings up a point which should now be clarified. In which plane do we reference when referring to resolution. If a 10x magnifying system minimum object resolution is 1 (um) spot this corresponds to a minimum image spot of 10 (um). Clearly, these values just scale by the magnification, but they are different.

In this thesis, unless otherwise specified, resolutions, PSFs, and OTFs, are referenced against the object plane. For example, if a imaging system produces a resolution limited point of 10 (um) in the image plane, with a magnification of 10x between the image and object plane, the system will be referred to of having a (object) resolution of 1 (um).

Combining the two OTFs to one scaled in to the object plane,

$$\hat{P}'_{\text{obj}}(k_x) = \hat{P}_{\text{img}}\left(\frac{k_x}{M}\right) \hat{P}_{\text{obj}}(k_x) . \quad (\text{B.26})$$

It's Fourier transform considers the effect of both input and outputs to the system and is the image plane PSF scaled back to the object plane convolved with the object plane PSF.

$$p'_{\text{obj}}(x) = p_{\text{img}}(Mx) \otimes p_{\text{obj}}(x) \quad (\text{B.27})$$

The ' denotes a PSF or OTF scaled to the object plane.

B.3 NA Analysis of Common Optical Systems

The NA of the optical relay system can limit the SPIFI image resolution (Sec. 2.3.1). For constructing imaging systems the common configurations of a single lens and telescope are often employed and in this section their NAs are analyzed as function of magnification.

The single lens imager is a lens with the conjugate planes spaced to satisfy the single lens imaging condition. The telescope is a two lens imaging system with the lenses separated by their combined focal lengths. The telescope configuration commonly used in the construction of a infinity corrected microscope a objective first lens, which is a short focal length high NA compound lens, and the second longer lens, typically between 150 and 200 (mm) depending on manufacturing, referred to as the tube lens used to produce real image.

From the discussions of the previous two sections (Sec. B.2, 2.3.1, for the case of the hard input and output apertures Eq. B.24 and NA'_{obj} puts a upper limit on the electronic image resolution. The input NA and output NA scaled to the object plane will now be analyzed for these systems as a function of magnification to determine which NA is lower limiting the image resolution.

B.3.1 Single Lens Imaging System

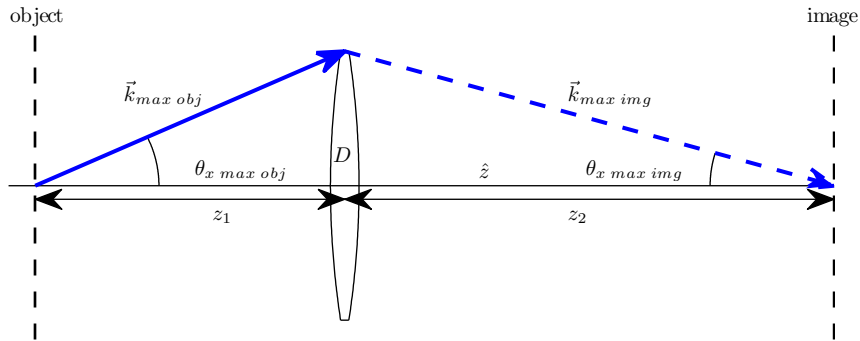


Figure B.6: Single lens imager diagram

The simplest and perhaps most common imaging system is one composed of a single lens. A single lens imaging system is shown in Fig. B.6. The distance from the object plane to the lens, z_1 , and the distance from lens to the image plane, z_2 must satisfy the simple lens formula

$$\frac{1}{z_1} + \frac{1}{z_2} = \frac{1}{f} \quad (\text{B.28})$$

where f is the focal length of the lens. The optical magnification is directly proportional to the ratio of the distances z_1 and z_2 ,

$$M = -\frac{z_2}{z_1} \quad (\text{B.29})$$

and the image is inverted between the planes as represented by the negative sign. Combining Eq. B.28 and Eq. B.29, z_1 and z_2 can be written in terms of the desired magnification and the focal length of the lens

$$z_1 = \frac{M - 1}{M} f \quad (\text{B.30a})$$

$$z_2 = (1 - M) f \quad (\text{B.30b})$$

Since z_1 and z_2 are both dependent on the magnification so is the input NA and output NA,

$$\text{NA}_{\text{obj}}(M) = \frac{R}{\sqrt{z_1^2 + R^2}} \quad (\text{B.31a})$$

$$\text{NA}_{\text{img}}(M) = \frac{R}{\sqrt{z_2^2 + R^2}} \quad (\text{B.31b})$$

where R is the radius of the aperture. Combining with Eq. B.30, these NA can be written as

$$\text{NA}_{\text{obj}}(M) = \frac{R}{\sqrt{(1 - \frac{1}{M})^2 f^2 + R^2}} \quad (\text{B.32a})$$

$$\text{NA}_{\text{img}}(M) = \frac{R}{\sqrt{(1 - M)^2 f^2 + R^2}} \quad (\text{B.32b})$$

To separate the physical properties of the lens from how it is used, the dimensionless parameter ζ will be defined as

$$\zeta = \frac{f}{R} \quad (\text{B.33})$$

and is twice the f-number, $\frac{f}{\#}$, of the lens. For example a $\frac{f}{2}$ would correspond to a $\zeta = 4$, and a $\frac{f}{3}$ would correspond to a $\zeta = 6$. Separating the parameters of the lens from how it is used the NAs of the lens is

$$\text{NA}_{\text{obj}}(M) = \frac{1}{\sqrt{1 + \zeta^2 (1 - \frac{1}{M})^2}} \quad (\text{B.34a})$$

$$\text{NA}_{\text{img}}(M) = \frac{1}{\sqrt{1 + \zeta^2 (1 - M)^2}} \quad (\text{B.34b})$$

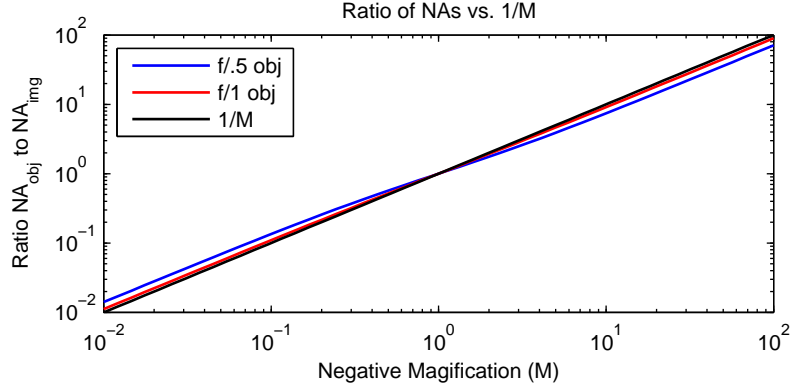


Figure B.7: Ratio, $\frac{NA_{obj}}{NA_{img}}$ vs. M . Functions do not overlap.

The ratio of $NA_{obj}(M)$ to $NA_{img}(M)$ is not M as one may expect from Eq. B.24. Instead the ratio is slightly off with the difference increasing with decreasing $\frac{f}{\#}$ as plotted in Fig. B.7 This means that when NA_{img} (Eq. B.34b) is rescaled to the object plane it is not equal to NA_{obj} instead it is equal to

$$NA'_{obj}(M) = \frac{M}{\sqrt{1 + \zeta^2 (1 - M)^2}} \quad (\text{B.35})$$

At best it can be written as

$$NA'_{obj}(M) = \frac{1}{\sqrt{\frac{1}{M^2} + \zeta^2 (1 - \frac{1}{M})^2}} \quad (\text{B.36})$$

with a leading $\frac{1}{M}$ term instead of a 1 in the square root. Hence, when the NA_{obj} is compared against NA_{img} scaled back to the input using Eq. B.36, under any magnification except for $M = -1$, one will be smaller than the other. In the case of $M = -1$ the system is symmetrical and they are equal. This comparison is shown in Fig. B.8 for three different $\frac{f}{\#}$ lenses.

Additionally, as suggested by Fig. B.7, and seen in Fig. B.8 as the $\frac{f}{\#}$ increases the difference between object NA and image NA scaled to the object plane is reduced.

Although it is perhaps not clear, for magnifying systems, $|M| > 1$, the $NA_{obj}(M)$ is always smaller than the $NA_{img}(M)$, scaled to the input, $NA'_{obj}(M)$, and for the demagnifying case the opposite is true. This means that when using a single lens a to magnify system, the NA on the input limits the image resolution and when used to demagnify the NA at the output limits the image resolution.

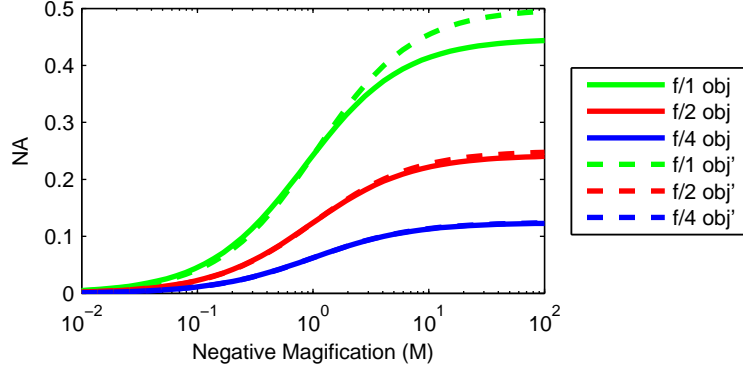


Figure B.8: NA vs. Magnification for three $\frac{F}{\#}$ ratios. Solid lines are NA_{obj} from input geometry, dashed lines are NA_{img} from output geometry scaled to the object plane to be $NA'_{\text{obj}}(M)$ Eq. B.36

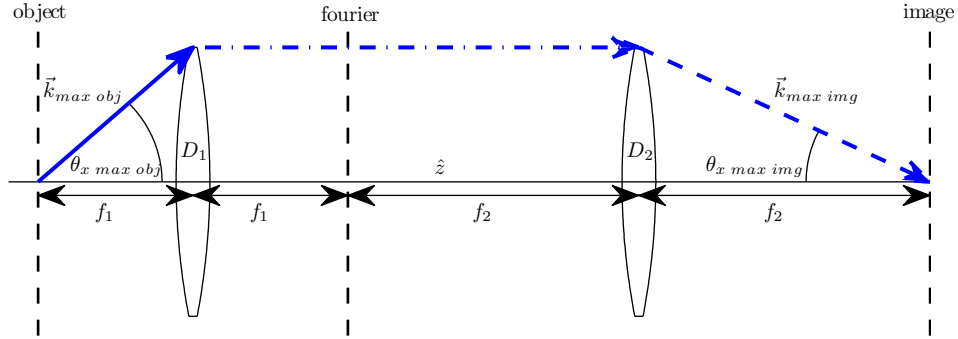


Figure B.9: Telecentric imager diagram

B.3.2 Telecentric and Infinity Corrected Microscopes

A telecentric imaging system (Fig. B.9) consists of two lenses separated by their combined focal lengths. The optical system has conjugate image planes in the front focal plane of the first lens and the back focal plane of the second lens. The magnification between the conjugate planes is the ratio of the focal lengths

$$M = -\frac{f_2}{f_1} \quad (\text{B.37})$$

For positive focal lengths, the magnification is negative and the image is inverted between image and object planes.

The input NA and output NA of the system are determined by the focal length of the lenses and

lens diameters

$$\text{NA}_{\text{obj}} = \frac{R_1}{\sqrt{f_1^2 + R_1^2}} \quad (\text{B.38a})$$

$$\text{NA}_{\text{img}} = \frac{R_2}{\sqrt{f_2^2 + R_2^2}} \quad (\text{B.38b})$$

The NA s can be written to be a function of the $\frac{F}{\#}$. We defined the parameter ζ (Eq. B.33) related to $\frac{f}{\#}$ to make it easier to work with the algebra of these parameters.

$$\zeta_{\text{in}} = \frac{f_1}{R_1} \quad (\text{B.39a})$$

$$\zeta_{\text{out}} = \frac{f_2}{R_2} \quad (\text{B.39b})$$

finding

$$\text{NA}_{\text{obj}} = \frac{1}{\sqrt{1 + \zeta_{\text{in}}^2}} \quad (\text{B.40a})$$

$$\text{NA}_{\text{img}} = \frac{1}{\sqrt{1 + \zeta_{\text{out}}^2}} \quad (\text{B.40b})$$

From Eq. B.25, for NA_{img} to be worse than NA_{obj} it must be smaller than $\frac{1}{M}$ times NA_{obj} , and for them to be equal

$$\text{NA}_{\text{img}} = \frac{\text{NA}_{\text{obj}}}{|M|} \quad (\text{B.41})$$

From Eq. B.41, for a magnifying system, $|M| > 1$ and the NA requirement on the input lens is higher than the NA requirement on the output lens. To reach the maximum imaging resolution, the highest NA lens available should be used as the input lens to the system. From Eq. B.40 the lens with the largest NA is the lens with the smallest $\frac{f}{\#}$. The NA_{obj} though the magnification(Eq. B.41) defines the smallest value of NA_{img} such that the input optic is limiting on the resolution(Eq. B.24). Since NA is inversely dependent on $\frac{F}{\#}$ (Eq. B.40b) this then sets the maximum $\frac{F}{\#}$ lens that can be used in the output of the system by

$$\frac{\text{NA}_{\text{obj}}}{M} = \frac{1}{\sqrt{1 + \zeta_{\text{out}}^2}} \quad (\text{B.42})$$

or

$$\zeta_{\text{out}} = \sqrt{\frac{M^2}{\text{NA}_{\text{obj}}^2} - 1} \quad (\text{B.43})$$

Larger magnifications lessen the requirement on the $\frac{f}{\#}$ of the output lens. Eq. B.43 only applies for, $|M| > 1$, as long as NA_{obj} is less than one the value of ζ_{out} will be real. Substituting Eq. B.40a, into Eq. B.43, the relation between input $\frac{F}{\#}$ and output $\frac{F}{\#}$ can be written directly as

$$\zeta_{\text{out}} = \sqrt{M^2 (1 + \zeta_{\text{in}}^2) - 1} \quad (\text{B.44})$$

For the case of $|M| = 1$, the expected symmetric result $\zeta_{\text{out}} = \zeta_{\text{in}}$ is found.

In the case of demagnification, $|M| < 1$ the NA requirement on the output lens is higher than on the input (Eq. B.41). Thus to reach the maximum resolution, the highest NA lens should be used for NA_{img} . From Eq. B.41, this lens then sets the minimum NA_{obj} , which determines the maximum $\frac{F}{\#}$ lens that can be used at the input without limiting the resolution. Thus the maximum $\frac{F}{\#}$ of the input lens is related to the magnification and out NA by

$$M \text{NA}_{\text{img}} = \frac{1}{\sqrt{1 + \zeta_{\text{in}}^2}} \quad (\text{B.45})$$

or

$$\zeta_{\text{in}} = \sqrt{\frac{1}{M^2 \text{NA}_{\text{img}}^2} - 1} \quad (\text{B.46})$$

For larger demagnification the minimum $\frac{F}{\#}$ increases. Substituting Eq. B.40a into Eq. B.46, one finds

$$\zeta_{\text{in}} = \sqrt{\frac{1 + \zeta_{\text{out}}^2}{M^2} - 1} \quad (\text{B.47})$$

which converges to $\zeta_{\text{in}} = \zeta_{\text{out}}$ for the case $|M| = -1$.

So for the telescope the highest NA lens should be used on the input if magnification is desired. This NA then sets the maximum $\frac{F}{\#}$ that can be used in the output. For the case of demagnification the highest NA lens should be used on the output setting the maximum $\frac{F}{\#}$ lens that can be used on the input.

B.3.3 Comparison between NA of Single Lens and Telescope

In Sec. B.4.2 the minimum object NA was inversely dependent on the lens $\frac{F}{\#}$ and the magnification in which it was used. In Sec. B.3.2 the highest lens NA available, associated with the lens with lowest $\frac{F}{\#}$, should be used at the input when magnifying and the output when demagnifying. This lens then set the maximum $\frac{F}{\#}$ lens parable to complete the telescope.

These systems can be compared as a function of magnification assuming the minimum $\frac{F}{\#}$ lens is the one used in the single lens imager, and that this lens governs the minimum resolution of the telescope. This comparison with the NA scaled to the object plane is shown in Fig. B.10 for three

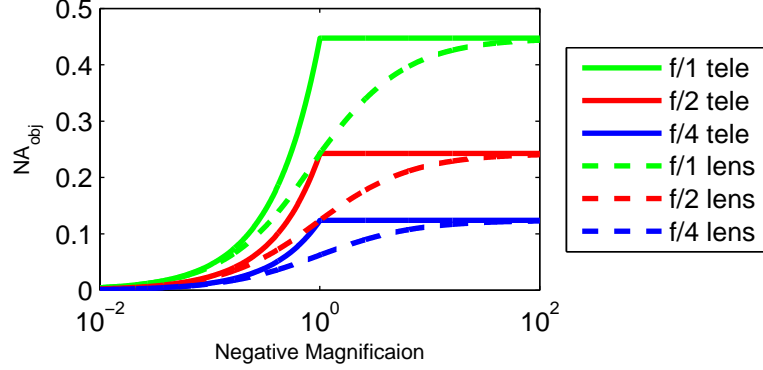


Figure B.10: Comparison between telescope and single lens NA for three $\frac{f}{\#}$. The NA of the telecentric imager is always higher than that of a single lens.

$\frac{f}{\#}$ lenses. From Sec. B.3.2 telecentric imager's magnification should be changed by altering the focal length of the second lens. Thus for magnification the telecentric imager has a object NA that is a function of just the lenses $\frac{f}{\#}$, in Fig. B.10.

From Fig. B.10, for a given minimum $\frac{f}{\#}$ the telecentric imager has a higher object plane NA than the single lens imager. For increasing magnifications, the NA of the single lens approaches the NA of the telecentric imager, and for demagnification, the telecentric imager also has higher NA approaching that of the single lens. The kink in the telescope object plane NA transferring to demagnification is due to switching the low $\frac{f}{\#}$ optic to the output where its NA scaled to the input becomes limiting.

B.4 Simulations

In the laboratory the single lens imager and telescope are typically constructed from spherical lenses, often just taken out of a already available lens kit. Using spherical lenses to build these systems, creates a imaging systems that suffers from aberration.

The spherical lens field transmission function is given by [33],

$$t(x) = \exp(-jk\Delta_0) \exp(jk(n-1)\Delta(x,y)) \text{rect}\left(\frac{x}{D}\right) \quad (\text{B.48})$$

$$\Delta(x,y) = \Delta_0 - R_1 \left(1 - \sqrt{1 - \frac{x^2}{R_1^2}}\right) + R_2 \left(1 - \sqrt{1 - \frac{x^2}{R_2^2}}\right) \quad (\text{B.49})$$

where D is the diameter of the lens, and R_1, R_2 are the radii of curvature, the parameters, $\Delta(x,y)$ and Δ_0 are shown in Fig. B.11. The first order method to correct for spherical aberrations is to change the lens phase function to a parabolic form,

$$t(x) = \exp\left(-j \frac{kx^2}{2f}\right) \text{rect}\left(\frac{x}{D}\right) \quad (\text{B.50})$$

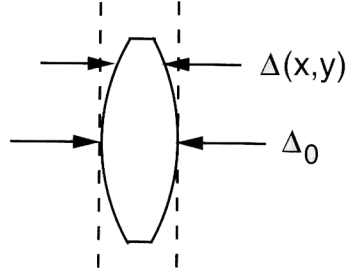


Figure B.11: Diagram of spherical Lens from Pg. 98 of [33].

[33] where f is the focal length. Even this doesn't fully correct the aberration and manufactures produce aspherical lenses with even higher order terms [35].

This section presents the results of numerical simulations that investigate the ability of the single lens and telescope to reproduce the object field in terms of PSF when constructed out of spherical and parabolic lenses. The simulations in this section seek to answer the questions of what the limits to the spherical lens systems are, and compares their performance against the same systems constructed higher cost parabolic lenses which is the first order correction.

Since the radiation used in the experiment (Ch. 4) came from a fiber laser with center wavelength of $\lambda = 1550$ (nm), this was the wavelength used throughout the simulations.

The computational steps in each numerical simulation is outlined in the flow cart of Fig. B.12. For the telescope the steps in the box labeled, "For Each Lens" is repeated for each lens in the imaging system.

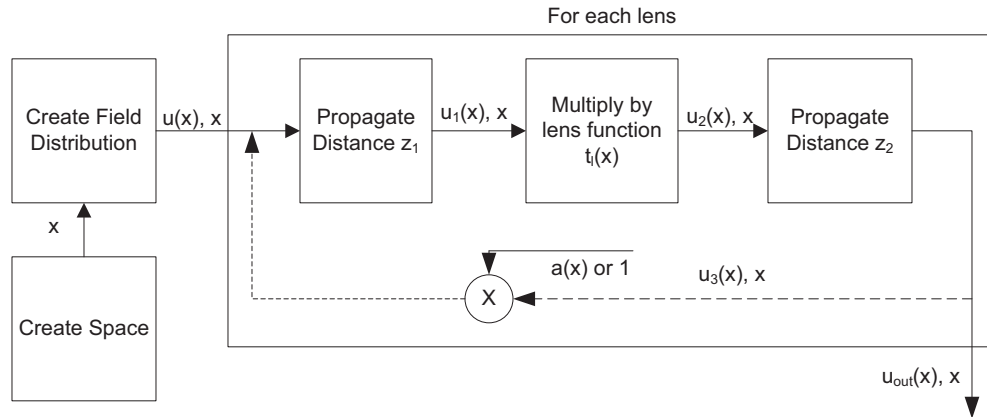


Figure B.12: Flow chart of simulations

All field distributions, $u(x)$, propagators, $H(k_x; z)$, and lens functions, $t_1(x)$, must be well sampled in both space and spatial frequency. The sampling requirements setting the minimum number of points for required for the simulation and is used in the first step of Fig. B.12 to create the space.

The sampling requirements will be considered in the next section (Sec. B.4.1).

Using this space, the simulation results of the on axis PSF of the single lens and telescope in a unity magnification configuration are presented in Sec. B.4.2 & Sec. B.4.3. A even more descriptive view of these systems includes the changes to the PSF when the source point is offset from the optic axis. This is called vignetting and simulations of its effect on these are presented in Sec. B.5.

B.4.1 The Spatial Simulation Parameters

The number of points in a spatial simulation is determined by the size of the space, Δx , and the spacing between points δx , by $N = \frac{\Delta x}{\delta x}$. δx defines the maximum band of spatial frequencies, $k_{x\max}$ that can be supported in the numerical simulation though

$$k_{x\max} = \frac{k_s}{2} \quad (\text{B.51})$$

where $k_s = \frac{2\pi}{\delta x}$, is the angular sampling frequency. Since δx determines the maximum spatial frequency supported in the simulation it also determines the smallest resolvable spot the field can become. The second thing to consider is that $k_{x\max}$ must be greater than the absolute value of the highest local spatial frequency, $|k_{x\text{loc}}(x)|$, of the lens function. The local spatial frequency any spatial phase function, $\phi(x)$ is its first derivative

$$k_{x\text{loc}}(x) = \frac{d\phi(x)}{dx} \quad (\text{B.52})$$

$k_{x\max}$ For Parabolic Lens

The parabolic lens has a phase function of

$$\phi(x) = -\frac{kx^2}{2f} \quad (\text{B.53})$$

and an instantaneous angular spatial frequency

$$\frac{d\phi(x)}{dx} = -\frac{kx}{f} \quad (\text{B.54})$$

We are interested in the maximum magnitude of the local angular spatial frequency, $k_{x\max}$, this occurs at the radius of the lens, $R = D/2$.

$$k_{x\max} = \frac{kD}{2f} \quad (\text{B.55})$$

This is directly related to the $\frac{f}{\#}$ of the lens. For a $\frac{f}{1}$ lens $k_{x\max} = .5k$, and $k_{x\max}$ goes down from there with increasing f-number.

$k_{x\max}$ For Spherical Lens

The spherical lens has a phase function of

$$\phi(x) = -k\Delta_0 + k(n-1) \left[\Delta_0 - R_1 \left(1 - \sqrt{1 - \frac{x^2}{R_1^2}} \right) + R_2 \left(1 - \sqrt{1 - \frac{x^2}{R_2^2}} \right) \right] \quad (\text{B.56})$$

and an instantaneous angular frequency of

$$\frac{d\phi(x)}{dx} = k(n-1) \left(-\frac{\frac{x}{R_1}}{\sqrt{1 - \frac{x^2}{R_1^2}}} + \frac{\frac{x}{R_2}}{\sqrt{1 - \frac{x^2}{R_2^2}}} \right) \quad (\text{B.57})$$

For a biconvex lens, $R_2 = -R_1$, leaving

$$\frac{d\phi(x)}{dx} = k(n-1) \left(-\frac{2x}{R_1 \sqrt{1 - \frac{x^2}{R_1^2}}} \right) \quad (\text{B.58})$$

The maximum magnitude occurs when $x = D/2$, and the maximum spatial frequency increases with decreasing radius of curvature, R_1 . For the $\frac{f}{\#} = 25$ (*mm*) ThorLabs Biconvex BK7(LB1761) lens considered in this section,

$$(n-1) \left(-\frac{2x}{R_1 \sqrt{1 - \frac{x^2}{R_1^2}}} \right) = .6244 \quad (\text{B.59})$$

would set $k_{x\max} = .6244k$, which is higher than for the parabolic lens.

Choice of $k_{x\max}$

In these simulations the ability of the optical systems to resolve a diffraction limited spot is tested. The input to the system will be the square band of all propagating spatial frequencies, which can be written as the a spatial frequency field

$$U(k_x) = \text{rect}\left(\frac{k_x}{2k}\right) \quad (\text{B.60})$$

No lenses with $\frac{f}{\#}$ shorter than $\frac{f}{1}$ are used in the simulation. The spatial frequency bandwidth of the input field was higher than the maximum local spatial frequency for the $\frac{f}{1}$ lens, $k_{x\max}$, which determines the sampling frequency, set to twice k , allowing the input spatial frequency distribution to occupy half of the simulation bandwidth, shown in Fig. B.14 (b).

$$k_{x\max} = 2k \quad (\text{B.61})$$

B.4.1.1 Choice of Δx

Propagations are performed by multiplying the angular spatial frequency distribution of the field $\hat{U}(k_x)$ by the spatial frequency propagator Eq. B.6. The phase of Eq. B.6, $\phi(k_x)$ needs to be sampled at least two time per period to satisfy the Nyquist criteria. Since the first derivative of the spatial phase, $\phi(x)$ function is the angular local spatial frequency function, $k_{x\text{loc}}(x)$, the first derivative of the angular spatial frequency phase function, $\phi(k_x)$ would be called the local spatial function $x_{\text{loc}}(k_x)$.

$$x_{\text{loc}}(k_x) = \frac{d\phi(k_x)}{dk_x} \quad (\text{B.62})$$

Analogous to the spatial frequency discussion, the size of the space Δx should satisfy

$$\Delta x \geq 2 \max |x_{\text{loc}}(k_x)| \quad (\text{B.63})$$

This will sperate samples in spatial frequency by

$$\delta k_x = \frac{2\pi}{\Delta x} \quad (\text{B.64})$$

which will sample the phase at least twice over 2π accumulation.

Δx for exact propagator, Eq. B.6

The phase of the exact angular spatial frequency free space propagator is

$$\phi(k_x) = -\sqrt{k^2 - k_x^2}z \quad (\text{B.65})$$

A plot of this angular phase function is shown in Fig. B.13 (a).

Taking the first derivative of the spatial frequency phase function

$$x_{\text{loc}}(k_x) = \frac{zk_x}{\sqrt{k^2 - k_x^2}} \quad (\text{B.66})$$

z is just a constant multiplier against the term, $\frac{k_x}{\sqrt{k^2 - k_x^2}}$, a plot of $\frac{k_x}{\sqrt{k^2 - k_x^2}}$ for $\lambda = 1550$ (nm). This function has asymptotes that tend to infinity as k_x approaches $\pm k$.

$$\begin{cases} \lim_{k_x \rightarrow +k} \frac{zk_x}{\sqrt{k^2 - k_x^2}} = \infty \\ \lim_{k_x \rightarrow -k} \frac{zk_x}{\sqrt{k^2 - k_x^2}} = -\infty \end{cases} \quad (\text{B.67})$$

Since the local space function goes to infinity, as $k_x \rightarrow k$, the point separation in spatial frequency, δk_x can never be made small enough to properly sample the phase of H_{prop} , as k_x goes through k .

A maximum value, $k_{x \max}$ must be chosen to prevent the phase from aliasing. The value of $k_{x \max}$ sets the maximum of $x_{\text{loc}}(k_x)$ which determines the minimum size of the simulation space

$$\Delta x \geq \frac{2zk_{x \max}}{\sqrt{k^2 - k_{x \max}^2}} \quad (\text{B.68})$$

To avoid aliasing the spatial frequency propagator Eq. B.6, must be windowed by $k_{x \max}$ making it

$$H_{\text{prop}}(k_x; z) = e^{-j\sqrt{k^2 - k_x^2}z} \text{rect}\left(\frac{k_x}{2k_{x \max}}\right) \quad (\text{B.69})$$

The minimum required size of the transverse space, Δx can be separated by the distance of the propagation, z , and a unit less scalar

$$\mathcal{K}(k_{x \max}) = \frac{2k_{x \max}}{\sqrt{k^2 - k_{x \max}^2}} \quad (\text{B.70})$$

to be

$$\Delta x \geq z\mathcal{K}(k_{x \max}) \quad (\text{B.71})$$

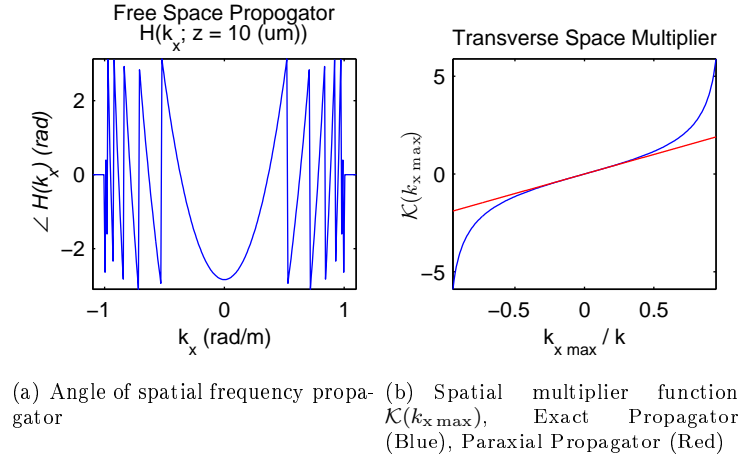


Figure B.13: The real part of the spatial frequency propogator (a) increasing spatial frequency density (b)

Δx for paraxial propagator

A approximation often made to the exact propagator is a parabolic expansion of the square root. This is called the paraxial or small angle approximation. The paraxial propagator can be written in spatial frequency as

$$H(k_x; z) = e^{-jkz} \left(1 - \frac{k_x^2}{2k^2}\right) \quad (\text{B.72})$$

From the phase of the local spatial extent of the beam is

$$x_{\text{loc}}(k_x) = \frac{zk_x}{k} \quad (\text{B.73})$$

which increases linearly with k_x .

$$\Delta x \geq \frac{2zk_x}{k} \quad (\text{B.74})$$

like the exact propagator case, this can be separated into z times a function

$$\mathcal{K}(k_{x \text{ max}}) = \frac{2k_x}{k} \quad (\text{B.75})$$

, the maximum propagating value is when $k_x = k$, therefore the maximum value of the propagator should be windowed by k making it

$$H(k_x; z) = e^{-jkz} \left(1 - \frac{k_x^2}{2k^2}\right) \text{rect}\left(\frac{k_x}{2k}\right) \quad (\text{B.76})$$

and the maximum value of $\mathcal{K}(k_{x \text{ max}}) = 2$. A plot of $(K)(k_{x \text{ max}})$ for the paraxial and exact propagators are compared in Fig. B.13 (b)

B.4.2 Single Lens

The PSF and OTF of a single lens under unity magnification, $z_1 = z_2 = 2f$, was simulated for the spherical and parabolic lens. The resulting PSF and OTF are compared to that expected from the NA of the lens (Eq. B.15, & Eq. B.13). The lens parameters used are that of the shortest focal length lens ($f = 25.4$ (mm)) in a 1 (in) diameter lens kit ($D = 25.4$ (mm)). In a unity magnification condition, this system would have a NA = .2425 (Eq. B.34), and Abbe resolution of $d_r = 1.87$ (um). The diffraction limited OTF (Eq. B.24), referred to as the Abbe OTF, and the theoretical PSF is referred to as the Abbe PSF (Eq. B.27) and is related to the OTF by Fourier transform.

To allow for the smallest possible point to be created in the image plane of the simulations, the angular spatial frequency field distribution in the object plane (Fig. B.14 (b)) consisted of all propagating spatial frequencies

$$\hat{U}_o(k_x) = \text{rect}\left(\frac{k_x}{2k}\right) \quad (\text{B.77})$$

The maximum angular frequency supported by the simulation was twice the frequency band of the object field, $k_s = 4k$, making $\delta x = 387$ (nm).

The space was created to well sample the exact spatial frequency propagator to $k_{x \text{ max}} = .95k$. Since the total distance is $4f$, the distance for the propagator was $z = 101.6$ (mm). The size of the

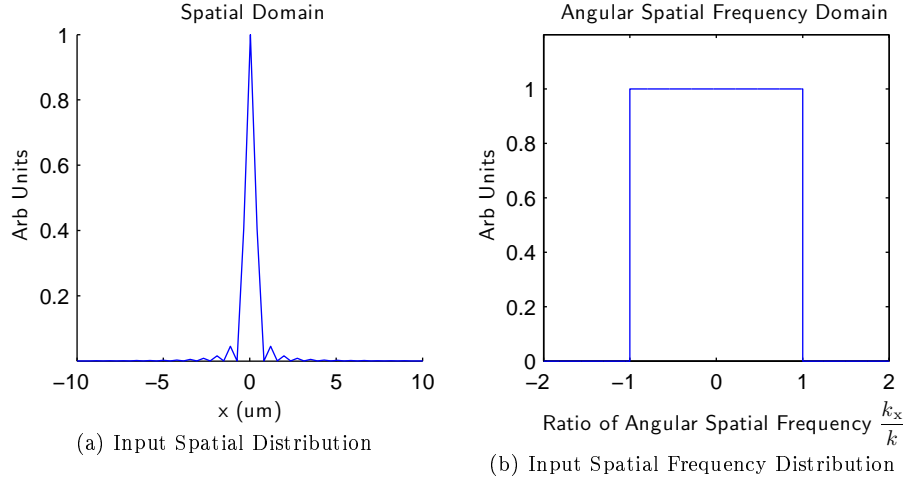


Figure B.14: The input spatial (a) and spatial frequency (b) distributions used in the simulations. The input spatial frequency distribution consisted of all propagating spatial frequencies.

space was set to

$$\Delta x = z1.5\mathcal{K}(k_{x\max}) \tag{B.78}$$

with the 1.5 to add an additional tolerance to the minimum space required (Eq. B.70). The transverse extent of the space was $\Delta x = 539.2$ (mm), and contained spatial points separated by δx for a total of $N_{\text{sim}} = 4,786,241 = 2^{22.19}$ points. The square-law intensity of the input spatial distribution, $|u_o(x)|^2$ and input angular spatial frequency distribution, $|\hat{U}_o(k_x)|$ are shown in Fig. B.14.

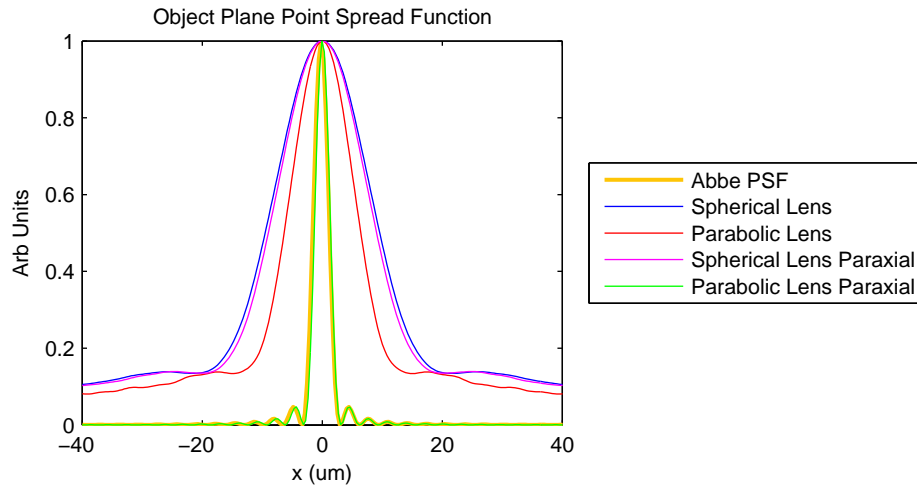


Figure B.15: Point Spread Function Comparison for $f = 25$ (mm), $D = 25.4$ (mm) lenses. The spherical(blue) and parabolic lens(red) PSFs are larger than Abbe(gold) due to aberrations. If the propagator is changed from the exact one to paraxial, the parabolic lens produces a diffraction limited PSF(green) overlapping the Abbe PSF. The spherical lens still produces a aberrated PSF(maroon) when used with the paraxial propagator.

Method	FWHM	% Abbe
Abbe	2.83 (um)	-
Spherical Lens Exact	19.4 (um)	14.5
Parabolic Lens Exact	13.0 (um)	21.7
Spherical Lens Paraxial	18.4 (um)	14.4
Parabolic Lens Paraxial	2.75 (um)	103

Table 1: FWHM for Single Lens PSF of Fig. B.15

The image plane PSFs, $|p_{\text{img}}(x)|^2$ are shown in Fig. B.15, since $M = -1$ they are identical when projected into the object plane. The profile of the PSF of the spherical lens(blue), and parabolic lens(red) do not overlap the PSF of Abbe. Instead they are broader and have a pedestal.

One may expect that the parabolic lens should have performed better, if the field between the parabolic lens conjugate planes is propagated with a paraxial propagator the phases cancel allowing for ideal imaging [33]. Thus the simulations of PSF with the spherical and parabolic lens were repeated with the paraxial propagator and are also compared in Fig. B.15. As expected parabolic lens with the paraxial propagator produces a PSF(green) that overlaps that of Abbe(gold). For the case of the paraxial propagator the spherical lens PSF(maroon) is only slightly smaller than with the exact propagator.

The FWHM of all the cases are in Table 1. $\%Abbe = \frac{FWHM_{\text{Abbe}}}{FWHM_{\text{case}}}$ quantifies how close each aberrated PSF is to the diffraction limit.

The reason the other three cases aren't diffraction limited isn't because of a loss of spatial frequencies. It is due to phase on their OTFs. The magnitude and phase of the OTF is shown in Fig. B.16. The Abbe OTF phase is not shown since it is assumed to be flat. Phase on the OTF is associated with lens aberrations or deviations in their spatial profile for the ideal geometry.

The aberrations caused both lenses to have a significantly larger PSF that what is expect from the NA . One may expect that the broader PSFs to smear out the finer features of the SPIFI modulator thus further shortening the time window. Since the size of the diffraction limited PSF and NA are inversely related(Eq. B.19), one could quantify the aberrated PSF as one with reduced NA by

$$NA_{\text{abb}} = \gamma NA \quad (\text{B.79})$$

where γ is the % Abbe number from Table 1. This leads to a modification to Eq. 2.43 to

$$T_m = \frac{2\gamma NA'_{\text{obj}}}{\lambda \kappa} \quad (\text{B.80})$$

Since the paraxial propagator did not produce a the correct PSF, it was not used in any further simulations. The exact propagator $k_{x_{\text{max}}}$ set to .95 was used to perform all following simulations.

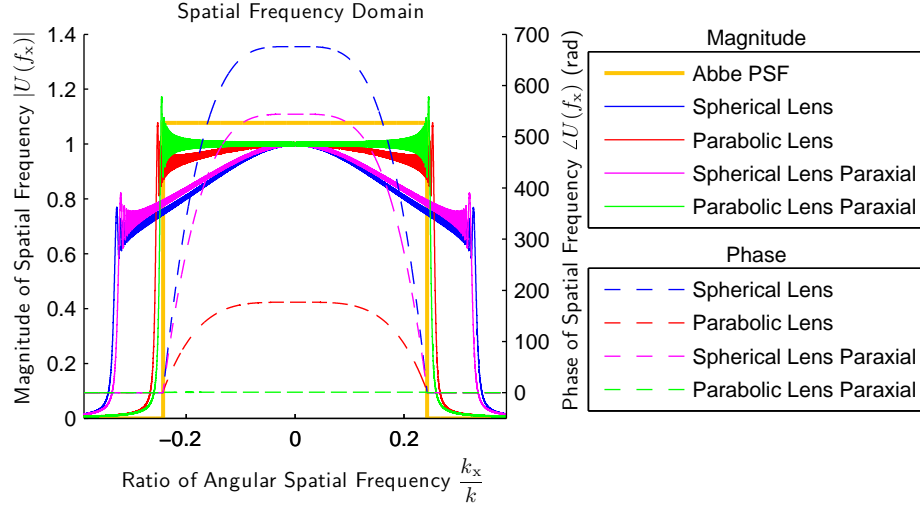


Figure B.16: The magnitude and phase of the of the field spatial frequency distribution at the image plane compared against that of Abbe(Eq. B.22). The spherical(blue) and parabolic(red) lens occupy the spatial frequency bandwidth of Abbe(gold) but have phase on their spatial frequency distributions(blue and red dashed lines). The parabolic lens with the paraxial propagator(green) has the same spatial frequency distribution as Abbe, but flat phase(green dashed line) thus produces a diffraction limited PSF. The spherical lens with the paraxial propagator also shows reduced phase on the OTF(maroon dashed line) but it is still significant.

Next we will investigate if a more ideal spatial lens phase function can be found to bring the PSF to the diffraction limit using the exact propagator.

B.4.2.1 Single Lens Ideal Phase Function

The simulations of the single lens imager with a $f = 25$ (mm), $D = 25.4$ (mm) spherical and parabolic lenses both produced PSFs that are nearly a order of magnitude larger than the diffraction limit. Out of curiosity, we wish to construct a lens phase profile that produces a PSF that reaches the diffraction limit. For the unity magnification condition, the distances from the object to lens planes, and lens plane to image planes are the same, we guess that the ideal lens spatial phase function will have the opposite phase of twice the spatial phase distribution of object point propagated to the lens plane. This lens phase is shown in Fig. B.18 (a) with the accumulated spatial phase of the point source at the lens plane.

This phase was used as the lens function, and the same simulation as that of the previous section was ran with the exact propagator. The PSF generated in the object plane using this lens is shown in FIG B.17 (b) compared against the previous simulation of the spherical lens and parabolic lenses. It is seen that with the "perfect lens" the PSF is the same as that predicted by Abbe, and better than the PSF of the other two lenses.

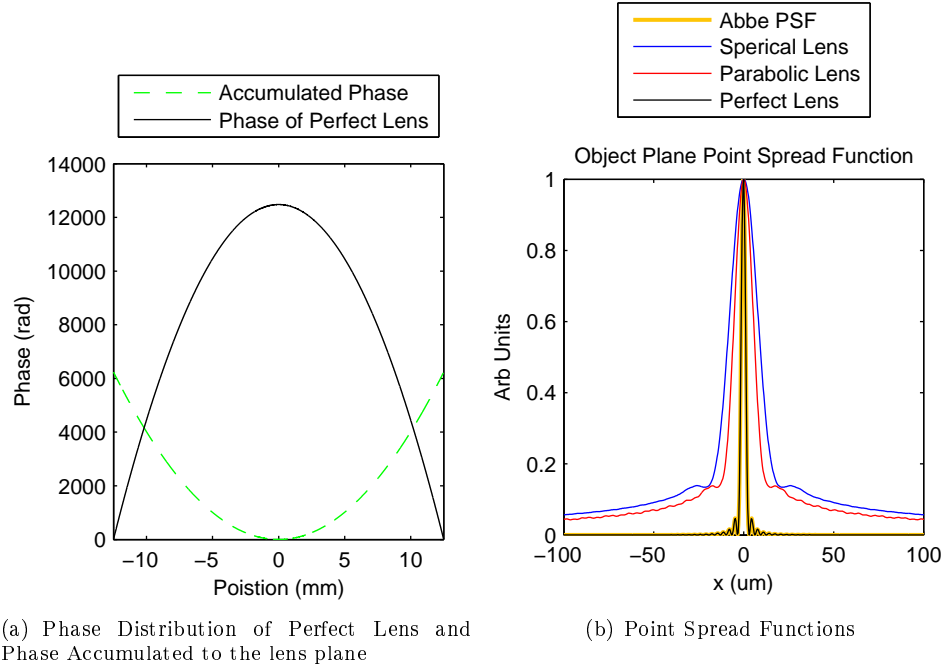


Figure B.17: Phase Distribution for a perfect lens (a). The accumulated phase (green) is in the opposite direction of the perfect lens (black). (b) shows a comparison of PSFs of the perfect lens (black) to the previous ones of the spherical lens (blue) and parabolic lens (red). The PSF of the perfect lens overlaps Abbe PSF (gold).

Seeing that this phase function produced a diffraction limited PSF we which to compare it to the phase function of the parabolic and spherical lenses. The unwrapped phase profiles of the spherical, parabolic, and perfect lenses are shown in Fig. B.18 (a) and the difference in phase between the perfect lens and both spherical and parabolic lenses is shown in Fig. B.18 (b).

In Fig. B.18 (a), we see that the parabolic lens is in closest agreement with the phase function of the ideal lens but is still multiple waves away from the profile of the perfect lens. The difference in phases is shown in Fig. B.18 (b), the parabolic lens seems to suffer from a 4th order error in the phase what the phase of the spherical lens appears to suffer from a mixture of 2nd, 4th and higher orders errors.

Lens designers seek to make lenses that are free of aberrations leading to a diffraction limited PSF and this is a topic beyond the scope of this thesis. This section merely showed how far the aberrations of parabolic and spherical lens deviate from their ideal performance.

B.4.3 Telescope

Image resolution using a parabolic and spherical single lens imager has been shown to be significantly degraded from that predicted by Abbe for the 1-1 imaging condition. We now wish to analyze the

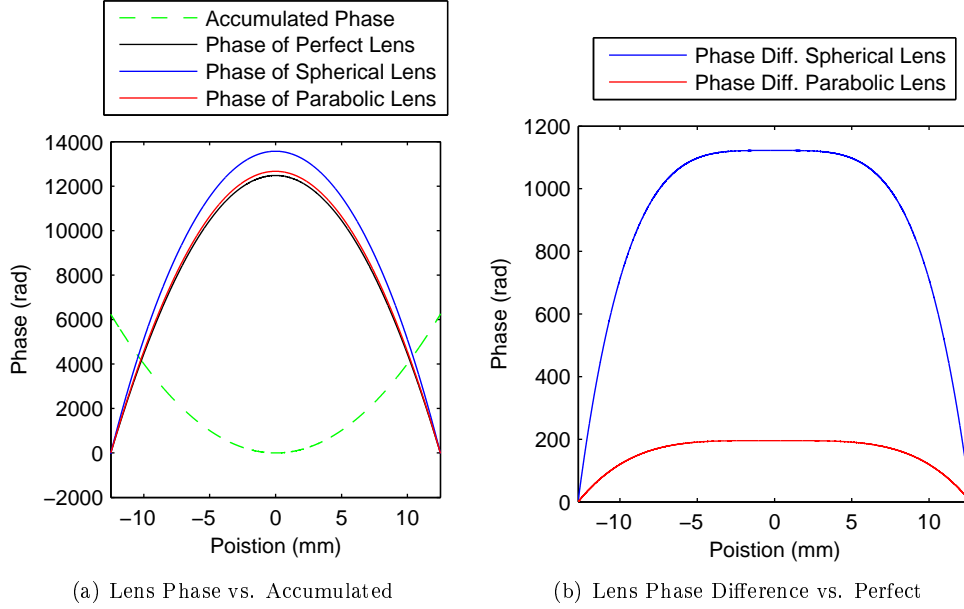


Figure B.18: Lens phase compared against propagated phase and perfect lens phase, (a), and difference between perfect lens, and real lens phases (b)

Method	FWHM	% Abbe
Abbe	1.16 (μm)	-
Spherical Lenses	13.0 (μm)	8.9
Parabolic Lenses	10.9 (μm)	10.6

Table 2: FWHM for Telescope PSF of Fig. B.19 (a)

PSF and OTF of a unity magnification telescope composed of two $f = 25$ (mm), $D = 25.4$ (mm) spherical and parabolic lenses. The PSFs and OTFs of these two telescopes is then compared against that of Abbe(Eq. B.27 , Eq. B.24), determined by the NA of these $\frac{F}{1}$ lenses.

The PSFs and it's OTFs are shown in Fig. B.19. Once again the PSFs are degraded from that predicted by Abbe and the considerations of Sec. B.3.2.

The plot of the OTF, and the phase across it is shown in Fig. B.19 (b). One sees that again the phase profile is not flat for both the spherical and parabolic lens. Unlike in the single lens imager, the bandwidth of the spherical lens is smaller than that of the parabolic lens which nearly matches Abbe in spectral width. The spherical lens telescope also has spatial frequency phase that rolls off slightly earlier than the parabolic lens creating a slightly larger PSF.

Using FWHM the PSFs of the two telescopes are compared against that of Abbe in Table 2, and the PSF of the spherical lens telescope is 11.2 times that off Abbe, and the PSF of the parabolic lens telescope is 9.3 times that of Abbe.

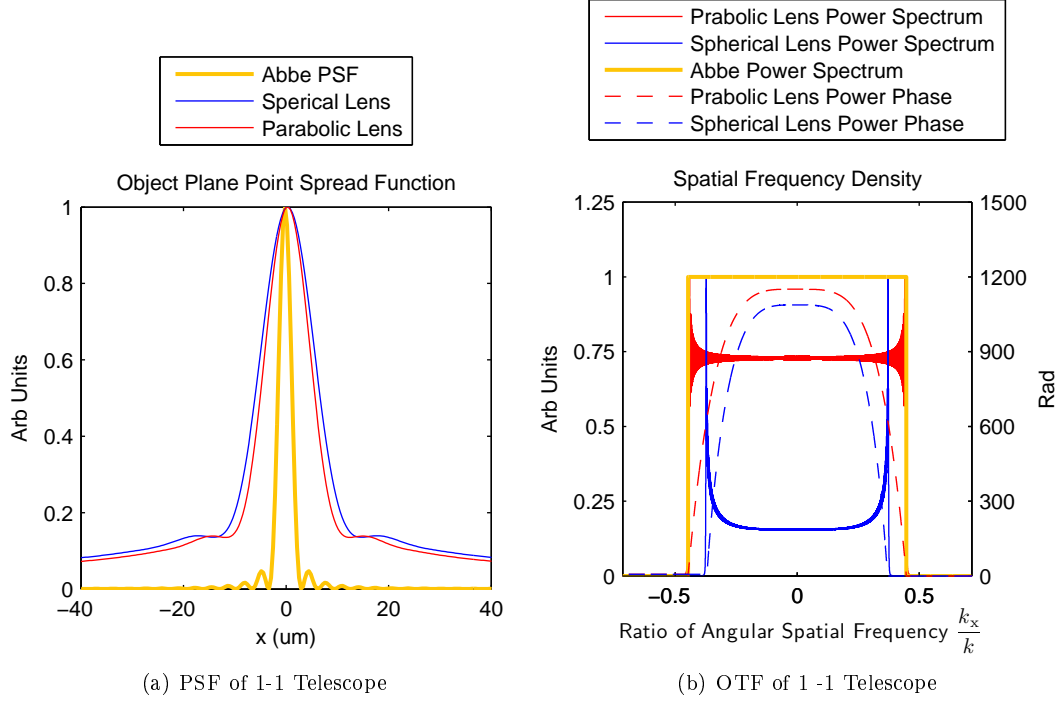


Figure B.19: Simulated PSF (a) and OTF (b) Telescope for a $M = -1$ telescope made of two $f = 25$ (mm), $D = 25.4$ (mm) spherical and parabolic lenses. The PSF of both telescopes is broader than that expected by the PSF expected by the NA (gold) (a). This is due to phase on the telescopes OTFs.

B.4.4 2D Simulations

The 1D simulations of Sec. B.4.2 & Sec. B.4.3, are composed of $N = 2^{22.19} \sim 2^{22}$ points in the transverse spatial extent. A similar 2D simulation, composed of 2^{22} points would have 2^{11} or 2048 points in each direction. Due to the sampling requirements for the exact spatial frequency propagator (Sec. B.4.1), the maximum propagation distance would then be ~ 793 (um). Since this is then the maximum distance between optics, the simulation of the optical system in 2D is impracticable. To have a comparable simulation to the 1D one, a 2D simulation would require 2^{44} or 1.75 trillion points. Assuming the FFT is limiting operation, each 2D FFT requires

$$Op = NM(\log(N \log M)) \quad (\text{B.81})$$

operations [44]. For the 2^{22} points per dimension, for the 2D case 1.88×10^{28} operations are required per FFT. Using double precision floats, the data alone would occupy 140 terabytes. Thus even for reasonable distances, and moderately long near infrared wavelengths, the 2D simulation using Fourier optics methods with the exact propagator is too computationally intensive to be practical, if not currently impossible.

Using the exact propagator, the only place left to stand is exploration the PSF and OTF of single lens and telescope imagers is 1-D simulations.

B.5 Spatial Invariance and Vignetting

Vignetting is the degradation of a image resolution away from the optic axis. Wide-field imaging seeks to accurately reproduce the distribution of the field preserving Eq. B.1 through out the transverse spatial extent. The previous analysis in terms of OTF and PSF assumed spatial shift invariance. In fact only the free space optical propagator is shift invariant(Eq. B.6), real optical systems are not due to the real size of their apertures.

The effect of spatial shift is seen when the object point(Fig. B.14) is transversely displaced. The image point can be simulated easily by adding a linear phase, $e^{jk_x x_0}$, to the object plane spatial frequency distribution before propagation though the system.

An example of simulated vignetted PSFs for a unity magnification spherical single lens($f = 25$ (mm), $D = 25.4$ (mm)) is shown in Fig. B.20. In these simulations, the source point is offset from the optic axis by the distance in the legend and is then imaged by the lens under negative magnification to be on the opposite side of the optical axis. For comparison the transverse offsets in the image plane of Fig. B.20 were then subtracted so the PSFs are centered on each other.

Fig. B.20 (a) shows the PSFs without the axis normalized to itself, the maximums of the PSF falls when it is moved from the optic axis due to a loss of collected power. In Fig. B.20 (b) the PSF is normalized so the shapes can be compared. Not only does the peak power fall but the distribution of the PSFs also broadens with increasing offset. The broadening is not significant with in the first mm but seems to increase rapidly afterwards.

To quantify the vignetting we need a metric of measurement of the PSF to associate the offset with. A first thought is to measure the standard deviation of the PSF as a function of position. This measurement yields a spot size that is much larger than expected due to the broad pedestal on the PSFs(Fig. B.20). Instead FWHM was used. The FWHM doesn't consider the reduction in intensity away from the optic axis.

The FWHM of the PSF as a function of displacement for the $f = 25$ (mm), $D = 25.4$ (mm) spherical single lens 1:1 imager is shown in Fig. B.21 (a). This plot quantifies the overall performance of the system including vignetting. If the inverse of FWHM as a function of displacement would be a point density. The point density per millimeter for the FWHM of Fig. B.21 (a) is shown in Fig. B.21 (b) and falls off away from the optical axis. Fig. B.21 (b) incorporates the considerations or resolution and field of view into one plot of the optical system.

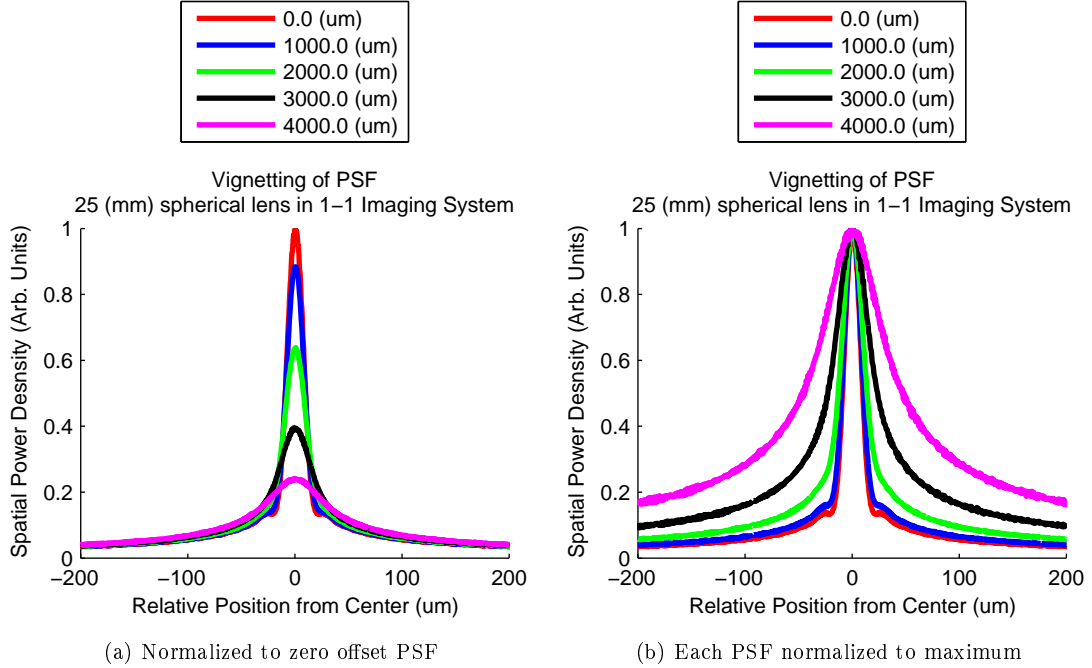


Figure B.20: PSF vignetting of $f = 25$ (mm), $D = 25.4$ (mm) lens. The intensity of the PSF is reduced((a)) and the PSF becomes broader((b)) for increases in the object point offset.

The fall off in number of points can be modeled as a loss of NA away from the optical axis, leading to an additional localized shortening in the time window. This can be incorporated as a spatial fall off in γ from Eq. B.79. Since the FWHM of the PSF of Abbe(Table 1) is twice the Abbe Resolution(Table B.19). One may expect that when the number of points is less than $\frac{\kappa T_m}{4}$ the effective time window of the point becomes shortened. Thus for resolution limited by the SPIFI time window the number of points in the optical system should be greater $\frac{\kappa T_m}{4}$ over the field of view.

Vignetting traces of the types in Fig. B.21 can be used to quantify these optical systems under varying magnification. Plots of the vignetting traces for these imaging systems composed of $f = 25$ (mm), $D = 25.4$ (mm) under for $M = -0.25, -1, \& -4$ are shown in Fig. B.22. Blue lines are traces for systems made using spherical lenses, and the red lines are the systems made using parabolic lenses. The solid lines show the single lens imager and the dashed lines show the telescope.

Under all magnifications the system with the smallest PSF and the largest number of points is always the telecentric one made of parabolic lenses. Also, the spherical lens telescope never outperforms the parabolic single lens, although for unity magnification their performance is nearly equal.

The ripples beginning to appear at the edges of the number of points traces for the two telescopes are due to either the image or object point leaving the diameter of one of the lenses of the telescope.

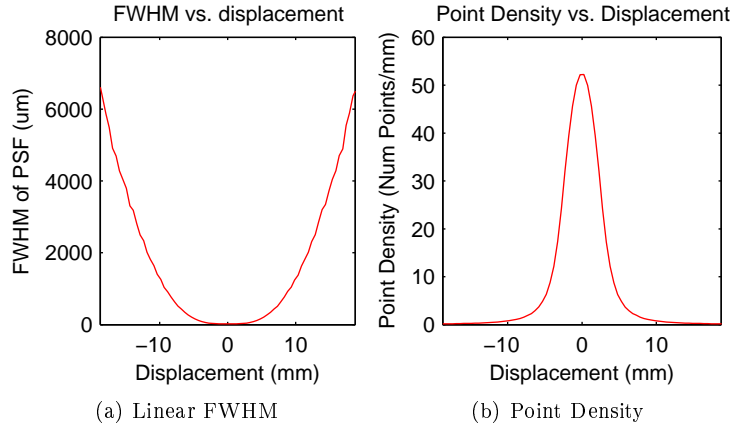


Figure B.21: PSF vignetting over the field of view for a $M = -1$, $f = 25$ (mm), $D = 25.4$ (mm) single lens imager. The FWHM of the PSF is measured as a function of transverse displacement of the object (a). This inverse of this is a point density as a function of position (b).

For example under magnification of 4, the output offset corresponding to the radius of the optics is 12.5 (mm), this corresponds to a input offset of 3.125 (mm). At this point, the output PSF becomes significantly distorted. The same holds for demagnification but on the input side of the telescope. This phenomena isn't seen for the single lens imagers.

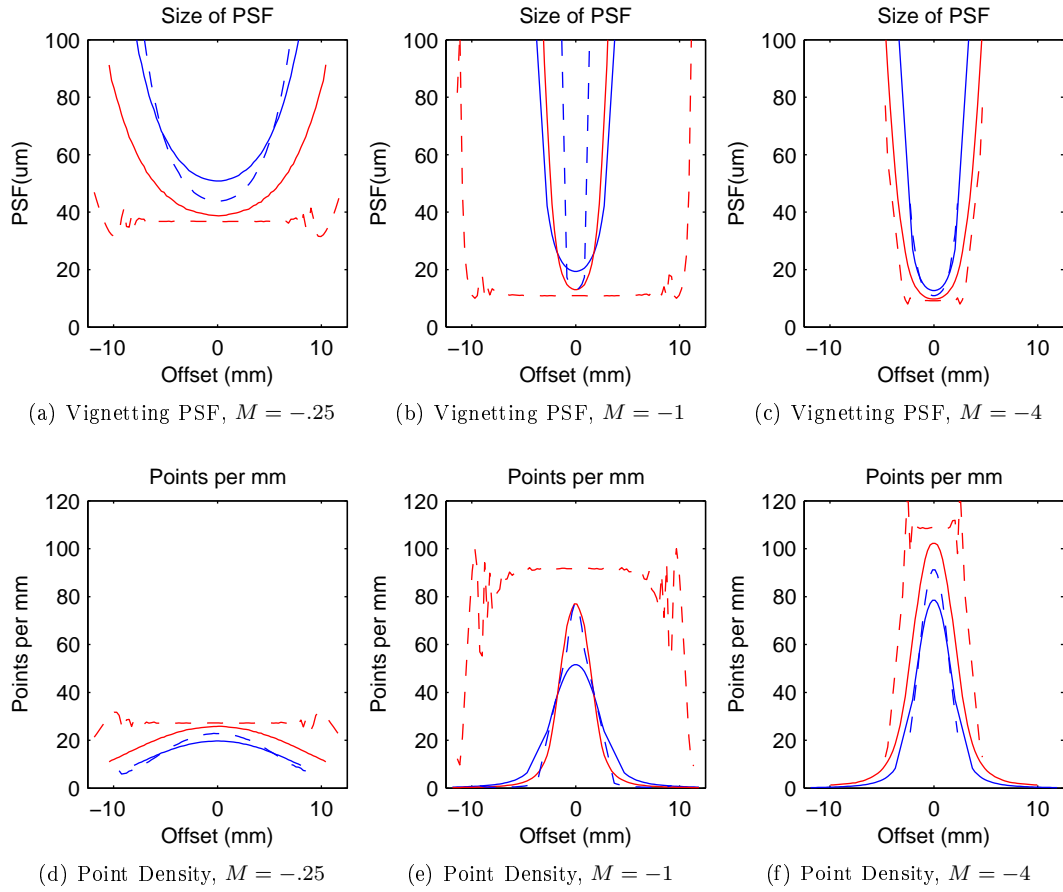


Figure B.22: Comparison of number of points for a spherical and parabolic 25 (mm) focal length, 25 (mm) diameter lens under various magnifications, (red) telescopes, (blue) single lens imager, (solid) spherical lens, (dashed) parabolic lenses

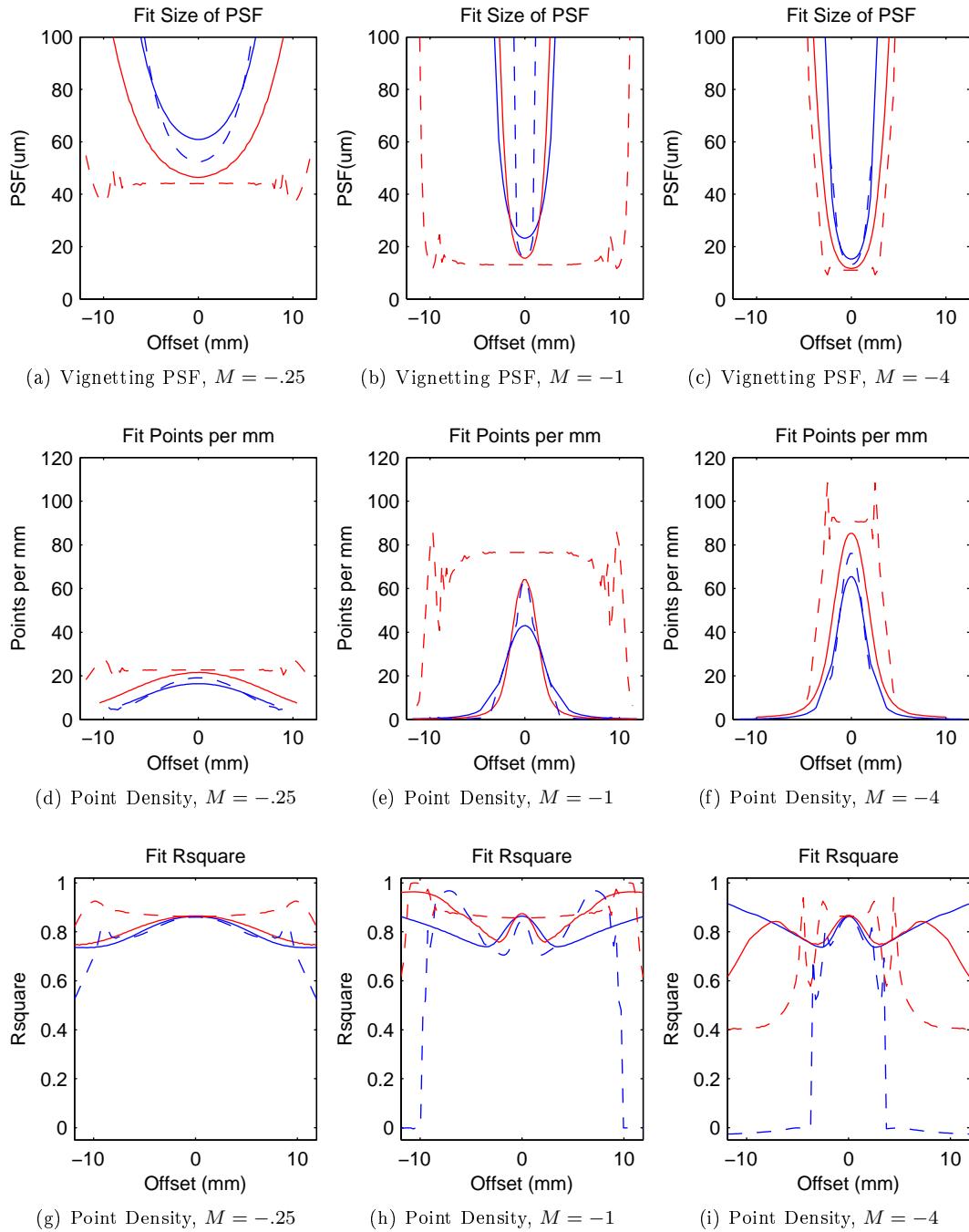


Figure B.23: Using width fit to sinc instead of FWHM. Comparison of number of points for a spherical and parabolic 25 (mm) focal length, 25 (mm) diameter lens under various magnifications, (red) telescopes, (blue) single lens imager, (solid) spherical lens, (dashed) parabolic lenses

APPENDIX C

NUMERICAL SIMULATIONS

This appendix chapter explores parameters of the SPIFI disc modulator and a SPIFI imaging system through numerical simulations. These results have not yet been verified experimentally so this content it has been taken out of the main part of the manuscript.

In the Ch. 2 and analytical model for SPIFI were presented showing how spatial information could be recovered in the FD of the detected electronic signal. Ch. 3 optical limits to the resolution of the electronic image, including NA and aberrations. Demagnifying systems were seen to have lower object plane resolution and over demagnification can limit SPIFI resolution due to a loss in spatial frequencies. Sec. C.1 further develops the limits on SPIFI resolution by numerically propagating the field and summing it's distribution on the detector as a function of time. We wish to see under what total demagnification where the diffraction limited object in the simulation becomes unresolved and compare this to Sec. B.5, using a notch object centered on the axis of the optical system.

C.1 Simulated Optical Limits to SPIFI Number of Points

Appendix B discussed how the numerical aperture and lens aberrations limit the minimum size of the PSF of the optical system. In Sec. B.5, the vignetting of some common optical systems were quantified in terms of a point density as a function of the object points' displacement from the optical axis and is expected to limit the SPIFI resolution for a aberrated system. In this section, the results of similar numerical propagation simulations are presented using the modulated SPIFI illumination field as the input beam to see the effect on the SPIFI resolution limited object with demagnification that exceed this resolution.

Similar to the experiment, the numerical propagation simulations start with a gaussian illumination beam with a beam waist, $w_{0\text{ ill}} = 5(\text{mm})$. The Gaussian beam is centered $x_c = 40(\text{mm})$ from the center of the disc modulator of Ch. 3. The disc modulator is taken to have a $\Delta k = 28(\frac{1}{\text{mm}})$, and spin at $f_0 = 60(\text{rotations} - \text{Hz})$. The modulated field is imaged with a telescope of magnification M_1 to the object plane where a transmission notch object of the form,

$$t_{obj}(x) = 1 - \text{rect}\left(\frac{x}{w_{obj}}\right) \quad (\text{C.1})$$

Parameter	Value
$w_{0 \text{ ill}}$	5 (mm)
x_c	40 (mm)
D	10 (mm)
k_1	0
Δk	28 ($\frac{1}{\text{mm}}$)
f_0	60 (Hz)

Table 3: Modulation Parameters

masks the beam. This produces a object field with example shown in Fig. C.1 that is then imaged to the detector. The detector is taken to have width $D = 10$ (mm), and integrates the field's intensity over it's area creating a output signal. The simulation parameters are summarized in Table 3.

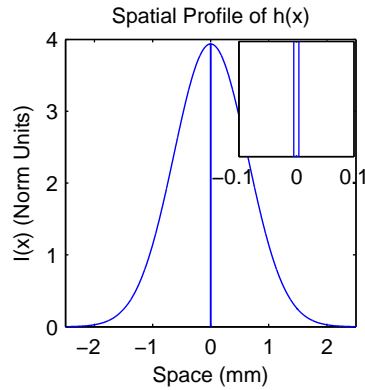


Figure C.1: Spatial distribution of field for simulations

The field distribution is numerically calculated at the detector for 5600 time domain points, over the time duration $T = \frac{1}{f_0}$. The time separation between the points, dt , was set to five times the center frequency of the first harmonic in the trace, $\frac{1}{dt} = 5 * f_0 * \Delta k * x_0$.

The field distribution on the detector for each time domain point was found with two methods, numerically propagating the field distribution from the modulator to object plane and detector, and by scaling the field distributions at the modulator and object planes by the optical magnification, the terms under the integral in Eq. A.9. The second method of scaling the field distributions by the magnifications doesn't model the effects of optical diffraction or aberrations.

From the vignetting graphs of Sec. B.5, telescopes have a higher number of points under all circumstances. Since spherical lenses are widely available, the imaging systems used for the simulations were telescopes composed of spherical lenses, with lens focal length selected to get various magnifications. The spherical lens function corresponding to ThorLabs BK7 Bi-Convex lenses of

diameter 25.4 (mm) were used for the focal lengths considered.

In all cases the size of the object, w_{obj} , from Eq. C.1, was also set to the SPIFI resolution limit, $w_{obj} = \frac{M_1}{\Delta k}$. The FD traces from some of the configurations are shown in Fig. C.2, and the time domain signal associated with these traces is shown in Fig. C.3. The green line in the TD traces is the envelop of the intensity of the spatial frequency distribution, $\mathcal{G}'(f_x = f_0 \Delta k M_1^{-1} M_2^{-1} t)$ from Eq. A.13.

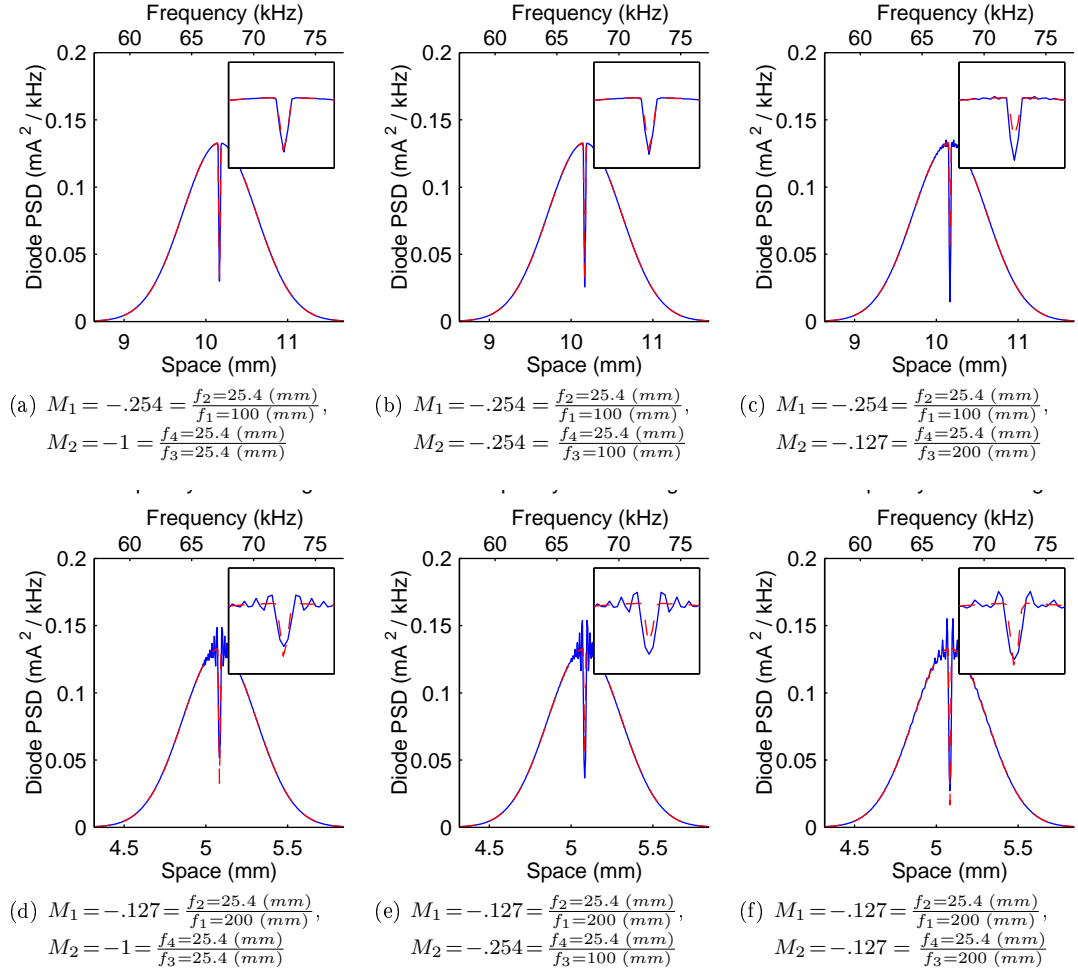


Figure C.2: Simulation of FD signal for varying optical relay systems. (Blue) Traces are found by propagating the field through the optical system. (Red) is found without propagation from the perfectly magnified signal at the detector plane.

Fig. C.2 (a) & (b) show a FD profile that is very similar between the simulations ran with and without propagation. For Fig. C.2 (a) this isn't surprising since, the $\Delta k = 28 \left(\frac{1}{mm}\right)$ would have a maximum periodicity of 14 lines per millimeter, and this is higher than the point density of Fig. B.22 (d), the first optical system should be able to reproduce this field at the object plane. The 14

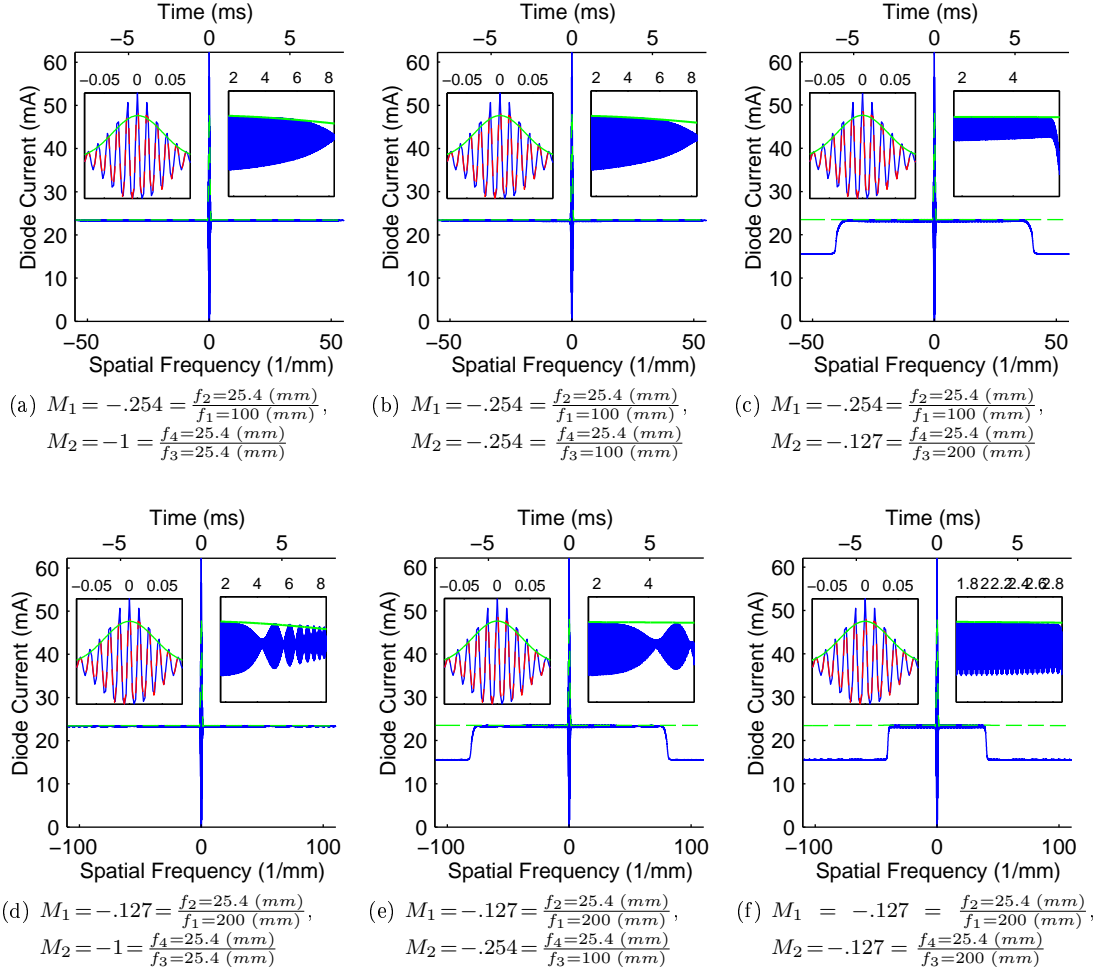


Figure C.3: Simulation of TD signal for varying optical relay systems. (Blue) Traces are found by propagations the field through the optical system. (Red) is found without propagation from the perfectly magnified signal at the detector plane. (Green) is the ideal envelope of the TD signal from the field's intensity spatial frequency distribution of the field.

lines per millimeter is demagnified by the 4 : 1 telescope to 56 lines per millimeter, which again is lower than the maximum point density supported by the 1:1 telescope, Fig. B.22 (e), used to relay it to the image plane.

What is unexpected is that for the simulations of Fig. C.2 (b) is also well resolved on the detector, in a manner very similar to without propagation. The vignetting simulations indicated that the 56 line per millimeter mask will not be well relayed to the detector plane since the maximum point density of Fig. B.22 (d) is a little more than 21 points per millimeter. It seems as if the aberrations of the second imaging system have little effect on the resolved image.

In Fig. C.2, (d), the demagnification of the first telescope is changed to $\sim 8:1$, for the propagation simulation ripple appears near the object in the pass band. This ripple is not present in the simulation

that doesn't perform numerical propagation. The cause of the ripple is not the temporal window function, since the FD plots of Fig. C.2, have had a hamming window applied in the time domain before transforming, further discussed in Sec. 2.7. From Fig. C.2, (d), the cause of the ripple from the appears unclear. The time domain plot Fig. C.3 (d) is revealing.

The envelope of Fig. C.3 (d) should follow the intensity's spatial frequency distribution, $\mathcal{G}'(f_x = f_0\Delta kM_1^{-1}M_2^{-1}t)$, shown in green. For lower spatial frequencies, top left inset of Fig. C.3 (d), this is indeed the case, but as the spatial frequencies increase, shown zoomed in the top right inset of Fig. C.3 (d), the envelope of the propagated signal appears to have acquired ripple. It is as if there is an additional function modulating \mathcal{G}' such that

$$\mathcal{G}''(f_x) = M_{sys}(f_x)\mathcal{G}'(f_x) \quad (\text{C.2})$$

, where M_{sys} is this modulating function. M_{sys} is likely related to the optical transfer function of the system. It's profile is causing the distortion, and is likely due to spherical abberations from the lenses.

Increased ripple is also seen in Fig. C.2, (c), (e), (f) and but here the cause is not lens abberations but the numerical apertures of the second relay system. From the periodicity of the modulator, Δk , and the magnification of the first optical system, M_1 , the maximum spatial frequencies at the object plane sweep over $\pm \frac{\Delta k}{2M_1}$, as shown in Fig. B.2, and from Eq. B.8, when the spatial frequency exceeds that of the aperture it is lost. This occurs when

$$2\pi f_0\Delta kM_1^{-1}t = k \frac{R}{\sqrt{f^2 + R^2}} \quad (\text{C.3})$$

For the parameters of Fig. C.2, (e), this would occur at $t = \pm 6.14$ (ms), and for Fig. C.2, (f), $t = \pm 3.09$ (ms) in agreeance with the fall off in the signal intensity seen in the figures at those time points.

C.2 Effects of Binary Printing

To avoid dithering in the printing of the modulator, the pattern of the modulator was such that

$$m(R, \theta) = \frac{1}{2} + \frac{1}{2}\text{sgn}[\cos[(k_0 + \Delta kR)\theta]] \quad (\text{C.4})$$

the difference in the mask for $t = \frac{1}{2T_m}$ is shown in Fig. C.4.

The goal of this section is to explore the effect of binary printing on the SPIFI electronic signal. The binary printing generates higher harmonic terms then the cosine modulation. To see the effect of

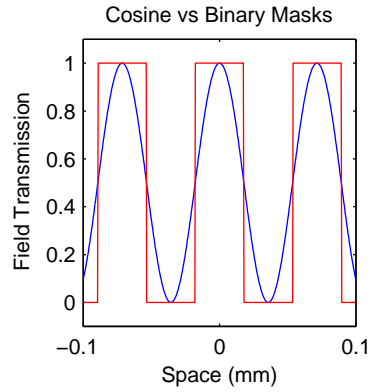


Figure C.4: Binary(red) vs. Normal(blue) Masks

the binary printing the time domain signal will be simulated with and without numerical propagation, the simulated outputs will be superimposed onto the traces of Fig. C.2. If the binary printing does little to the output one would expect that the traces should overlap those of Fig. C.2. Diffraction will also have an effect with binary printing just as it did with the cosine simulations in Sec. B.

APPENDIX D

EXTENDED BACKGROUND INFORMATION

The human eye has been used as the detection back end of optical systems for centuries. It was the invention of the photograph in the 19th century provided us with a new detector. The photograph originally used silver salts on a hard plate. Later, methods of manufacturing film on flexible acetate and cellulose substrates were invented.

Today, camera film has been replaced with CCDs, and CMOS arrays. High speed array detectors do also exist but at cost. Other optical imaging modalities that do not use an array detector exist. The most notable of these methods is scanning confocal microscopy. Spatial information in these systems is time multiplexed onto a single detector. The single detectors often used in scanning microscopy are photo-multiplier tubes, and avalanche photo diodes offering high sensitivities. Single detection is natural in scanning systems since light must pass through a common pinhole to perform optical sectioning.

D.1 High speed imaging

High speed imaging's ability to capture dynamics has been of great scientific interest since the demonstration of strobe photography by Muybridge and Stanford in 1873 [45]. Stanford, the former governor of California, recruited Muybridge, a photographer of note of his time, to prove that a horse's feet leave the ground when it gallops. Fig. [Scan Figure] shows the definitive results of Muybridge's work.

Early high speed cinematography used sparks to supply the radiation needed to expose the film. In the 1930s Dr. Edgerton developed sealed gas electronic discharge flash lamps. The discharge in these lamps took place in krypton, argon, or xenon gas improving the luminous efficiency of the source. [45] Dr. Edgerton and his company E. G. & G were able to develop flash lamps with light durations as short as 1-10 (μ s), which were short enough for front lit high velocity projectile work. [45] These experiments used a trigger to fire a strobe light after some delay.

Many dynamical processes of interest cannot be synchronized this way. Consequently, a significant effort has been mounted to develop imaging technologies that acquire images at high frame rates. The bulk of this effort has been devoted to charge coupled devices (CCD) and complementary

metal-oxide semiconductor(CMOS) technologies. CCD and CMOS detectors are multi element, and can be produced on chips with high bandwidth and low noise electronics to read out the detected signal. As chips, they devices are mostly manufactured in mature silicon processes, limiting spectral range to between 400-1100 nm.

D.1.1 Applications Requiring High speed Imaging

Interest in high speed imaging has increased significantly since early pioneering work, making high speed cameras indispensable tools in many scientific and industrial applications.

On the industrial and military side, many applications are pursued. In the automotive industry high speed imaging is used for air bag deployment, rollover, and restraint, and hi-G crash testing. In addition, high speed imaging is used for combustion testing, and to help improve engine efficiency. [46, 47, 48] Defense applications include ballistics [49], detonics [50], impact tests [51, 52], and testing turbine engines [53]. There are numerous other applications including non-destructive testing [54], particle image velocimetry [55], crack propagation [56], and ink jet sprays, [57].

Fluid dynamics can be investigated with high speed imaging, showing droplet and bubble formation [58, 59], flow in microfluidic channels [60], wake field dynamics [61], and other effects. Limitations of image speed can prevent detailed imaging of droplet formation, which can last only $100\mu S$. [62] MEMS devices and microactuator dynamics can be visualized [63, 64]. In this area, there is a need to study dynamics with frame rates up 1 million frames per second(FPS).

Numerous medical and biomedical applications also require high speed imaging capabilities. These include studies of biomechanics [65], diagnosis of vocal cord disorders [66], muscle contraction dynamics [67], comparative physiology [68], blood flow [69, 70, 71, 72], cardiac fluid flow and forces [73, 74], and high speed neuron dynamics [75, 76, 77, 78, 79, 80, 81, 53, 82, 83, 84, 85, 86].

The applications cited above are an incomplete listing of the applications employing high speed imaging. The list will be greatly expanded if the imaging speed can be increased particularly if costs are reduced and if techniques of high speed imaging can be expanded beyond areas where high speed silicon-based CCD and CMOS chips are currently used.

High speed imaging can be broadly classified into imaging techniques using fast segmented detectors like CCD and CMOS or fast time domain(TD) scanning systems for confocal or laser scanning microscopy.

D.2 CMOS and CCD Imagers

Since [13] described the CCD device in 1970, and [14] verified that it works, the CCD has been the dominate electronic imager. The CCD could be said to be invented by accident. Boyle and Amelio by were in search of a new bubble array memory and ended up developing a light sensitive detector. Boyle and Amelio were awarded the nobel prize in physics in 2009 for the invention of the CCD owing the key to it's success being the CCDs simplicity. [87]

Metal Oxide Semiconductors(MOS) imager had been developed starting in 1960. However CCDs became dominate over them since their invention in 1970 due to their relative freedom from fixed pattern noise(FPN). [88] Development of CCD imagers continues constantly pushing the limits on sensitivity and speed. [89] has published results of a custom developed 512x512 pixel CCD with 2 million frame per second capture rats. At the time of publication they claim this to be the "largest and fastest back-illuminated CCD in the world" - [89]

After the invention of the CCD, development of MOS imagers slowed significantly. Most reports in the 1970s and 1980s compared performance parameters of MOS imagers unfavorably to CCD detectors. [90] In the 1990s MOS imagers came roaring back. This was due to the desire for low power and low cost single chip imaging systems and the achievements in the development of CMOS process technology. [88]

CMOS technology allows more transistors and memory to be integrated on chip close to the pixels. Most imagers suffer from a read out bottleneck of the need to multiplex 2D data into a single analog to digital converter [91]. To overcome this limitation, [92] produced a CMOS device and individual analog to digital converter(A/D) and memory per pixel to make it capable of massively parallel readout. Their 352x238 pixels was capable of frame rates up to 10,000 frames per second. Pushing parallel readout, [91] has proposed a 32x32 pixel design that can read at 1.25 billion frames per second. CMOS has seen rapid development recently due to costs, but even [93] in his review of CMOS sensors, admits that CCDs are still produce higher quality still images.

Recent advances in highly optimized CCD and CMOS imaging technologies has been tremendous and segmented detector architectures have been optimized for either speed or sensitivity depending on the application. High speed CMOS and CCD Imagers have achieved remarkable imaging frame rates. However, the speed comes at great expense, and costs increase rapidly for more complex high speed imaging cameras. Many sensors cited in this section are not even commercially available. More importantly, these speeds are restricted to wavelengths in the bands that silicon is a effective optical detector. Generally, this is from 400 to 1100 nm. For wavelengths with a photon energy

bellow the bandgap of silicon, many advances in segmented high speed cameras do not apply.

D.3 Reticle Imaging

The FM Reticle was first invented by [23]. This mask was first used to map the position of a point on the reticle into a frequency domain signal, and was used for target tracking. [94] describes methods how varying the parameters that define the spatial pattern of the reticle, allows 2D information of a point object through the frequency and phase of the output signal. Such a method isn't directly expandable into 2D wide-field imaging.

[25] first described modifying the reticle pattern of [23] making it symmetric to perform wide-field imaging. The reticle allows for a dimensional reduction of the detector array, and [25] used a scanning mirror to multiplex the second dimension of their images. [25] showed experimentally that their reticle would allow for the recovery of 2D information, they did not present the overall imaging theory containing the number of points and image resolution that is presented here.

D.4 High Speed Scanning Microscopy

The most common optical sectioning microscope is the point scanning confocal microscope, a field know as confocal microscopy. In confocal microscopy, out of focus light is rejected from the detector using a pinhole causing increased localization in the z direction of the image. Initial implementations of confocal microscopy were slow due to requirement of scanning the pinhole. Increased speeds in confocal microscopy have been obtained using a disc architecture. High-speed confocal microscopy at 1,000 (FPS) has been achieved using a microlens array disk in a pinhole array. [95] Spinning disk confocal microcopy has been optimized for higher speeds with, 3D image stacks formed with 30 layers at a rate of 30 stacks per second. [96] High speed confocal microscopes are used for imaging velocity profiles in microfluidic structures [97], and for functional cell imaging [75].

D.5 Structured Illumination Microscopy

Confocal microscopy performs optical sectioning using a pinhole. Structured illumination microscopy(SIM) reproachers this problem by modulating the illumination beam. In SIM, illumination masks are imaged onto the transmission or reflectance of an object, and then captured with a CCD. From captured images, and knowledge of the masks optical sections mathematical formula exist to recover the optical section. [98].

Taking advantage of the downmixing effect of spatial frequencies, Moiré Fringes , [99,100] demonstrated the use of SIM to beat the diffraction limit by a factor of two. [101] showed that coupled

with non-linear harmonics, structured illumination could have theoretically unlimited resolution. The unlimited resolution analysis does not take noise, and eventually harmonic strength will fall below the noise floor limiting resolution.

REFERENCES

- [1] G. Cox, *Optical Imaging Techniques in Cell Biology*, 1st ed. CRC Press, Nov. 2006.
- [2] R. Hooke, *Micrographia, or, Some physiological descriptions of minute bodies made by magnifying glasses, with observations and inquiries thereupon: by Robert Hooke ; with a preface by R.T. Gunther*. J. Martyn and J. Allestry, 1665. [Online]. Available: <http://www.gutenberg.org/files/15491/15491-h/15491-h.htm>
- [3] L. Daguerre, *History and Practice of the Photogenic Drawing on the True Principles of the Daguerreotype with the New Method of Dioramic Painting*. London: Stewart and Murray, 1839, translated by: J.S. Memes. [Online]. Available: <http://books.google.com/books?id=gnUEAAAQAAJ&dq=A%20practical%20description%20of%20that%20process%20called%20the%20daguerreotype&pg=PP9#v=onepage&q&f=false>
- [4] H. Talbot, "Some account of the art of photogenic drawing," *The London and Edinburgh Philosophical Magazine and Journal of Science*, vol. 14, pp. 196–208, 1839. [Online]. Available: <http://books.google.com/books?id=U8M-AAAAYAAJ&dq=London%20and%20Edinburgh%20Philosophical%20Magazine%20and%20Journal%20of%20Science%20volume%2014&pg=PA196#v=onepage&q&f=false>
- [5] "Photogenic drawing, or dawing by the agency of light," *The Edinburgh Review or Critical Journal*, vol. 76, pp. 309–344, Jan. 1843. [Online]. Available: <http://books.google.com/books?id=nTobAAAAYAAJ&dq=On%20the%20Chemical%20Action%20of%20the%20Rays%20of%20the%20Solar%20Spectrum%20on%20Preparations%20of%20Silver%20and%20Other%20Substances%2C%20Both%20Metallic%20and%20Non-Metallic%2C%20and%20on%20Some%20Photographic%20Processes&pg=PA309#v=onepage&q&f=false>
- [6] J. F. W. Herschel, "On the chemical action of the rays of the solar spectrum on preparations of silver and other substances, both metallic and Non-Metallic, and on some photographic processes," *Philosophical Transactions of the Royal Society of London*, vol. 130, pp. 1–59, Feb. 1840, ArticleType: research-article / Full publication date: 1840 / Copyright © 1840 The Royal Society. [Online]. Available: <http://www.jstor.org/stable/108209>
- [7] H. Hertz, "Ueber einen einfluss des ultravioletten lichtetes auf die electriche entladung," *Annalen der Physik und Chemie*, vol. 31, no. 8b, pp. 983–1000, May 1887. [Online]. Available: <http://books.google.com/books?id=79SWAAAIAAJ&dq=Annalen%20der%20Physik%20und%20Chemie%20hertz%201887&pg=PA983#v=onepage&q&f=false>
- [8] L. Austin and H. Starke, "Ueber die reflexion der kathodenstrahlen und eine damit verbundene neue erscheinung secundärer emission," *Annalen der Physik*, vol. 314, no. 10, pp. 271–292, 1902. [Online]. Available: <http://onlinelibrary.wiley.com/doi/10.1002/andp.19023141003/abstract>
- [9] H. Iams and B. Salzberg, "The secondary emission phototube," *Proceedings of the Institute of Radio Engineers*, vol. 23, no. 1, pp. 55–64, 1935. [Online]. Available: http://ieeexplore.ieee.org/xpls/abs_all.jsp?arnumber=1685754&tag=1
- [10] Z. Vladimir, "Method of and apparatus for producing images of objects," Haddonfield, NJ, Nov. 1935, undefinedFiling Date: Nov 13, 1931. [Online]. Available: <http://www.google.com/patents?id=ugN-AAAEEBAJ>
- [11] M. Faraday, "Experimental researches in electricity. fourth series," *Philosophical Transactions of the Royal Society of London*, vol. 123, pp. 507–522, Jan. 1833. [Online]. Available: <http://www.jstor.org/stable/108004>

- [12] R. F. Pierret, *Semiconductor Device Fundamentals*, 2nd ed. Addison Wesley, Apr. 1996.
- [13] W. Boyle and G. Smith, "Charge coupled semiconductor devices," *BELL SYSTEM TECHNICAL JOURNAL*, vol. 49, no. 4, pp. 587–593, Apr. 1970.
- [14] G. Amelio, M. Tompsett, and G. Smith, "Experimental verification of the charge coupled device concept," *BELL SYSTEM TECHNICAL JOURNAL*, vol. 49, no. 4, p. 593–600, Apr. 1970.
- [15] D. Burrows, R. Dennis, K. Patnaude, A. Reisinger, M. Sundaram, H. S. Kim, E. Plis, J. B. Rodriguez, G. D. Bishop, Y. D. Sharma, L. R. Dawson, S. Krishna, J. Bundas, and R. Cook, "Mid-IR focal plane array based on type-II InAs/GaSb strain layer superlattice detector with nBn design," *Applied Physics Letters*, vol. 92, no. 18, p. 183502–3, May 2008. [Online]. Available: <http://link.aip.org/link/?APL/92/183502/1>
- [16] S. D. Gunapala, S. V. Bandara, J. K. Liu, C. J. Hill, S. B. Rafol, J. M. Mumolo, J. T. Trinh, M. Z. Tidrow, and P. D. LeVan, "1024 x 1024 pixel mid-wavelength and long-wavelength infrared QWIP focal plane arrays for imaging applications," *Semiconductor Science and Technology*, vol. 20, no. 5, p. 473–480, 2005. [Online]. Available: <http://www.iop.org/EJ/abstract/0268-1242/20/5/026>
- [17] E. Ojefors, U. Pfeiffer, A. Lisauskas, and H. Roskos, "A 0.65 THz Focal-Plane array in a Quarter-Micron CMOS process technology," *Solid-State Circuits, IEEE Journal of*, vol. 44, no. 7, pp. 1968–1976, 2009. [Online]. Available: http://ieeexplore.ieee.org/xpls/abs_all.jsp?arnumber=5109781
- [18] P. Goldsmith, C. Hsieh, G. Huguenin, J. Kapitzky, and E. Moore, "Focal plane imaging systems for millimeter wavelengths," *Microwave Theory and Techniques, IEEE Transactions on*, vol. 41, no. 10, pp. 1664–1675, 1993. [Online]. Available: http://ieeexplore.ieee.org/xpls/abs_all.jsp?arnumber=247910
- [19] D. Sheen, D. McMakin, and T. Hall, "Three-dimensional millimeter-wave imaging for concealed weapon detection," *Microwave Theory and Techniques, IEEE Transactions on*, vol. 49, no. 9, pp. 1581–1592, 2001. [Online]. Available: http://ieeexplore.ieee.org/xpls/abs_all.jsp?arnumber=942570&tag=1
- [20] S. W. Paddock, "Principles and practices of laser scanning confocal microscopy," *Molecular Biotechnology*, vol. 16, no. 2, pp. 127–150, 2000. [Online]. Available: <http://www.springerlink.com/content/f7wxt278n6n551x0/>
- [21] M. Minsky, "Microscopy apparatus," Cambridge, Mass., p. 3, Dec. 1961, undefined-Filing Date: Nov 7, 1957. [Online]. Available: <http://www.google.com/patents?id=G01yAAAEBAJ&zoom=4&pg=PA2#v=onepage&q&f=false>
- [22] W. B. Amos and J. G. White, "How the confocal laser scanning microscope entered biological research," *Biology of the Cell*, vol. 95, no. 6, p. 335–342, 2003. [Online]. Available: <http://www.biocell.org/boc/095/0335/boc0950335.pdf>
- [23] D. Lovell, "ELECTRO-OPTICAL POSITION INDICATOR," South Bend, Indiana, Aug. 1961, undefined-Filing Date: Aug 3, 1959. [Online]. Available: <http://www.google.com/patents?hl=en&lr=&vid=USPAT2997699&id=rMNuAAAEBAJ&oi=fnd&dq=Electro-Optical+Position+Indicator+System&printsec=abstract>
- [24] Z. W. Chao and J. L. Chu, "General analysis of frequency-modulation reticles," *Optical Engineering*, vol. 27, p. 440–442, 1988.
- [25] J. S. Sanders, R. G. Driggers, C. E. Halford, and S. T. Griffin, "Imaging with frequency-modulated reticles," *Optical Engineering*, vol. 30, no. 11, p. 1720–1724, 1991.

- [26] Wikipedia, “CD-ROM,” Mar. 2011. [Online]. Available: <http://en.wikipedia.org/w/index.php?title=CD-ROM&oldid=41777898>
- [27] “Newegg.com - ASUS beige 52X CD-ROM E-IDE/ATAPI CD-ROM drive model CD-S520/A5,” <http://www.newegg.com/Product/Product.aspx?Item=N82E16827134013>, 2011. [Online]. Available: <http://www.newegg.com/Product/Product.aspx?Item=N82E16827134013>
- [28] S. Lee, J. Kim, and S. Kim, “Critical and flutter speeds of optical disks,” *Microsystem Technologies*, vol. 8, no. 2-3, pp. 206–211, 2002. [Online]. Available: <http://www.springerlink.com/content/ht0klf65mnb2711f/>
- [29] N. Kang and A. Raman, “Vibrations and stability of a flexible disk rotating in a gas-filled enclosure—Part 2: Experimental study,” *Journal of Sound and Vibration*, vol. 296, no. 4-5, pp. 676–689, Oct. 2006. [Online]. Available: <http://www.sciencedirect.com/science/article/B6WM3-4K7NHN5-1/2/c150b449de18baee90ce7b24c7bea6f7>
- [30] P. Rees, “MythBusters: cell phone destroys gas station,” Sep. 2003. [Online]. Available: http://www.amazon.com/Cell-Phone-Destroys-Gas-Station/dp/B000IT7O5C/ref=pd_vodsm_B000IT7O5C
- [31] E. Abbe, “The relation of aperture and power in the microscope (continued).” *Journal of the Royal Microscopical Society*, vol. 2, no. 1, p. 460–473, Jun. 1882. [Online]. Available: <http://books.google.com/books?id=4r4EAAAAQAAJ&dq=Journal%20of%20the%20Royal%20Microscopical%20Society%20%201881&pg=PA460#v=onepage&q&f=false>
- [32] —, “On the estimation of aperture in the microscope,” *Journal of the Royal Microscopical Society*, vol. 1, no. 1, p. 388–423, Mar. 1881. [Online]. Available: <http://books.google.com/books?id=xe4BAAAAYAAJ&dq=Journal%20of%20the%20Royal%20Microscopical%20Society%20Abbe%20On%20the%20Function%20of%20Aperture&pg=PA388#v=onepage&q&f=false>
- [33] J. W. Goodman, *Introduction to Fourier optics*. Roberts and Company Publishers, 2005.
- [34] M. Corp., “Application note 728 - defining and testing dyanamic parameters of High-Speed ADCs, part 1,” <http://www.maxim-ic.com/app-notes/index.mvp/id/728>, Feb. 2001. [Online]. Available: <http://www.maxim-ic.com/app-notes/index.mvp/id/728>
- [35] “Thorlabs.com - large diameter precision polished aspheres,” http://www.thorlabs.com/NewGroupPage9.cfm?ObjectGroup_ID=2736. [Online]. Available: http://www.thorlabs.com/NewGroupPage9.cfm?ObjectGroup_ID=2736
- [36] P. Siegel, “Terahertz technology,” *Microwave Theory and Techniques, IEEE Transactions on*, vol. 50, no. 3, pp. 910–928, 2002. [Online]. Available: http://ieeexplore.ieee.org/xpls/abs_all.jsp?arnumber=989974&tag=1
- [37] A. W. M. Lee, Q. Qin, S. Kumar, B. S. Williams, Q. Hu, and J. L. Reno, “Real-time terahertz imaging over a standoff distance (>25 meters),” *Applied Physics Letters*, vol. 89, no. 14, p. 141125, 2006. [Online]. Available: <http://link.aip.org/link/APPLAB/v89/i14/p141125/s1&Agg=doi>
- [38] W. L. Chan, K. Charan, D. Takhar, K. F. Kelly, R. G. Baraniuk, and D. M. Mittleman, “A single-pixel terahertz imaging system based on compressed sensing,” *Applied Physics Letters*, vol. 93, no. 12, p. 121105, 2008. [Online]. Available: <http://link.aip.org/link/APPLAB/v93/i12/p121105/s1&Agg=doi>
- [39] C. Ling, J. Landry, H. Davee, G. Chin, and G. Rebeiz, “Large area bolometers for THz power measurements,” *Microwave Theory and Techniques, IEEE Transactions on*, vol. 42, no. 4, pp. 758–760, 1994. [Online]. Available: http://ieeexplore.ieee.org/xpls/abs_all.jsp?arnumber=285093

- [40] R. F. Fischer and B. Tadic, *Optical System Design*, 1st ed. McGraw-Hill Professional, Jun. 2000.
- [41] “ZEMAX: software for optical system design.” <http://www.zemax.com/>, 2011. [Online]. Available: <http://www.zemax.com/>
- [42] S. M. Barnett, “Resolution of the Abraham-Minkowski dilemma,” *Physical Review Letters*, vol. 104, no. 7, p. 070401, Feb. 2010. [Online]. Available: <http://link.aps.org/doi/10.1103/PhysRevLett.104.070401>
- [43] H. Helmholtz, “On the limits of the optical capacity of the microscope,” *The Monthly microscopical journal*, vol. 16, pp. 15–39, 1876. [Online]. Available: <http://books.google.com/books?id=-DE4AAAAMAAJ&dq=optics%20limit%20abbe%20frripp&pg=PA15#v=onepage&q&f=false>
- [44] K. Moreland and E. Angel, “The FFT on a GPU,” in *Proceedings of the ACM SIGGRAPH/EUROGRAPHICS conference on Graphics hardware*. San Diego, California: Eurographics Association, 2003, p. 112–119. [Online]. Available: <http://portal.acm.org/citation.cfm?id=844191>
- [45] J. C. Russ, *The Image Processing Handbook, Third Edition*, 3rd ed. CRC Press, Oct. 1998.
- [46] J. Hult, M. Richter, J. Nygren, M. Alden, A. Hultqvist, M. Christensen, and B. Johansson, “Application of a high-repetition-rate laser diagnostic system for single-cycle-resolved imaging in internal combustion engines,” *APPLIED OPTICS*, vol. 41, no. 24, p. 5002–5014, Aug. 2002. [Online]. Available: http://apps.isiknowledge.com/full_record.do?product=WOS&search_mode=GeneralSearch&qid=1&SID=3CpBEcC7Hog44E1IjJI&page=1&doc=1
- [47] N. Jiang, W. R. Lempert, G. L. Switzer, T. R. Meyer, and J. R. Gord, “Narrow-linewidth megahertz-repetition-rate optical parametric oscillator for high-speed flow and combustion diagnostics,” *Applied Optics*, vol. 47, no. 1, p. 64–71, Jan. 2008. [Online]. Available: <http://ao.osa.org/abstract.cfm?URI=ao-47-1-64>
- [48] J. D. Miller, M. Slipchenko, T. R. Meyer, N. Jiang, W. R. Lempert, and J. R. Gord, “Ultrahigh-frame-rate OH fluorescence imaging in turbulent flames using a burst-mode optical parametric oscillator,” *Optics Letters*, vol. 34, no. 9, p. 1309–1311, May 2009. [Online]. Available: <http://ol.osa.org/abstract.cfm?URI=ol-34-9-1309>
- [49] M. M. Biss, G. S. Settles, M. J. Hargather, L. J. Dodson, and J. D. Miller, “High-speed digital shadowgraphy of shock waves from explosions and gunshots,” *SHOCK WAVES, VOL 1, PROCEEDINGS*, p. 91–96, 2009. [Online]. Available: <http://www.springerlink.com/content/j365378242011287/>
- [50] D. KLICK and F. KNIGHT, “Applications of a streak-camera-based imager with simultaneous high space and time resolution,” *20TH INTERNATIONAL CONGRESS ON HIGH-SPEED PHOTOGRAPHY AND PHOTONICS*, vol. 1801, p. 206–217, 1993. [Online]. Available: http://spiedigitallibrary.org/proceedings/resource/2/psisdg/1801/1/206_1?isAuthorized=no
- [51] J. D. Hrubes, “High-speed imaging of supercavitating underwater projectiles,” *Experiments in Fluids*, vol. 30, no. 1, p. 57–64, 2001. [Online]. Available: <http://www.springerlink.com/content/6hcv6rjel149jmy9/>
- [52] V. Tiwari, M. A. Sutton, and S. R. McNeill, “Assessment of high speed imaging systems for 2D and 3D deformation measurements: Methodology development and validation,” *Experimental Mechanics*, vol. 47, no. 4, p. 561–579, 2007. [Online]. Available: <http://www.springerlink.com/content/84617933tv566v46/>

- [53] Q. Nguyen, N. Callamaras, C. Hsieh, and I. Parker, "Construction of a two-photon microscope for video-rate Ca^{2+} imaging," *Cell Calcium*, vol. 30, no. 6, p. 383–393, Dec. 2001. [Online]. Available: <http://www.sciencedirect.com/science/article/B6WCC-45B5962-5/2/6991cf16b1757310799f8e96ac9cc04c>
- [54] A. Ercan, F. Xiao, X. Liu, S. Lim, A. E. Gamal, and B. Wandell, "Experimental high speed CMOS image sensor system and applications," in *Sensors, 2002. Proceedings of IEEE*, vol. 1, 2002, p. 15–20 vol.1. [Online]. Available: http://ieeexplore.ieee.org/xpls/abs_all.jsp?arnumber=1036979&tag=1
- [55] K. Hoyer, M. Holzner, B. Lüthi, M. Guala, A. Liberzon, and W. Kinzelbach, "3D scanning particle tracking velocimetry," *Experiments in Fluids*, vol. 39, no. 5, p. 923–934, 2005. [Online]. Available: <http://www.springerlink.com/content/r43k526861257u4p/>
- [56] D. Lee, H. Tippur, M. Kirugulige, and P. Bogert, "Experimental study of dynamic crack growth in unidirectional Graphite/Epoxy composites using digital image correlation method and high-speed photography," *Journal of Composite Materials*, vol. 43, no. 19, p. 2081–2108, 2009. [Online]. Available: <http://jcm.sagepub.com/content/43/19/2081.abstract>
- [57] J. Park, M. Hardy, S. J. Kang, K. Barton, K. Adair, D. Kishore Mukhopadhyay, C. Y. Lee, M. S. Strano, A. G. Alleyne, J. G. Georgiadis, P. M. Ferreira, and J. A. Rogers, "High-resolution electrohydrodynamic jet printing," *Nat Mater*, vol. 6, no. 10, p. 782–789, Oct. 2007. [Online]. Available: <http://dx.doi.org/10.1038/nmat1974>
- [58] S. Sugiura, M. Nakajima, S. Iwamoto, and M. Seki, "Interfacial tension driven monodispersed droplet formation from microfabricated channel array," *Langmuir*, vol. 17, no. 18, p. 5562–5566, 2001. [Online]. Available: <http://dx.doi.org/10.1021/la010342y>
- [59] S. Thoroddsen, T. Etoh, and K. Takehara, "High-Speed imaging of drops and bubbles," *Annual Review of Fluid Mechanics*, vol. 40, no. 1, p. 257–285, 2008. [Online]. Available: [http://arjournals.annualreviews.org/doi/abs/10.1146/annurev.fluid.40.111406.102215?prevSearch=\(microfluidic\)+AND+%5Bjournal%3A+fluid%5D](http://arjournals.annualreviews.org/doi/abs/10.1146/annurev.fluid.40.111406.102215?prevSearch=(microfluidic)+AND+%5Bjournal%3A+fluid%5D)
- [60] K. Shinohara, Y. Sugii, A. Aota, A. Hibara, M. Tokeshi, T. Kitamori, and K. Okamoto, "High-speed micro-PIV measurements of transient flow in microfluidic devices," *Measurement Science and Technology*, vol. 15, no. 10, p. 1965–1970, 2004. [Online]. Available: <http://iopscience.iop.org/0957-0233/15/10/003>
- [61] E. G. Drucker and G. V. Lauder, "Locomotor forces on a swimming fish: three-dimensional vortex wake dynamics quantified using digital particle image velocimetry," *J Exp Biol*, vol. 202, no. 18, p. 2393–2412, Sep. 1999. [Online]. Available: <http://jeb.biologists.org/cgi/content/abstract/202/18/2393>
- [62] H. Dong, W. W. Carr, and J. F. Morris, "An experimental study of drop-on-demand drop formation," *Physics of Fluids*, vol. 18, no. 7, p. 072102, 2006. [Online]. Available: <http://link.aip.org/link/PHFLE6/v18/i7/p072102/s1&Agg=doi>
- [63] P. Krehl, S. Engemann, C. Rembe, and E. P. Hofer, "High-speed visualization, a powerful diagnostic tool for microactuators - retrospect and prospect," *Microsystem Technologies*, vol. 5, no. 3, p. 113–132, 1999. [Online]. Available: <http://www.springerlink.com/content/wbd0pxcmk4d90f/>
- [64] C. Rembe, R. Kant, and R. S. Muller, "Optical measurement methods to study dynamic behavior in MEMS," *MICROSYSTEMS ENGINEERING: METROLOGY AND INSPECTION*, vol. 4400, p. 127–137, 2001. [Online]. Available: http://apps.isiknowledge.com/full_record.do?product=WOS&search_mode=GeneralSearch&qid=13&SID=3CpBEcC7Hog44E1IjJI&page=1&doc=1&cacheurlFromRightClick=no

- [65] S. N. Patek, J. E. Baio, B. L. Fisher, and A. V. Suarez, “Multifunctionality and mechanical origins: Ballistic jaw propulsion in trap-jaw ants,” *Proceedings of the National Academy of Sciences*, vol. 103, no. 34, p. 12787–12792, 2006. [Online]. Available: <http://www.pnas.org/content/103/34/12787.abstract>
- [66] T. Braunschweig, J. Flaschka, P. Schelhorn-Neise, and M. Döllinger, “High-speed video analysis of the phonation onset, with an application to the diagnosis of functional dysphonias,” *Medical Engineering & Physics*, vol. 30, no. 1, p. 59–66, Jan. 2008. [Online]. Available: <http://www.sciencedirect.com/science/article/B6T9K-4N3H15X-1/2/Oafe068329d7ebec94518b58fa2ecb95>
- [67] M. E. Llewellyn, R. P. J. Barretto, S. L. Delp, and M. J. Schnitzer, “Minimally invasive high-speed imaging of sarcomere contractile dynamics in mice and humans,” *Nature*, vol. 454, no. 7205, p. 784–788, 2008. [Online]. Available: <http://dx.doi.org/10.1038/nature07104>
- [68] G. V. Lauder and P. G. Madden, “Advances in comparative physiology from High-Speed imaging of animal and fluid motion,” *Annual Review of Physiology*, vol. 70, no. 1, p. 143–163, 2008. [Online]. Available: <http://arjournals.annualreviews.org/doi/abs/10.1146/annurev.physiol.70.113006.100438>
- [69] T. Schmoll, C. Kolbitsch, and R. A. Leitgeb, “Ultra-high-speed volumetric tomography of human retinal blood flow,” *Optics Express*, vol. 17, no. 5, p. 4166–4176, Mar. 2009. [Online]. Available: <http://www.opticsexpress.org/abstract.cfm?URI=oe-17-5-4166>
- [70] Y. K. Tao, A. M. Davis, and J. A. Izatt, “Single-pass volumetric bidirectional blood flow imaging spectral domain optical coherence tomography using a modified hilbert transform,” *Optics Express*, vol. 16, no. 16, p. 12350–12361, 2008. [Online]. Available: <http://www.opticsexpress.org/abstract.cfm?URI=oe-16-16-12350>
- [71] Y. K. Tao, K. M. Kennedy, and J. A. Izatt, “Velocity-resolved 3D retinal microvessel imaging using single-pass flow imaging spectral domain optical coherence tomography,” *Optics Express*, vol. 17, no. 5, p. 4177–4188, Mar. 2009. [Online]. Available: <http://www.opticsexpress.org/abstract.cfm?URI=oe-17-5-4177>
- [72] D. Yelin, B. E. Bouma, J. J. Rosowsky, and G. J. Tearney, “Doppler imaging using spectrally-encoded endoscopy,” *Optics Express*, vol. 16, no. 19, p. 14836–14844, 2008. [Online]. Available: <http://www.opticsexpress.org/abstract.cfm?URI=oe-16-19-14836>
- [73] J. R. Hove, R. W. Koster, A. S. Forouhar, G. Acevedo-Bolton, S. E. Fraser, and M. Gharib, “Intracardiac fluid forces are an essential epigenetic factor for embryonic cardiogenesis,” *Nature*, vol. 421, no. 6919, p. 172–177, Jan. 2003. [Online]. Available: <http://dx.doi.org/10.1038/nature01282>
- [74] J. R. Hove, “Quantifying cardiovascular flow dynamics during early development,” *Pediatric Research*, vol. 60, no. 1, p. 6–13, 2006. [Online]. Available: http://journals.lww.com/pedresearch/Fulltext/2006/07000/Quantifying_Cardiovascular_Flow_Dynamics_During.2.aspx
- [75] V. Bansal, S. Patel, and P. Saggau, “High-speed addressable confocal microscopy for functional imaging of cellular activity,” *Journal of Biomedical Optics*, vol. 11, no. 3, p. 034003–9, May 2006. [Online]. Available: <http://link.aip.org/link/?JBO/11/034003/1>
- [76] J. Bradley, R. Luo, T. S. Otis, and D. A. DiGregorio, “Submillisecond optical reporting of membrane potential in situ using a neuronal tracer dye,” *J. Neurosci.*, vol. 29, no. 29, p. 9197–9209, Jul. 2009. [Online]. Available: <http://www.jneurosci.org/cgi/content/abstract/29/29/9197>

- [77] V. Crépel, D. Aronov, I. Jorquera, A. Represa, Y. Ben-Ari, and R. Cossart, “A Parturition-Associated nonsynaptic coherent activity pattern in the developing hippocampus,” *Neuron*, vol. 54, no. 1, p. 105–120, Apr. 2007. [Online]. Available: <http://www.sciencedirect.com/science/article/B6WSS-4NDNGYC-F/2/308982e0d9914265c0ca35b4a06cb4e4>
- [78] V. R. Daria, C. Stricker, R. Bowman, S. Redman, and H. Bachor, “Arbitrary multisite two-photon excitation in four dimensions,” *Applied Physics Letters*, vol. 95, no. 9, p. 093701, 2009. [Online]. Available: <http://link.aip.org/link/APPLAB/v95/i9/p093701/s1&Agg=doi>
- [79] W. Goebel and R. Helmchen, “Optical 3D measurement of neuronal network dynamics,” *NEUROFORUM*, vol. 14, no. 2, p. 184–189, Jun. 2008. [Online]. Available: http://apps.isiknowledge.com/full_record.do?product=WOS&search_mode=GeneralSearch&qid=21&SID=3CpBEcC7Hog44E1IjJI&page=1&doc=1&cacheurlFromRightClick=no
- [80] W. Gobel, B. M. Kampa, and F. Helmchen, “Imaging cellular network dynamics in three dimensions using fast 3D laser scanning,” *Nat Meth*, vol. 4, no. 1, p. 73–79, Jan. 2007. [Online]. Available: <http://dx.doi.org/10.1038/nmeth989>
- [81] K. P. Lillis, A. Eng, J. A. White, and J. Mertz, “Two-photon imaging of spatially extended neuronal network dynamics with high temporal resolution,” *Journal of Neuroscience Methods*, vol. 172, no. 2, p. 178–184, Jul. 2008. [Online]. Available: <http://www.sciencedirect.com/science/article/B6T04-4SDX2NF-1/2/9ad8930a97f143dbfb1b2160b40bc4e8>
- [82] S. Namiki and Y. Ikegaya, “Current application and technology of functional multineuron calcium imaging,” *BIOLOGICAL & PHARMACEUTICAL BULLETIN*, vol. 32, no. 1, p. 1–9, Jan. 2009. [Online]. Available: http://www.jstage.jst.go.jp/article/bpb/32/1/32_1/_article
- [83] Y. Otsu, V. Bormuth, J. Wong, B. Mathieu, G. P. Dugué, A. Feltz, and S. Dieudonné, “Optical monitoring of neuronal activity at high frame rate with a digital random-access multiphoton (RAMP) microscope,” *Journal of Neuroscience Methods*, vol. 173, no. 2, p. 259–270, Aug. 2008. [Online]. Available: <http://www.sciencedirect.com/science/article/B6T04-4SVC5HD-1/2/aa9836aa3e71e31d900ef97b08a60995>
- [84] G. D. Reddy and P. Saggau, “Fast three-dimensional laser scanning scheme using acousto-optic deflectors,” *Journal of Biomedical Optics*, vol. 10, no. 6, p. 064038–10, Nov. 2005. [Online]. Available: <http://link.aip.org/link/?JBO/10/064038/1>
- [85] T. Sasaki, N. Takahashi, N. Matsuki, and Y. Ikegaya, “Fast and accurate detection of action potentials from somatic calcium fluctuations,” *J Neurophysiol*, vol. 100, no. 3, p. 1668–1676, Sep. 2008. [Online]. Available: <http://jn.physiology.org/cgi/content/abstract/100/3/1668>
- [86] G. Stutzmann, “Seeing the brain in action: How multiphoton imaging has advanced our understanding of neuronal function,” *MICROSCOPY AND MICROANALYSIS*, vol. 14, no. 6, p. 482–491, Dec. 2008. [Online]. Available: <http://journals.cambridge.org/action/displayAbstract?fromPage=online&aid=2598996>
- [87] GerstnerEd, “Nobel prize 2009: Kao, boyle & smith,” *Nat Phys*, vol. 5, no. 11, p. 780, Nov. 2009. [Online]. Available: <http://dx.doi.org/10.1038/nphys1454>
- [88] E. R. Fossum, “CMOS image sensors: Electronic camera-on-a-chip,” *IEEE TRANSACTIONS ON ELECTRON DEVICES*, vol. 44, no. 10, p. 1689–1698, Oct. 1997. [Online]. Available: http://apps.isiknowledge.com/full_record.do?product=WOS&search_mode=GeneralSearch&qid=29&SID=4EklIPEKhhf6Jgn7hkj&page=1&doc=1
- [89] J. Mendez, S. Balzer, S. Watson, R. Reich, and D. O’Mara, “A Multi-Frame, megahertz CCD imager,” *Nuclear Science, IEEE Transactions on*, vol. 56, no. 3, p. 1188–1192, 2009. [Online]. Available: [10.1109/TNS.2009.2013238](https://doi.org/10.1109/TNS.2009.2013238)

- [90] R. Melen, "The tradeoffs in monolithic image sensors: MOS vs CCD," *Electronics*, vol. 46, no. 11, p. 106–111, 1973. [Online]. Available: http://apps.isiknowledge.com/full_record.do?product=WOS&search_mode=GeneralSearch&qid=53&SID=4EklPEKhHf6Jgn7hkj&page=1&doc=1
- [91] M. El-Desouki, M. J. Deen, Q. Fang, L. Liu, F. Tse, and D. Armstrong, "CMOS image sensors for high speed applications," *Sensors*, vol. 9, no. 1, pp. 430–444, 2009. [Online]. Available: <http://www.mdpi.com/1424-8220/9/1/430>
- [92] S. Kleinfelder, S. Lim, X. Liu, and A. E. Gamal, "A 10000 frames/s CMOS digital pixel sensor," *Solid-State Circuits, IEEE Journal of*, vol. 36, no. 12, p. 2049–2059, 2001. [Online]. Available: http://ieeexplore.ieee.org/xpls/abs_all.jsp?arnumber=972156
- [93] M. Bigas, E. Cabruja, J. Forest, and J. Salvi, "Review of CMOS image sensors," *Microelectronics Journal*, vol. 37, no. 5, p. 433–451, May 2006. [Online]. Available: <http://www.sciencedirect.com/science/article/B6V44-4H21R3N-1/2/348a7b2ee3dfd1f4fcc6783d808fb7cb>
- [94] R. G. Driggers, C. E. Halford, G. D. Boreman, D. Lattman, and K. F. Williams, "Parameters of spinning FM reticles," *Applied Optics*, vol. 30, no. 7, pp. 887–895, Mar. 1991. [Online]. Available: <http://ao.osa.org/abstract.cfm?URI=ao-30-7-887>
- [95] T. Tanaami, S. Otsuki, N. Tomosada, Y. Kosugi, M. Shimizu, and H. Ishida, "High-Speed 1-Frame/ms scanning confocal microscope with a microlens and nipkow disks," *Applied Optics*, vol. 41, no. 22, p. 4704–4708, 2002. [Online]. Available: <http://ao.osa.org/abstract.cfm?URI=ao-41-22-4704>
- [96] R. G. McAllister, D. R. Sisan, and J. S. Urbach, "Design and optimization of a high-speed, high-sensitivity, spinning disk confocal microscopy system," *Journal of Biomedical Optics*, vol. 13, no. 5, p. 054058–7, 2008. [Online]. Available: <http://link.aip.org/link/?JBO/13/054058/1>
- [97] H. Kinoshita, S. Kaneda, T. Fujii, and M. Oshima, "Three-dimensional measurement and visualization of internal flow of a moving droplet using confocal micro-PIV," *LAB ON A CHIP*, vol. 7, no. 3, p. 338–346, 2007. [Online]. Available: <http://pubs.rsc.org/en/Content/ArticleLanding/2007/LC/b617391h>
- [98] M. A. A. Neil, R. Juskaitis, and T. Wilson, "Method of obtaining optical sectioning by using structured light in a conventional microscope," *Optics Letters*, vol. 22, no. 24, p. 1905–1907, Dec. 1997. [Online]. Available: <http://ol.osa.org/abstract.cfm?URI=ol-22-24-1905>
- [99] M. G. L. Gustafsson, "Surpassing the lateral resolution limit by a factor of two using structured illumination microscopy," *JOURNAL OF MICROSCOPY-OXFORD*, vol. 198, p. 82–87, May 2000. [Online]. Available: <http://onlinelibrary.wiley.com/doi/10.1046/j.1365-2818.2000.00710.x/full>
- [100] J. T. Frohn, H. F. Knapp, and A. Stemmer, "True optical resolution beyond the rayleigh limit achieved by standing wave illumination," *Proceedings of the National Academy of Sciences of the United States of America*, vol. 97, no. 13, p. 7232–7236, Jun. 2000. [Online]. Available: <http://www.pnas.org/content/97/13/7232.abstract>
- [101] M. G. L. Gustafsson, "Nonlinear structured-illumination microscopy: Wide-field fluorescence imaging with theoretically unlimited resolution," *Proceedings of the National Academy of Sciences of the United States of America*, vol. 102, no. 37, p. 13081–13086, 2005. [Online]. Available: <http://www.pnas.org/content/102/37/13081.abstract>